Cell Reports

Article

Rapid assembly of a polar network architecture drives efficient actomyosin contractility

Graphical abstract

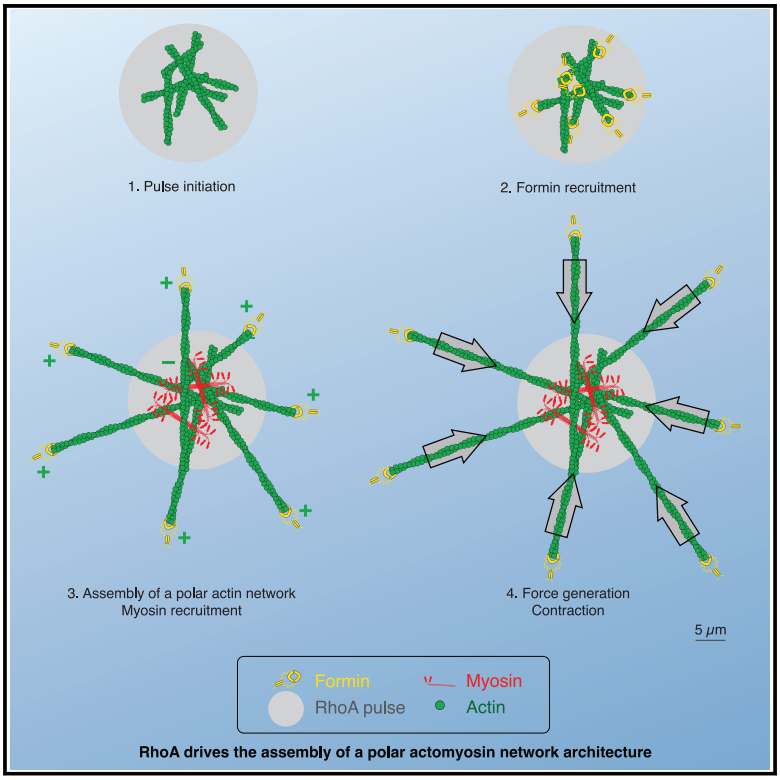

Authors

Vlad Costache, Serena Prigent Garcia, Camille N. Plancke, ..., Anne-Cécile Reymann, Taeyoon Kim, François B. Robin

Correspondence

kimty@purdue.edu (T.K.), francois.robin@sorbonne-universite.fr (F.B.R.)

In brief

RhoA-driven actomyosin contractility plays a key role in driving cell and tissue contractility during morphogenesis. Tracking individual formins, Costache et al. show that the network assembled downstream of RhoA displays a polar architecture, barbed ends pointing outward, a feature that supports efficient contractility and force transmission during pulsed contractions.

Highlights

- The formin CYK-1 drives actin network assembly downstream of RhoA pulses
- A barbed-end saturation mechanism could allow responsive F-actin assembly
- Rapid F-actin elongation results in assembly of aster-like polar actin networks
- Numerical simulations show network polarity drives efficient network contractility

Costache et al., 2022, Cell Reports *39*, 110868
May 31, 2022
https://doi.org/10.1016/j.celrep.2022.110868

CellPress

Cell Reports

CellPress
OPEN ACCESS

Article

Rapid assembly of a polar network architecture drives efficient actomyosin contractility

Vlad Costache,[1,4] Serena Prigent Garcia,[1,4] Camille N. Plancke,[1] Jing Li,[2] Simon Begnaud,[1] Shashi Kumar Suman,[1] Anne-Cécile Reymann,[3] Taeyoon Kim,[2,*] and François B. Robin[1,5,*]

[1]Sorbonne Université, CNRS, INSERM, Institut de Biologie Paris-Seine IBPS, Laboratoire de Biologie du Développement, Paris, France
[2]Weldon School of Biomedical Engineering, Purdue University, West Lafayette, IN, USA
[3]IGBMC, CNRS UMR7104, INSERM U1258, and Université de Strasbourg, Illkirch, France
[4]These authors contributed equally
[5]Lead contact
*Correspondence: kimty@purdue.edu (T.K.), francois.robin@sorbonne-universite.fr (F.B.R.)
https://doi.org/10.1016/j.celrep.2022.110868

SUMMARY

Actin network architecture and dynamics play a central role in cell contractility and tissue morphogenesis. RhoA-driven pulsed contractions are a generic mode of actomyosin contractility, but the mechanisms underlying how their specific architecture emerges and how this architecture supports the contractile function of the network remain unclear. Here we show that, during pulsed contractions, the actin network is assembled by two subpopulations of formins: a functionally inactive population (recruited) and formins actively participating in actin filament elongation (elongating). We then show that elongating formins assemble a polar actin network, with barbed ends pointing out of the pulse. Numerical simulations demonstrate that this geometry favors rapid network contraction. Our results show that formins convert a local RhoA activity gradient into a polar network architecture, causing efficient network contractility, underlying the key function of kinetic controls in the assembly and mechanics of cortical network architectures.

INTRODUCTION

Vastly conserved in eukaryotes, the actomyosin cytoskeleton is a major determinant of the mechanical properties of embryonic cells and tissues (Munjal and Lecuit, 2014). Modulation of actomyosin networks activity plays a critical role in cell shape changes, cell division, cell migration, and polarization. The integration of these behaviors, at the tissue scale, drives tissue deformation and morphogenesis (Lecuit and Lenne, 2007). At the molecular scale, however, the role of the architecture of actomyosin networks has been a research focus and subject of some debate (Blanchoin et al., 2014; Koenderink and Paluch, 2018; Agarwal and Zaidel-Bar, 2019). In muscle, the mechanisms of actomyosin contractility have historically been characterized, showing that, in this quasi-crystalline organization, the sliding of bipolar myosin II mini-filaments along actin filaments drives network contractility and sarcomere shortening. In other contexts, in contrast, and in particular at the cell cortex of developing embryos, seemingly disordered actin networks remain poorly understood in terms of network polarity, length distribution, mesh size, turnover rates, or crosslinking levels, and we still do not fully comprehend how F-actin architecture is functionally linked to network contractility. Theoretical studies (Lenz et al., 2012a, 2012b) and computational models (Kim, 2015) have shown that asymmetry between the compressive and extensive modulus—the ability to withstand tension but buckle under compressive forces—can drive contraction of disordered bundles. Similarly, numerical simulations and *in vitro* experiments have clearly demonstrated that non-polar actin networks can contract (Yu et al., 2018). Cellular networks however, often display characteristic organization, suggesting that specific network dynamics and geometries may play a critical role in network contractility (Koenderink and Paluch, 2018).

Active Rho GTPase zones have recently emerged as essential regulators to template the architecture of the actomyosin meshwork by defining active, task-tuned zones of cytoskeletal assembly (Miller and Bement, 2009). Examples of such zones include the leading edge of migrating cells, the cleavage furrow during cell division, and the apical cortex during apical constriction. During embryonic morphogenesis in particular, a wide class of morphogenetic processes is driven by pulsed contractions, a widespread mode of actomyosin contractility where transient and iterative F-actin and myosin II accumulations accompany contraction of the actomyosin network (He et al., 2010; Kim and Davidson, 2011; Martin et al., 2009; Munro et al., 2004; Roh-Johnson et al., 2012). Previous work has shown that pulsed contractions are driven by excitable dynamics of the Rho GTPase RhoA, leading to formation of activation zones that drive recruitment of downstream effectors, including formin, Anillin, F-actin, and myosin II (Maddox et al., 2005; Munro et al., 2004; Michaux et al., 2018; Naganathan et al., 2018; Reymann et al., 2016). Excitable dynamics, with feedforward activation and delayed negative feedback, seem to play an important role to establish Rho activation (Bement et al., 2015; Nishikawa et al., 2017; Michaux et al., 2018).

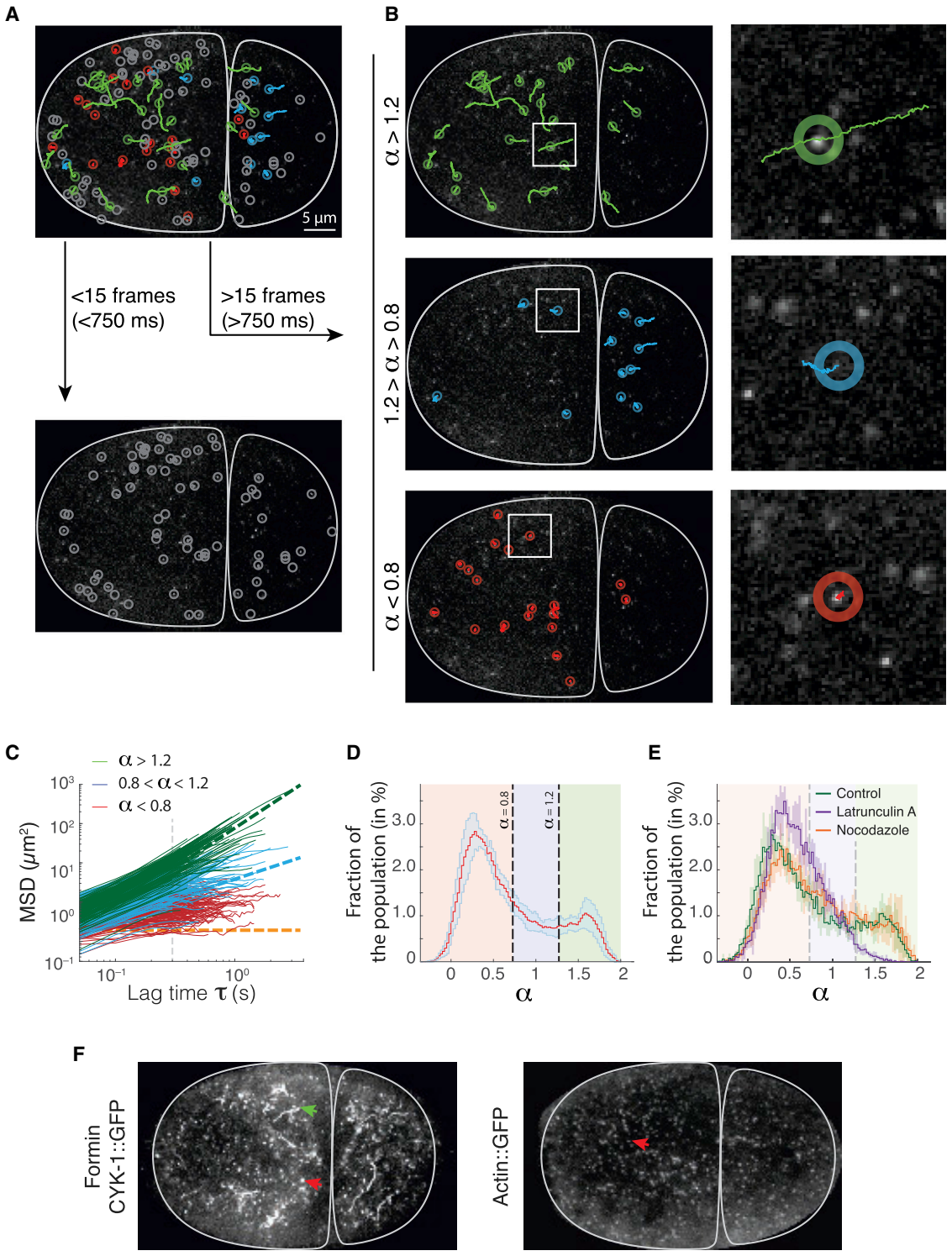

Figure 1. Anomalous diffusion of individual formin molecules identifies a subpopulation of actin-elongating formins

(A) Single-molecule imaging and tracking of formins fused with GFP (CYK-1::GFP CRISPR strain) shows individual behaviors ranging from superdiffusive (green) to diffusive (blue) to subdiffusive (red).

(B) Detected mobilities correspond to different classes of behaviors. Superdiffusive particles display a characteristic ballistic motion (green, top panel), whereas subdiffusive particles appear immobile in the cortex (red, bottom).

(legend continued on next page)

Thus, Rho GTPases spatially and temporally pattern the recruitment, turnover, and activity of downstream effectors. It remains unclear, however, how these orchestrated modulations of actomyosin dynamics support the specific cellular function of Rho zones. Here we show that the dynamics and topology of RhoA activation, converting a RhoA chemical gradient into assembly of a polar actin network, drive formation of a network structure tuned to its contractile function.

In the nematode *Caenorhabditis elegans*, pulsed contractions occur from the 1-cell stage onward during interphase (Munro et al., 2004; Mayer et al., 2010) and support cell polarization and apical constriction (Nance and Priess, 2002; Nance et al., 2003; Roh-Johnson et al., 2012). Here we show that RhoA pulses control accumulation of the formin CYK-1 (a diaphanous/mDia homolog), driving F-actin accumulation during pulsed contractions. We further show that actin network assembly is kinetically controlled by saturation of actin filament barbed ends, resulting in a time-optimal response to RhoA activation so that initiation of actin elongation closely follows the RhoA pulse. Using single-molecule microscopy to infer local actin filament orientation during pulse assembly, we show that formin-assembled actin networks are polar, generating networks with barbed ends pointing outside of the pulse. Finally, our computational exploration shows that this polar network architecture is favorable for generation of efficient actomyosin contractility. These results underline kinetic rather than mechanical control of actomyosin network orientation during pulsed contractions. They also underline the evolution of billion-years-old machinery, reusing molecular machinery—formin, F-actin, and myosin II—to drive a fundamentally conserved phenomenon, precisely tuned force generation, with opposite geometries reflecting organism-specific construction rules and constraints.

RESULTS

Cortical dynamics of formins in a developing embryo

Formins drive assembly of a variety of actin-based cellular structures that drive physiological processes ranging from cell division and cell migration to cell polarization (Rottner et al., 2017). Formins are actin nucleators and processive actin elongators, catalyzing addition of actin monomers to the barbed end of actin filaments while protecting the filament against capping (Courtemanche, 2018). In *C. elegans*, 7 formin genes have been identified previously (Mi-Mi et al., 2012). Mutants for five of them are viable (Mi-Mi et al., 2012), and the product of another localizes to the nucleus and does not interact with actin *in vitro* (Amin et al., 2007, 2009; Johnston et al., 2006). *cyk-1* (cytokinetic defective-1), the only ortholog of the Diaphanous family of formins, is required for cell division and plays a key role in actin assembly during the early stages of embryonic development (Swan et al., 1998).

To study CYK-1 in *C. elegans*, we first generated a GFP CRISPR knockin at the genomic *cyk-1* locus. The resulting strain is fully viable and displays no readily identifiable phenotype, suggesting that the fusion protein is fully functional. We then used live single-molecule fluorescence microscopy to visualize the dynamics of individual formin molecules fused with GFP (Robin et al., 2014). We first observed that formins were apparently classified into at least two populations (Video S1), ballistic and static, as observed previously in other systems (Higashida et al., 2004, 2013; Funk et al., 2019). To better visualize these two populations, we used maximum intensity projection to visualize formin trajectories over 100 consecutive time points (Video S2). Static formins appeared as dots, and moving formins appeared as a trail on the cell surface.

To quantitatively characterize these two populations, we performed single-particle tracking and analyzed the trajectories of 19,137 individual formin molecules from 5 embryos. Based on the logarithmic regression of the mean squared displacement to an anomalous diffusion model, $MSD = 2D \cdot t^{\alpha}$ (Robin et al., 2014), we characterized all particle trajectories longer than 15 frames or 750 ms (Figures 1A and 1B) by their anomalous diffusion coefficient D and scaling exponent α. We could clearly distinguish the two formin populations, static and ballistic, with apparent distributions of the scaling exponent peaking at $\alpha = 0.3$ (subdiffusive) and $\alpha = 1.6$ (superdiffusive), respectively (Figures 1C, 1D, and S1A–S1D; Video S3). We subsequently used these empirical metrics to classify and sort these two sub-populations.

Previous work has suggested that these superdiffusive particles represent formins actively elongating actin filaments (Higashida et al., 2004, 2008, 2013; Funk et al., 2019). To confirm this, we used RNAi against *perm-1*, a known component of eggshell protein (Carvalho et al., 2011; Olson et al., 2012) that permeabilizes the eggshell, and subsequently treated the embryos with the microtubule-depolymerizing drug nocodazole and the actin-depolymerizing drug latrunculin A (Video S4). Performing the same analysis as before, we observed that the superdiffusive population essentially disappeared after latrunculin A treatment but was unaffected by nocodazole treatment (Figure 1E; Video S4). Latrunculin A (LatA) treatment resulted in initially increased recruitment of formins at the cell cortex immediately after LatA treatment (Figures S1E–S1G). Although our quantitative analysis did not reveal strong differences in the fraction of superdiffusive versus subdiffusive population during this brief period after LatA treatment, we could not exclude that this increased

(C) MSD versus lag time (log-log scale). Curve slope reports on the anomalous diffusion exponent α of the trajectory. Green: superdiffusive ($\alpha > 1.2$). Blue: diffusive ($0.8 < \alpha < 1.2$). Red: subdiffusive ($\alpha < 0.8$). Green dashed: pure superdiffusive ($\alpha = 2$). Blue dashed: pure diffusive ($\alpha = 1$). Orange dashed: immobile ($\alpha = 0$). Detailed curves are available in Figures S1D–S1G.

(D) Distribution of the fraction of particles displaying a given anomalous diffusion exponent in 5 videos (average ±SD). Background shows the domains corresponding to the classification used here. Two peaks seem to emerge, centered at $\alpha = 0.3$ and $\alpha = 1.6$.

(E) Compared with the control (green curve), the superdiffusive population is absent in embryos treated with LatA (purple) but not nocodazole (orange). More than 2,000 tracks were analyzed per embryo, with more than 5 embryos per condition presented.

(F) Projection over 5 s (100 consecutive frames) of formin CYK-1::GFP (left) and actin::GFP (right) speckles, showing subdiffusive speckles (red arrow) and superdiffusive trails (green arrow). Actin::GFP does not display superdiffusive trails.

formin recruitment could be caused by increased CYK-1 nucleation secondary to an increase in G-actin concentration (Figures S1E–S1G). These results strongly supported the idea that superdiffusive cortical CYK-1::GFP speckles corresponded to formin dimers actively and processively elongating actin filaments at the barbed end of the filament at the cell cortex.

To measure the speed of formin speckles, we used two metrics. We either selected a collection of trajectories, smoothed them, projected the position of the formin on the smoothed trajectory, and quantified the traveled distance along this trajectory, or we used mean squared displacement (MSD) measurements presented before. Both metrics yielded very similar result, 1.1 ± 0.2 $\mu m \cdot s^{-1}$ and 1.3 ± 0.2 $\mu m \cdot s^{-1}$ (standard deviation), in line with previously reported speeds (Higashida et al., 2004) but slower than in a recent *in vivo* report (Funk et al., 2019).

To test whether immobile formins may be elongating actin filaments, we decided to use fiducial markers on the network of actin filaments. We showed previously in *C. elegans* that actin::GFP incorporates at the cleavage furrow during cell division (Robin et al., 2014), which has also been demonstrated in mammalian cell culture (Murthy and Wadsworth, 2005; Zhou and Wang, 2008; see also Skruber et al., 2018). In embryos depleted of Arp-2/3 by RNAi, cortical recruitment of actin::GFP is unaltered (Michaux et al., 2018). This suggests that, although actin::GFP might be selected against and not fully functional, it is still incorporated in formin-elongated networks and should work as an effective probe to test our hypothesis. We did not observe significant directional movements, and single-molecule speckles of actin::GFP remained largely immobile (Video S5).

To ascertain that our result was not affected by a failure of actin::GFP to efficiently incorporate into the formin network (Chen et al., 2012; Wu and Pollard, 2005), we decided confirm this first result by observing the single-molecule cortical dynamics of an F-actin side-binding probe, UtrophinABD::GFP. Although this alternative strategy would not focus on actin monomers recently incorporated into the network, if strong elongation from immobile formins were to occur and displace actin monomers, then we would expect to see a signature of these movements in the motion of UtrophinABD::GFP speckles. Similarly, single-molecule speckles of actin::GFP and UtrophinABD::GFP remained largely immobile, not displaying significant directional mobility. The fact that neither probe displayed significant directional movements, and single-molecule speckles of actin::GFP and UtrophinABD::GFP remained largely immobile (Figure 1F; Videos S5, S6, and S7; Robin et al., 2014), strongly supports the idea that filament elongation instead fully translates in formin directional motion and that immobile formins are indeed not elongating actin filaments, or at very low speeds.

These data show that CYK-1 velocity is a reliable *in vivo* proxy for formin elongation rate, demonstrating an average elongation rate of ∼400–468 monomers$\cdot s^{-1}$. Incidentally, our results also suggest that CYK-1 could be used as a biosensor to measure cellular modulations of the concentrations of profilin-ATP-G-actin, calibrated on elongation rates reported previously *in vitro* in the presence of profilin (Neidt et al., 2008, 2009). Provided that, in our system, formin-mediated actin filament elongation rates are not buffered by slow dissociation of profilin from the barbed end (Funk et al., 2019) or modulated by mechanical forces (Jégou et al., 2013; Courtemanche et al., 2013; Kubota et al., 2017), our results point to a local profilin-ATP-G-actin concentration in the early embryo in the ∼10–12 μM range (see STAR Methods for details).

Formin-mediated actin filament elongation rates during the cell cycle

To explore whether actin elongation was dynamically modulated during embryonic development, we measured formin velocity at the 1-, 2-, and 4-cell stages during distinct phases of the cell cycle (Figure 2A). To avoid confounding effects of overcrowding on tracking at high particle density, we decided to use a strain overexpressing CYK-1::GFP, which displays essentially identical dynamics as our CRISPR CYK-1::GFP but allowed us to use GFP RNAi (Robin et al., 2014) to visualize formins at much lower densities, improving particle tracking (Videos S8 and S9). At the 1-cell stage, the elongation rate remained unchanged from polarization to the maintenance phase (1.25 ± 0.18 $\mu m \cdot s^{-1}$ and 1.27 ± 0.16 $\mu m \cdot s^{-1}$, respectively) but decreased significantly over the entire cortex during cytokinesis to 1.05 ± 0.22 $\mu m \cdot s^{-1}$.

The velocity increased again after cytokinesis, going back to levels similar to 1-cell stage polarity establishment (1.24 ± 0.19 $\mu m \cdot s^{-1}$), remaining stable or slightly decreasing during mitosis (1.18 ± 0.18 $\mu m \cdot s^{-1}$) in the AB cell, and decreasing again during AB cytokinesis (1.04 ± 0.18 $\mu m \cdot s^{-1}$). During interphase at the 4-cell stage in ABp, formin velocity increased again but was notably lower in interphase compared with mitosis (1.15 ± 0.17 $\mu m \cdot s^{-1}$ at interphase and 1.24 ± 0.18 $\mu m \cdot s^{-1}$ during mitosis). These results show that formin speed drops significantly during cytokinesis but increases when interphase resumes.

To compare actin elongation rates across lineages, we also measured formin speed in AB and P1 at the 2-cell stage during interphase (1.24 ± 0.19 $\mu m \cdot s^{-1}$ and 1.18 ± 0.18 $\mu m \cdot s^{-1}$, respectively) and during mitosis (1.18 ± 0.18 $\mu m \cdot s^{-1}$ and 1.22 ± 0.19 $\mu m \cdot s^{-1}$, respectively) (Figure 2B). Our results suggest that formin speed does not vary between the two cell types.

We also manually quantified the fraction of superdiffusive formins at different stages of the cell cycle from the 1- to the 4-cell stage. We observed that the ratio fluctuates mildly from 20% to 35% from the 1- to the 4-cell stage, with the highest fraction of superdiffusive formins observed during interphase (Figure S2).

Actin elongation dynamics are distinctly modulated during phases of the cell cycle, decreasing significantly by more than 10% during cytokinesis and increasing again after cytokinesis completion. The measured elongation rates seemed to be relatively robust and only changed marginally from the 1-cell to the 4-cell stage. Because the measured elongation rates reflect the catalytic enzymatic activity of formin as an actin elongator, these changes could report on modulations in the concentration of G-actin species, either free G-actin or complexed with other factors, such as the profilin PFN-1. The balance between these various species in particular might play an important role in control of elongation rates. Our results suggest that F-actin elongation dynamics might be dynamically regulated by the concentrations of G-actin species but remain largely robust through time and across cell lineages during early embryonic development.

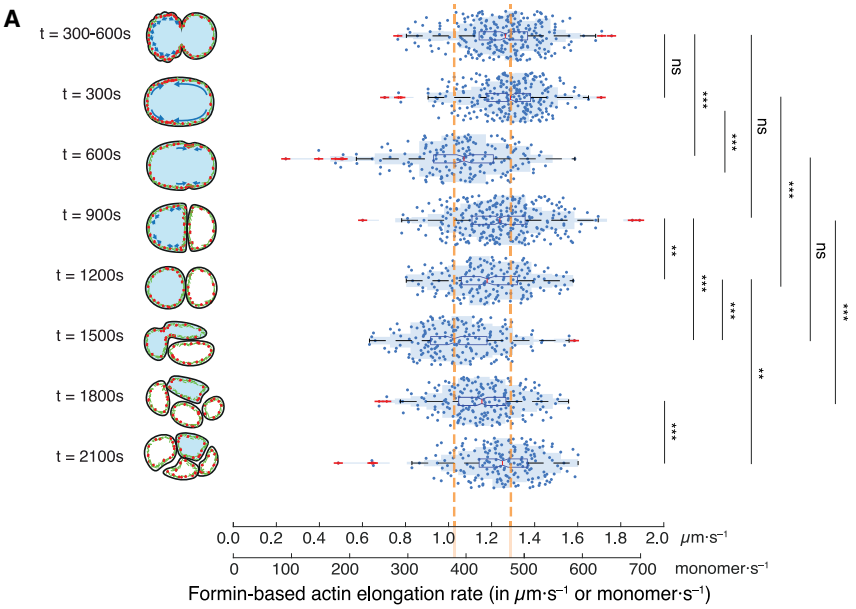

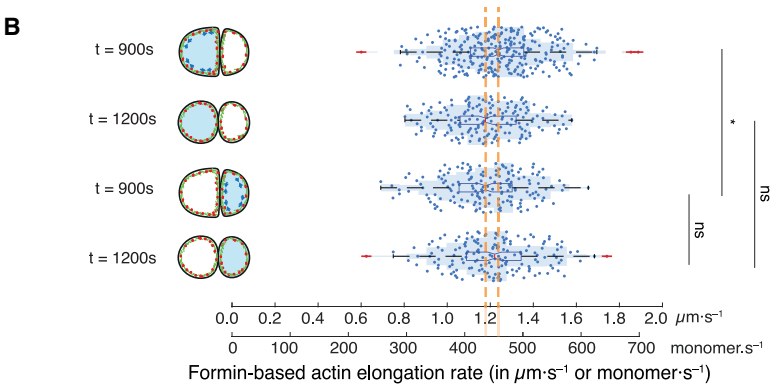

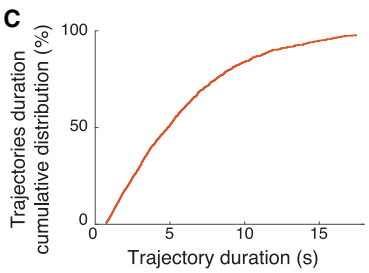

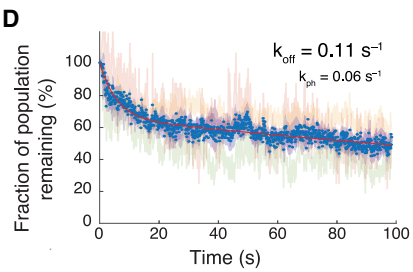

Figure 2. Formin speed is changed by the cell cycle but conserved through cell lineages

(A and B) Formin speed in AB (A) and P1 (B) cells. Right: distribution of elongating formin speed. Left: schematic of the stage and location of the cell from which the tracks are extracted, with the measured cell in light blue. Myosin is shown in red and actin in green. *p ≥0.05, **p ≥0.01, ***p ≥0.001; ns, not significant. A dashed orange line marks upper and lower averages. Outliers are shown in red. See Tables S1 and S2 for detailed statistical information.

(C) Cumulative distribution of CYK-1::GFP trajectory duration as a fraction of detection events, showing a half-life of ~5 s.

(D) The surviving fraction of cortical CYK-1::GFP as a function of photobleaching time reports on the turnover rate k_{off} and the photobleaching rate k_{ph}. Curves of photobleaching for 4 individual embryos, normalized for initial values, are shown in colored shades. Biexponential fit is shown in solid red. Experiments were performed on the CYK-1::GFP overexpression strain. GFP density was reduced using GFP RNAi.

Formin kinetics and implications on actin filament length *in vivo*

The length of formin-elongated actin filaments is controlled by a combination of the formin elongation rate, the formin global off-rate (combining unbinding and competition), and the turnover rate of F-actin monomers in the cortex. Specifically, we assumed that F-actin turnover and elongation dynamics are independent processes and follow exponential laws with the characteristic rate $1/\tau_{actin}$ and $1/\tau_{formin}$. For an F-actin monomer at the time of its disassembly, the length of a filament from the monomer the to the barbed end of the filament follows an exponential law with the characteristic length $L_{filament} = V_{formin} \times \tau_{filament}$, where $1/\tau_{filament} = 1/\tau_{actin} + 1/\tau_{formin}$ is a characteristic "off" rate of formins and V_{formin} their speed (see supplemental information for the detailed derivation). To estimate filament length, we needed to access actin and formin off-rates and use our measured actin filament elongation rates.

We expected a significant fraction of trajectory to be interrupted by tracking failure or photobleaching, barring us from using single-molecule tracking as a proxy (Figure 2C). We therefore turned to a previously established strategy, smPReSS (Robin et al., 2014), to estimate a bulk turnover rate for formins as well as the photobleaching rate. Briefly, by measuring the depletion of cortical formins caused by laser illumination of the cortex in a CYK-1 overexpression strain, we can infer the photobleaching rate and subsequently estimate a bulk formin turnover rate over all formin populations. We could thus establish that the bulk cortical turnover rate of the formin CYK-1 is ~0.11 s^{-1} (Figure 2D).

Combining our results with previous measurements of actin::GFP turnover rates (0.05–0.15 s^{-1}; Robin et al., 2014; Michaux et al., 2018), we estimate that formin-elongated actin filaments scale to ~6 μm on average in the 2-cell-stage *C. elegans* embryo.

Dynamics of formin at the cortex during pulsed contractions

During interphase at the 2-cell stage and during polarity establishment in the 1-cell embryo, myosin II accumulates in

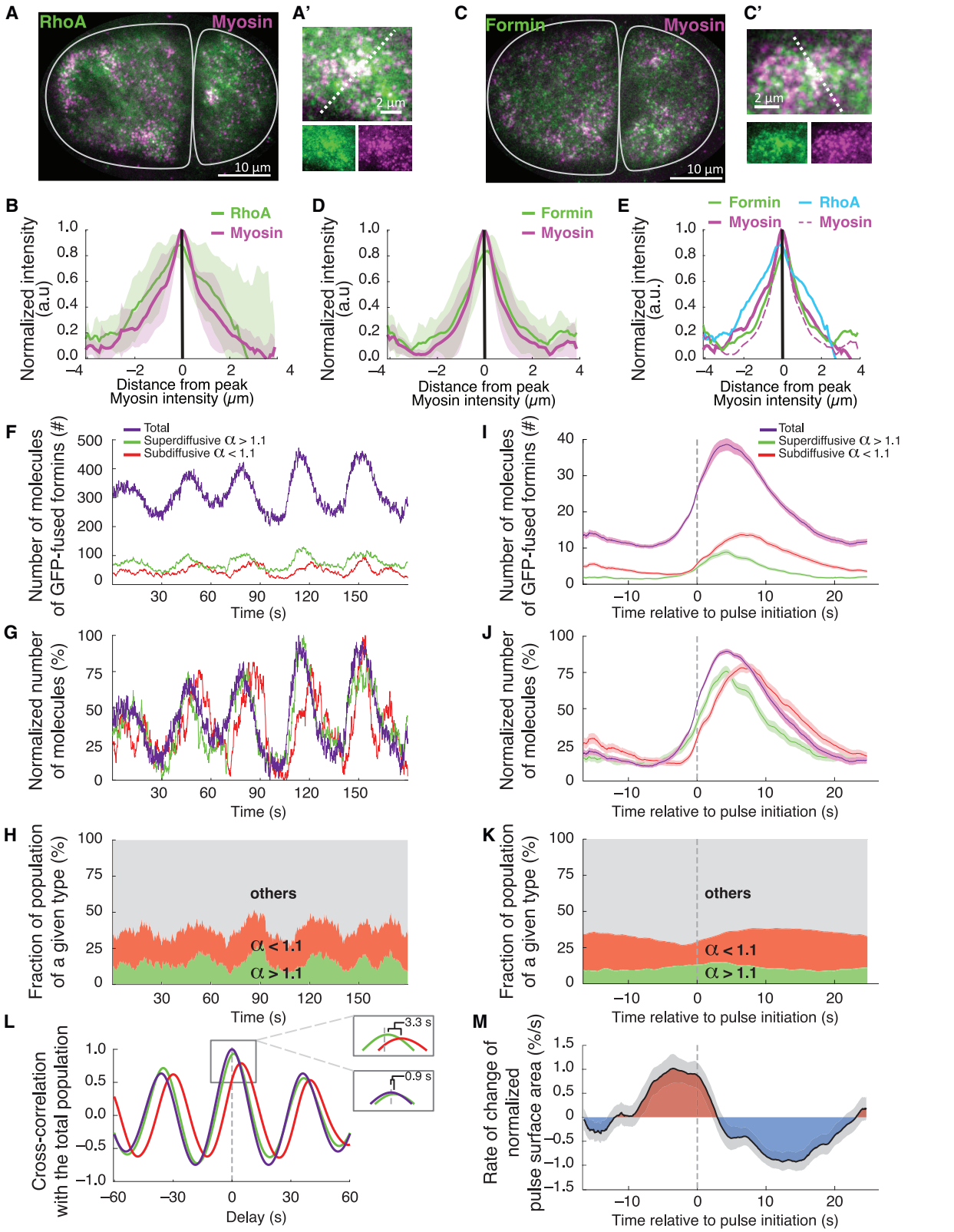

(legend on next page)

well-identifiable foci, driving local contractions of the actomyosin cortex, a process called pulsed contractions, driven by the Rho GTPase RhoA (Michaux et al., 2018). During the corresponding stage of the cell cycle, formins also displayed pulsed cortical accumulations reminiscent of RhoA/myosin pulsed dynamics (Video S2), so we decided to focus on the dynamics of formins during pulsed contractions.

We first monitored RhoA activation using a biosensor derived from the Rho-binding domain of Anillin, encompassing the Anillin homology (AH) and pleckstrin homology (PH) domains (Figures 3A–3E and S3A; Video S2; Munro et al., 2004; Piekny et al., 2005; Tse et al., 2012; Naganathan et al., 2014; Reymann et al., 2016; Michaux et al., 2018). As described previously (Michaux et al., 2018), in a strain co-expressing the RhoA biosensor with myosin (NMY-2::mRFP), we observed a spatial correlation between the localizations of myosin and the RhoA biosensor (Figures 3A, 3A′, 3B, S4E, and S4F). We further confirmed these results by visualizing ROCK, a direct downstream effector of RhoA, in a strain expressing ROCK fused with GFP from the endogenous genomic locus along with NMY-2::mRFP (Bell et al., 2020). By co-monitoring ROCK/LET-502 and myosin/NMY-2, we found, as observed previously at the 1-cell stage (Bell et al., 2020), that ROCK also accumulated in domains prefiguring myosin localization, displaying very similar spatial and temporal recruitment dynamics as our RhoA biosensor (Figures S4A–S4C, S4G, and S4H).

To test whether pulsed accumulations of formins were indeed coordinated with pulsed contractions, we compared the spatial and temporal distribution of formins and myosin II using a strain co-expressing NMY-2::mRFP and CYK-1 fused with GFP from the endogenous locus. We indeed observed that formins accumulated in broad domains that prefigured the accumulation of myosin/NMY-2 (Figures 3C, 3D, S4I, and S4J). To verify the spatial alignment between the regions where myosin accumulated, we measured the intensity across the region of accumulation, using the locus of maximal myosin intensity as a point of reference, when myosin and the co-monitored species were present. Using this approach, we observed that myosin-pulsed accumulations overlapped spatially with those of RhoA, ROCK and formin (Figures 3B, 3D, 3E, S4A–S4C, S4F, S4H, and S4J).

To infer the biochemical sequence of formin activation during pulsed contractions, we decided to measure the timing of arrival of the various formin populations over the course of a pulsed contraction. We divided our trajectories into 3 tiers: short tracks (<15 consecutive time frames), which could not be categorized into a specific population; long subdiffusive; and long superdiffusive. Using this technique, we were able to demonstrate that the ratio between the different populations was finely modulated during pulses (Figures 3F–3K). To characterize the dynamics of arrival of these populations at the cell cortex, we first focused on the kinetics of these populations on a sequence of successive pulses (Figure 3F). We observed an iterated sequence of accumulation (Figures 3G and 3H). Using cross-correlation, we measured a delay between arrival of the superdiffusive and subdiffusive populations of ~3 s (Figure 3L). This suggested that the distinct populations accumulated at the cortex in a sequence, with superdiffusive formins (hereafter called elongating formins) accumulating first, followed by subdiffusive formins (hereafter called recruited formins).

To confirm this result, we collected a series of 115 pulses from 10 embryos and quantified the dynamics of the different formin subpopulations along with the dynamics of the pulse. To show that formin accumulations were indeed coupled with pulsed contractions of the actomyosin cortex, we first measured the rate of change of the surface area of our formin pulses (Figures 3M and S8; Video S10; see the flowchart of the image analysis procedure for details). We further confirmed the contraction of the network during pulsed contractions by visualizing fiducial landmarks on the network with actin fused to GFP (ACT-1::GFP, overexpression strain, single-molecule level), along with the myosin heavy chain fused with mCherry (NMY-2::mCherry, overexpression strain) as a general marker for pulsed contractions (Figure S4D;

Figure 3. Recruited formins and actin-filament elongating formins display distinct dynamics during pulsed contractions

(A) Two-cell stage embryo showing the RhoA biosensor (green, AHPH::GFP) and myosin II (magenta, NMY-2:mKate2).

(B) Mean normalized intensity of RhoA and myosin density profile across pulses. See Figure S4 for detailed information on quantifications.

(C) Two-cell stage *C. elegans* embryo expressing formin CYK-1::GFP CRISPR (green) and myosin NMY-2:mKate2 CRISPR (magenta).

(A′ and C′) Corresponding magnified views of a single pulse. Top: both channels. Bottom: separate channels.

(D) Formin normalized mean intensity (solid green) and myosin (solid magenta) density profile along an axis drawn through pulses.

(E) Compiled results from (B) and (D).

(B, D, and E) Shaded curves: standard deviations from 18 pulses from 6 embryos.

(F) The number of total (purple), superdiffusive (green), and subdiffusive (red) formin CYK-1::GFP molecules during pulsed contractions varies periodically.

(G) Normalized number of molecules during pulsed contractions. The populations display distinct accumulation dynamics.

(H) Temporal evolution of the relative fraction of superdiffusive (green) and subdiffusive (red) subpopulations within the total population during pulsed contractions.

(I–K) Dynamics of formin CYK-1::GFP populations during pulsed contractions, averaged over 115 pulses from 10 embryos. Individual pulses are synchronized to pulse initiation (t = 0; see also Figure 5F). In (I) and (J), the number of total (purple), superdiffusive (green), and subdiffusive (red) formin CYK-1::GFP speckles during pulsed contractions. Absolute (I) and normalized (J) numbers of molecules during pulsed contractions show that superdiffusive (green), subdiffusive (red), and total formin (purple) populations accumulate with distinct dynamics.

(L) Cross-correlation with total population of superdiffusive (green), subdiffusive (red), and total (purple) formin populations. The offset shows that subdiffusive formins accumulate 3.3 s after superdiffusive formins.

(F–H and L) Population dynamics of formin CYK-1::GFP in a single embryo during 5 consecutive pulsed contractions.

(M) Rate of change of normalized pulse area during a pulsed contraction. The contraction (blue overlay) starts ~3 s after pulse initiation and ~6 s after particles start to accumulate in the pulse.

(I, J, and M) Shaded curves: SEM.

(F–M) CYK-1::GFP overexpression strain. GFP density was reduced using GFP RNAi.

Video S11). Based on these results, we then confirmed that formins accumulated at the cortex in a well-defined sequence, starting with superdiffusive followed by subdiffusive formins (Figures 3I–3K; Video S10). We further confirmed this observation using a different metric (based directly on particle displacement instead of trajectory classification) to measure this delay (Figures S3B–S3E), which yielded very similar delays (Figures S3F–S3I).

This result was somewhat surprising because, based on previous work on formin structure and domain activity, we expected an activation sequence where formins would be first recruited to the cortex by RhoA and then transferred to barbed ends of actin filaments to promote elongation (Li and Higgs, 2003, 2005; Higgs, 2005). Numerically, however, the number of recruited formins outweighed the elongating population (Figure S3F, class 1 versus class 2), suggesting that the system might be running under a regimen where formins are in excess.

Previous work (Higashida et al., 2004, 2008, 2013) also reported two formin subpopulations. In these studies, low doses of latrunculin B (Higashida et al., 2008) and gentle mechanical stimulation (Higashida et al., 2013) increased the fraction of mobile formins, and the authors demonstrated that this increase in the mobile formin fraction was caused by an increase in free G-actin concentration. In our system, however, it is difficult to imagine that pulsed contractions could drive changes in free G-actin either locally or globally. Global changes would require that individual, uncoordinated pulses, spanning ~5%–10% of the cell surface (Video S2), robustly alter the free G-actin concentration at the cell scale, even as only ~10% of actin monomers are assembled as F-actin at the cortex (Robin et al., 2014). On the other hand, we expect that local changes in free G-actin concentration would be instantly mitigated by diffusion in this almost circular system. These two arguments go against the hypothesis that local actin assembly dynamics would change free G-actin concentration at the pulse scale and lead to the observed sequence of events during local and asynchronous pulsed contractions.

Two other classes of models could explain this sequence of recruitment. The first class of models invokes delayed activation by RhoA of a formin competitor for barbed-end binding. The heterodimeric capping protein CP/CapZ, an ortholog of the *C. elegans* proteins CAP-1 and CAP-2, is a major actin-capping protein *in vivo* and might be an interesting candidate for such a mechanism. CAP-1/2 was recently described as forming a *ménage à trois* (or "decision complex"; Bombardier et al., 2015) with formins at the barbed end, weakening formin/barbed-end binding affinity and eventually leading to formin displacement (Shekhar et al., 2015).

Alternatively, in a second class of models, a non-diffusible limiting factor would be consumed locally by formins during their recruitment to the cortex. We hypothesized that one such factor could be uncapped barbed ends available for elongation, running under a regimen where formins are recruited in excess of that population of barbed ends, and elongate actin filaments from this limiting pool. Although, in this scenario, the shift from elongating to recruited/inactive formins would result from saturation of available barbed ends rather than competition between formins and capping proteins for barbed ends, such a model would essentially present the same kinetic signature.

A barbed-end saturation mechanism allows responsive actin assembly

To test whether this second model of limiting available barbed ends was plausible, we designed a simple kinetic model for CYK-1 recruitment and used this model to explore the temporal dynamics of formin accumulation (Figures S5A and S5B). We postulated that

(1) active RhoA concentration pulses periodically, with a period of 30 s (Michaux et al., 2018);
(2) cytoplasmic formins are activated by active RhoA and recruited to the cortex, shifting in the recruited population (Li and Higgs, 2005);
(3) CYK-1 formins are poor nucleators but good elongators—we considered that formins do not efficiently nucleate new filaments under physiological conditions (*in vitro* actin assembly yields ~1 new nucleated filament per 550 CYK-1 formin molecules at 2.5 μM actin and 2.5 μM profilin PFN-1 (Neidt et al., 2008);
(4) when recruited at the cortex, formins bind to barbed ends through a bimolecular reaction to drive actin assembly, becoming elongating formins; and
(5) recruited and elongating formins unbind from the cortex, returning to the cytoplasmic pool with characteristic rates of $1/\tau_{recruited}$ and $1/\tau_{elongating}$.

To seed our model, we used measured parameter values for RhoA activity, formin unbinding rates, and relative ratios between the different formin populations. Using these parameters, and provided that, in our parameters, (1) the binding reaction of recruited formins to barbed ends is very fast, and (2) barbed ends are scarce and are depleted when formin density increases, our model indeed captured the key observation that elongating formins accumulated before recruited formins (Figures 4A–4C). Under these conditions, during an early phase, elongating formins accumulate rapidly after the RhoA pulse, followed by a late phase during which recruited formins accumulate (Figures 4B, 4F, and S5C–S5H).

We favored a model for activation where RhoA binding preceded dimerization (Figure S5A), although other models (e.g., a dimer existing before the formin binds to RhoA and unfolds) are also plausible. The simulation, however, proved to be robust to these modifications of the biochemical scheme (Figures 4D and 4E).

Under a small set of assumptions, we can explain the emergence of a significant delay between recruited and elongating formins. Provided that this model is correct, saturation by CYK-1 of free barbed ends of actin filaments would allow a rapid response to pulsed RhoA activation (Figures S5C–S5H). These results demonstrate that the kinetics of the actin cytoskeleton in the early *C. elegans* embryo is wired to drive a fast response to upstream activation of actin dynamics.

Relative rates of actin assembly and contractility support polar network assembly

During pulsed contractions, cortical contractile dynamics results in peak cortical flow rates of ~0.3 $\mu m \cdot s^{-1}$ (Michaux et al., 2018; Munro et al., 2004; Nishikawa et al., 2017). In comparison, elongating formins move relatively rapidly, with a measured

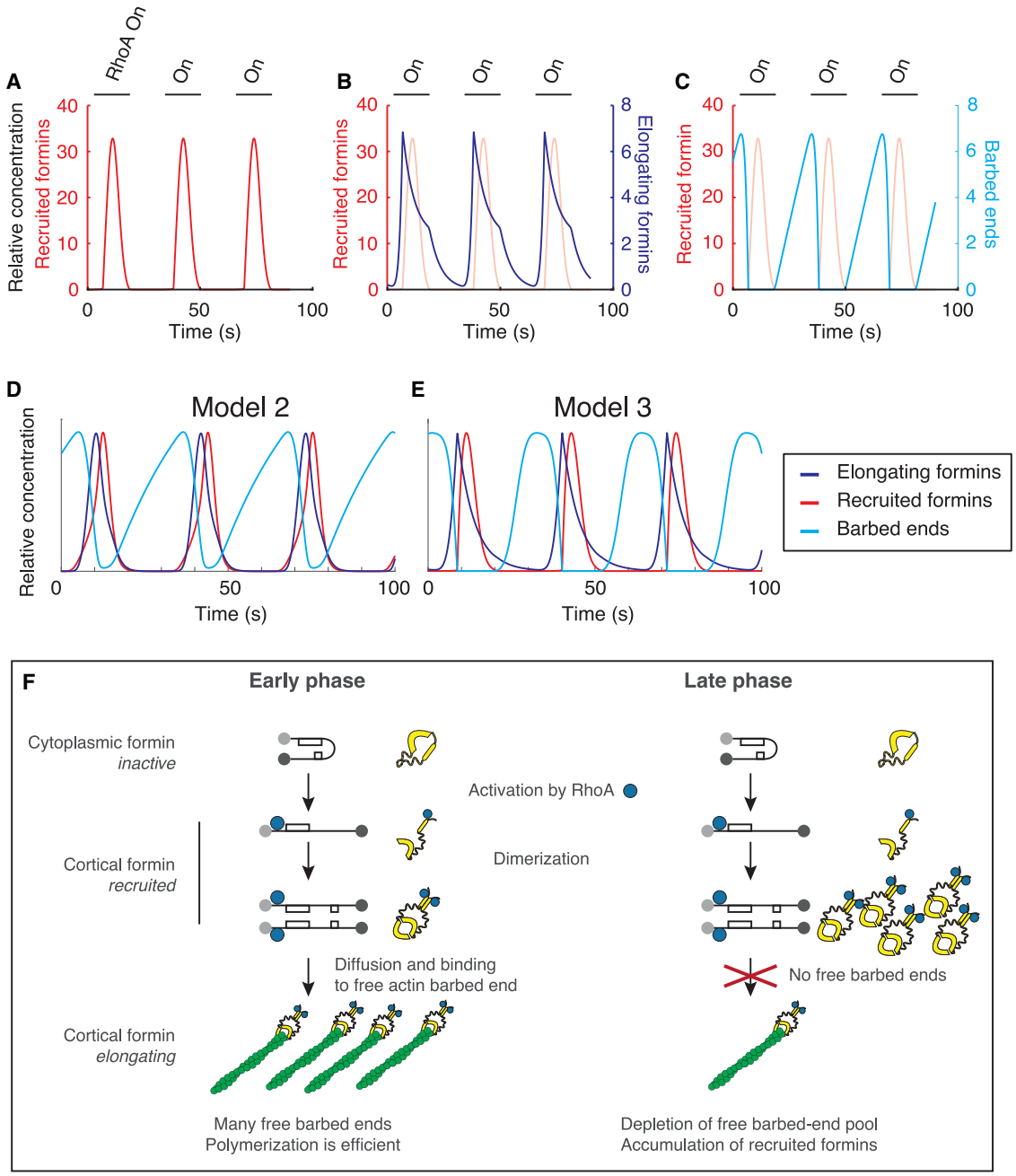

Figure 4. Modeling formin recruitment dynamics with an excess of formins over barbed ends reproduces the *in vivo* recruitment sequence

(A) Temporal dynamics of recruited formins during a sequence of 3 pulses. Red, recruited formins.

(B) Same as in (A) but with elongating formins (purple, elongating formins; light red, recruited formins). Recruited formins accumulate after elongating formins.

(C) Temporal dynamics of barbed ends (cyan, barbed ends; light red, recruited formins). Model with 2 free parameters and 4 fixed parameters, the value of which was set based on experimental measurements. Barbed ends accumulate progressively in the absence of formins (between pulses) but are rapidly used upon formin recruitment. Recruited formins are immediately converted into elongating formins so that elongating formins accumulate until depletion of the built-up barbed ends. The RhoA activation period is denoted by a black line and "Rho On" or "On."

(D) The same model with a different choice of parameter values for the free parameters of the model. The outcome is similar.

(E) Distinct model where barbed ends are generated periodically during the end of the pulsed contractions, mimicking myosin-driven actin buckling/severing activity. This model also readily reproduced the expected outcome without additional refinement.

(F) Schematic of the two phases of the pulse, representing a "first come, first served" scenario. Early phase: formins arrive at the cell surface, barbed ends are available, and recruited formins are immediately converted into elongating formins. Late phase: upon depletion of the barbed-end pool, formins are trapped in the recruited state.

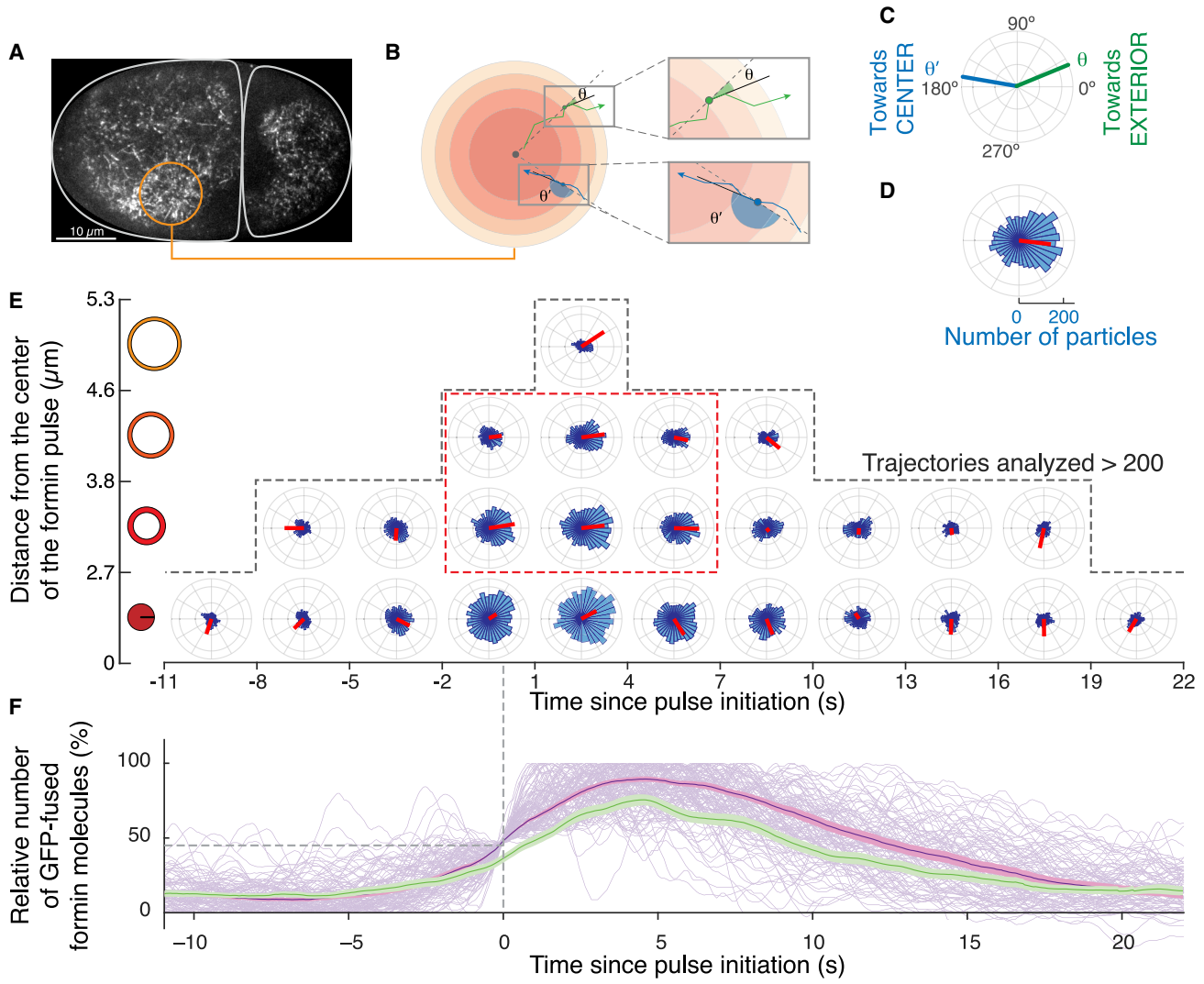

Figure 5. CYK-1 formin-driven actin-filament elongation during pulsed contractions drives formation of a transient polar actin network, barbed ends pointing out

(A) 2-cell-stage embryo expressing CYK-1::GFP. Orange circle, pulsed contraction.

(B) Measurement of the angle is performed with respect to the center of the formin pulse and the local orientation of the formin trajectory.

(C) Green (blue) track oriented with the filament barbed end pointing away from (toward) the center of the formin pulse.

(D) Angle distribution for steps of elongating formins. Average elongation orientation is shown as a red segment.

(E) Angle distribution of superdiffusive formin trajectory steps during pulsed contractions. During the peak of the pulse, around the pulse center, superdiffusive formins display, on average, an outward orientation (dashed red box). 115 pulses derived from 10 distinct embryos were used to collect more than 50,000 trajectories. Steps are binned according to the distance from the center of the formin pulse (vertical) and time from t = 0 (horizontal, 3-s intervals) to produce each rose plot. Steps are then mapped in the polar histogram as in (C). Individual pulses are synchronized to pulse initiation (t = 0, first pass at 45% of the normalized number of particles in the considered pulse), as shown in (F). Average step orientation is displayed as a red segment, with length reflecting statistical significance. Rose plots with fewer than 200 steps are not represented (the dashed line outlines plots with >200 steps).

(F) Evolution of the number of particles in a pulse; the same axis as in (E). Light purple, total number of formin particles in individual pulses; dark purple, the corresponding average and SEM; green, average and SEM for the superdiffusive population.

This is the same dataset as in Figures 3I–3L. Experiments were performed on the CYK-1::GFP overexpression strain. GFP density was reduced using GFP RNAi (see STAR Methods for additional details).

speed of 1.1–1.3 $\mu m \cdot s^{-1}$. As a consequence, even at the peak of contraction, elongating formins can "exit" the contraction zone easily and assemble an actin network of filaments up to several microns around the pulse region. To describe the architecture of this network, we measured the orientation of formin-based actin elongation during pulse assembly. We focused on elongating formins and measured the orientation of elongation radially away from the zone of formin accumulation (Figures 5A–5D), which essentially corresponds to the RhoA recruitment zone (Figure S3A). Displaying only orientations where we could collect

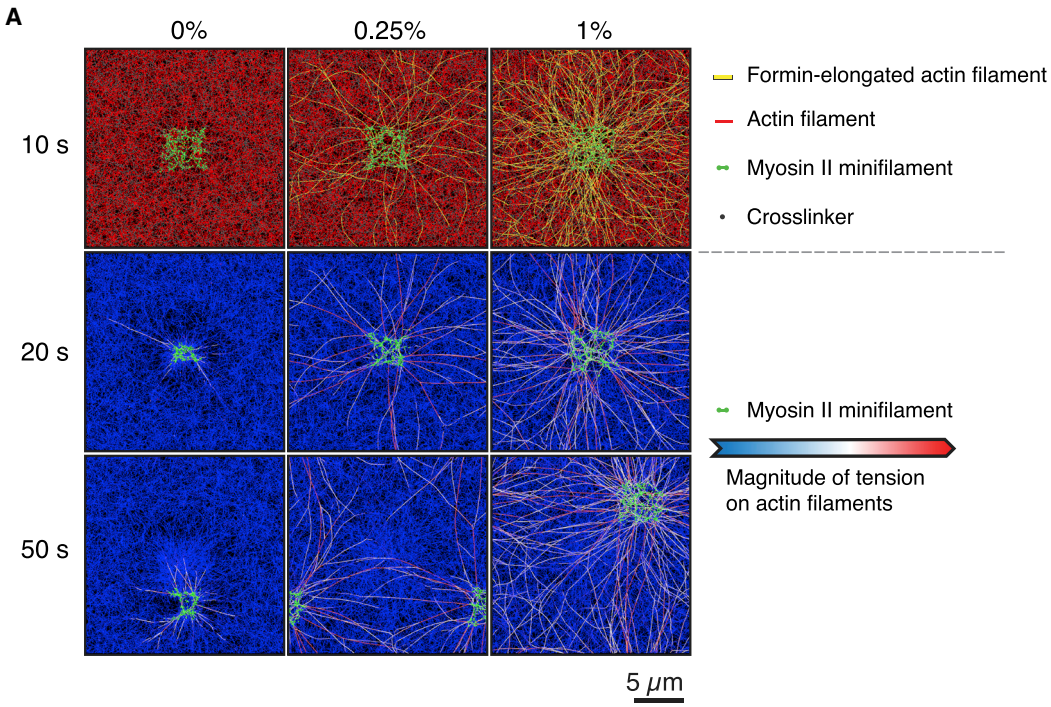

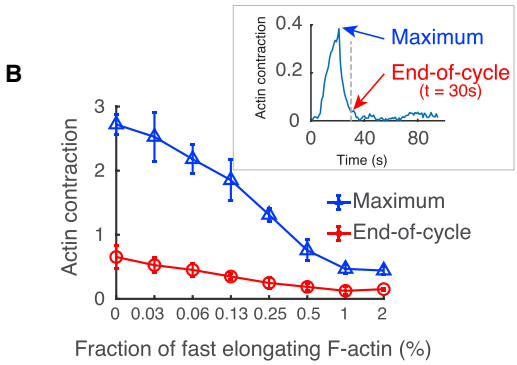

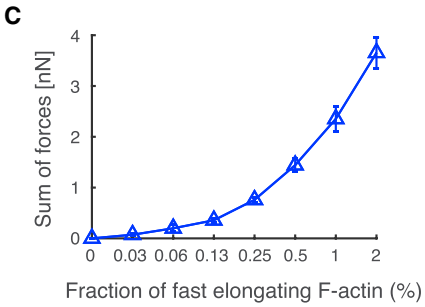

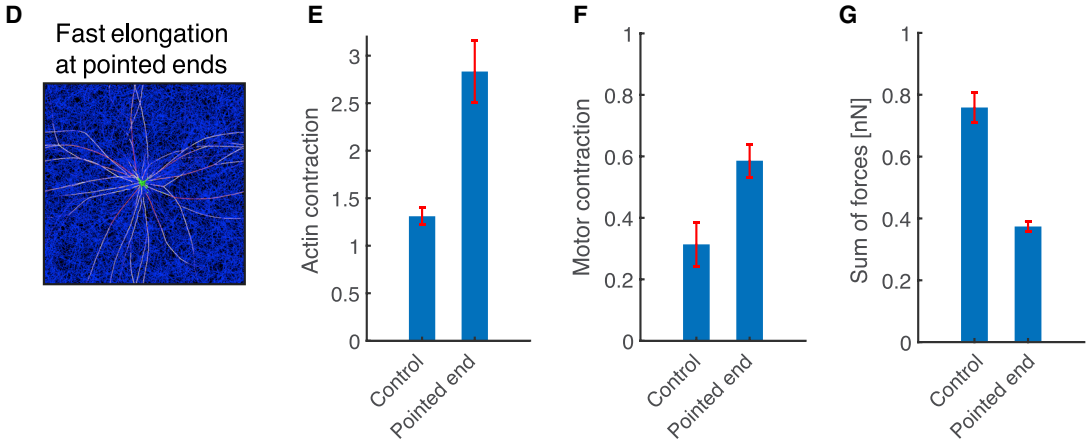

(legend on next page)

more than 200 individual elongation measurements, we observed that formins are not heavily oriented outside of the pulse time window (Figures 5E and 5F). In contrast, during the peak of assembly (corresponding approximately to the period where elongating formins >50% max.), the orientation of formin-mediated actin assembly displayed strong polarization (Figure 5E).

These results show that formins elongate the actin network with a polar dynamics, with elongation during the pulse occurring, on average, from the center of the formin pulse to the outside. Because formin-based elongation increases local actin concentration ~2-fold (Michaux et al., 2018), we propose that pulses assemble a polar actin network with barbed ends pointing outward of the pulse, akin to an "actin aster" (see discussion).

To test whether this orientation resulted purely from the transient local gradient of elongating formins between the pulsing region and its surroundings or whether additional mechanisms should be invoked, we designed a simple spatial model of formin orientation. To seed our model, we exclusively used measured parameters of formin recruitment and elongation dynamics (formin-mediated actin filament elongation rate, density, activation/elongation duration, and off-rate and pulsed contraction localizations) and generated synthetic formin pulsed accumulations with random orientations. The modeled formin dynamics displayed similar orientations, with filaments pointing outward, closely mirroring the dynamics observed *in vivo* (Figure S6; Video S12). These results demonstrate that local formin accumulation drives the assembly of a polar actin network architecture, with the majority of barbed ends pointing out.

Actomyosin network polarity supports efficient contractility

Although previous work, theoretical (Lenz et al., 2012a, 2012b) and *in vitro* (Linsmeier et al., 2016), showed that actin contraction does not require a specific network orientation, *in vivo* observations suggest that pulsed contractions form a polar actin network (Coravos and Martin, 2016). *In vitro* and computational work shows that myosin II contractility can drive polar network reorganization by barbed-end filament sorting with an opposite polarity (Kreten et al., 2018; Wollrab et al., 2018). We thus wanted to determine whether the polar network architecture we observed, barbed end pointing out combined with myosin II intrinsic polarity as a plus-end-directed motor (Howard, 2001), would not support stronger contractions or contraction over larger distances. Independently controlling network orientation and density while faithfully constraining other parameters, however, was not experimentally manageable *in vivo* or *in vitro*. We decided to turn to agent-based models of cortical mechanics to decipher the impact of network architecture on contractility.

Using our established computational model of actomyosin networks (Figure S7A; Bidone et al., 2017; Kim, 2015), we probed the roles of formin-induced F-actin elongation in cortex mechanics and architecture. Using a three-dimensional cortex-like actin meshwork (20 μm × 20 μm×100 nm), we simulated RhoA-driven pulsed contraction by locally modulating the kinetics of myosin II and F-actin elongation rates based on experimental measurements (Figure S7B). Specifically, to reproduce formin activity, we increased the elongation rate of a fraction of the barbed ends in the RhoA-activated region, resulting in rapid elongation of actin filaments for ~10 s or ~12 μm (Figure 6A, top row). We then locally turned on myosin II activity in the RhoA-activated region for 15 s and with a delay of ~5 s to reproduce delayed myosin II activation by RhoA (Videos S13, S14, and S15; Michaux et al., 2018).

Using this tailored model of pulsed contraction, we then evaluated the impact of formin activation levels on network architecture and the deployment of forces generated by myosin II. We observed that actin and myosin tended to contract toward the center of the activated region upon motor activation, peak, and then relax upon myosin II inactivation (Figures 6B, inset, and S7C). The maximum levels of actomyosin contraction decreased with formin activation levels (Figures 6B and S7D). The sum of forces experienced by formin-elongated actin filaments increased with higher formin activation levels (Figures 6A, second row, and 6C): long, formin-elongated actin filaments are cross-linked with many other short actin filaments, propagating the force generated by myosin II farther into the network (Figure S7E). We also observed that weaker local contraction and longer-range force transmission in the network prevented formation of contraction-induced actin aggregates separated from the rest of the network (Figures 6A and 6B). At high formin activation levels, myosin and actin contractions were inhibited, preventing

Figure 6. Agent-based models for the mechanics of pulsed contractions demonstrate that polar network architecture supports efficient actomyosin contractility

(A) Simulating a sequence of two successive pulsed contractions. The first pulse occurs in the center, whereas the second pulse location is stochastic. Snapshots were taken at t = 10, 20, and 50 s (during pulse initiation, the first pulse, and the second pulse, respectively; Figure S7B) with three different fractions of barbed ends undergoing quick elongation: 0%, 0.25%, and 1%. Top row: actin, myosin, and actin cross-linking protein are shown in red, green, and gray, respectively. Formin-elongated actin filaments assembled are shown in yellow. Center and bottom rows: magnitude of tensile forces on filaments, visualized using the color scaling shown below. A green overlay represents active myosin motors. Simulations have periodic boundary conditions.

(B) Maximum and end-of-cycle values (blue triangles and red circles, respectively; see inset for definition) of the actin contraction as a function of the fraction of fast-elongating actin filaments. Contraction is computed in a square region (4 × 4 μm) located within the pulsing region and indicates how homogeneous the network morphology becomes in the square region because of actin aggregation (see supplemental information for details). The inset shows the time evolution of actin contraction (fast elongation at 0.25%) with an indication of maximum and end-of-cycle values.

(C) Sum of tensile forces acting on quickly elongated filaments depending on the fraction of such filaments.

(D) A snapshot of a network with actin filaments elongated quickly from pointed ends, taken at t = 20 s. The color schemes are identical to those used in the second and third rows of (A).

(E–G) Maximum actin contraction (E), motor contraction (F), and sum of tensile forces on elongated filaments (G), quantified at t = 20 s. The motor contraction indicates how much the size of motor the population decreases compared with the initial size. In the control case, filaments are elongated from barbed ends, whereas in the other case, filaments are elongated from pointed ends.

the appearance of aggregates (Figures 6B; Video S15). As more actin filaments are elongated by formin, resistance to contraction increases, preventing local network collapse while enabling force transmission farther in the cortex.

Finally, to explore the specific impact of network polarity on contractility (Figure 5), we decided to probe the mechanics of networks displaying inverted architectures; we set out the numerical simulations to assemble actin networks with pointed ends emerging from the aster (by inverting formin polymerization dynamics, enhancing formin-mediated actin filament elongation at the pointed ends instead of the barbed end). We observed that actin and myosin contractions were enhanced (Figures 6D–6F). The forces acting on formin-elongated actin filaments were severely reduced (Figure 6G). With this network architecture, myosin motors moved toward the pulse center in a polarity sorting mechanism (Figure 6D; Wollrab et al., 2018) rather than pulling actin filaments to generate forces. These simulations showed that rapid assembly of a polar network architecture, under control of RhoA-driven pulses of formins, drives efficient actomyosin network contractility, supporting the remodeling of cell shape during pulsed contractions.

These simulation results show that actomyosin network architecture, largely governed by the kinetics of formin-mediated actin filament assembly, controls the mechanics of pulsed contraction, playing a key role to support the cellular function of pulsed contractions.

DISCUSSION

Precise architectural organization of the actomyosin network is crucial for force generation at the cell cortex. How contractile architectures are assembled in rapidly remodeling actin networks is a multiple-answer question, especially during development, when force deployment is critical for embryo morphogenesis. Here we show that formins organize a polar actin network during cortical pulsed contraction in a biochemical system primed for rapid assembly.

Our detailed description of the kinetics of actin assembly by formins shows that formins elongate actin filaments at 1.2 $\mu m \cdot s^{-1}$, or ~450 monomers$\cdot s^{-1}$. Assuming that the elongation rate scales with actin concentration in a solvent-independent manner, formin velocity may be a good indicator of the modulations of free G-actin concentration in the cell. Recent work, however, has shown that, under saturating conditions, at concentrations of actin of more than 200 μM, formin velocity actually does not scale with G-actin and profilin concentration and is controlled instead by the dissociation of profilin from the filament end (Funk et al., 2019). The decrease in elongation rates observed during cell division could then be caused by F-actin sequestration at the cleavage furrow, globally altering G-actin concentration or the actin/profilin ratio (Neidt et al., 2009).

Closely following the accumulation of two distinct populations of formins during pulsed contractions, we observed a puzzling kinetics sequence: elongating formin actually preceded recruited formins. We hypothesized that this sequence emerged directly from the kinetics of CYK-1-mediated actin assembly and designed a simple kinetics model recapitulating the main known characteristics of our system. In this model, the observed kinetics and theoretical biochemical sequence could come together under a small set of specific assumptions: (1) barbed ends available for elongation are limiting, (2) formins are recruited in large numbers, and (3) the conversion reaction is fast compared with other reactions in the system. At this point, however, we still lack tools to conclusively explore a number of related issues. How does RhoA/CYK-1 recruitment to the cell surface (compared with purely cytoplasmic dynamics) impact barbed-end dynamics (2D versus 3D effects and reduction of dimensionality are discussed further in Methods S1)? What is the molecular nature of these barbed ends available for elongation (uncapped, capped by different factors than capping proteins, etc.)? When are barbed ends generated and by which mechanisms? What are the dynamics of capping during pulses? How many barbed ends are generated? Quantitatively at least, the concentration of formins seems to be consistent with an uncapped barbed end saturation mechanism: with a binding rate constant to uncapped barbed ends of ~0.029 $nM^{-1}.s^{-}1$ and a local concentration at the pulse site of ~10 nM, we would expect a half-life for barbed ends in the range of ~3 s, consistent with our experimental observations (see supplemental information). We also do not yet have the resolution to explore the specific nature of the observed barbed ends. Are formins capable of heterodimerizing or co-assembling with other factors acting as competitive inhibitors, and could this lead to formation of inactive barbed ends?

Our numerical simulations also point to an important role of the long actin filaments assembled by formins because they seem to efficiently transmit forces in the network across long distances and avoid local network collapse. Future studies may leverage optogenetics tools to locally tune the activity of formins and test their mechanical function in cortical actomyosin contractility independent of their function in the global assembly and balance of the actin cortex.

Strikingly, the geometry of the assembled network is controlled by the geometry of the upstream signaling factors: local RhoA activation drives assembly of a polar actin network. This suggests that, at this scale, the actin architecture seems to be fundamentally driven by the spatial patterning of assembly kinetics rather than by reorganization of the actin cytoskeleton by the mechanical motor activity of myosin II (Reymann et al., 2016).

This architecture of the assembled structure, with myosin II recruited at the center of a polar actin network, barbed ends pointing out, is well tuned for actomyosin contractility. Our numerical simulations show that, although actomyosin networks can generate tension in the absence of a specific network architecture, actomyosin networks perform differently depending on their organization, and the contractile efficiency of the actomyosin network remains functionally linked to their geometry. RhoA signaling therefore converts a chemical RhoA gradient into a polar actin network architecture with a structure well adapted to the contractile function of actomyosin pulses in morphogenesis.

With precisely timed cell cycles, similar in duration to the ones in *Drosophila* syncytial embryos, lasting ~10′, *C. elegans* embryonic early development cell cycles unfold very fast (Brauchle et al., 2003), in particular compared with other early embryos; for instance, mouse embryos (20 h; Yamagata and FitzHarris, 2013), sea urchins (150 min; Chassé et al., 2016), and even ascidians (~30 min; Dumollard et al., 2013). In *C. elegans*, the

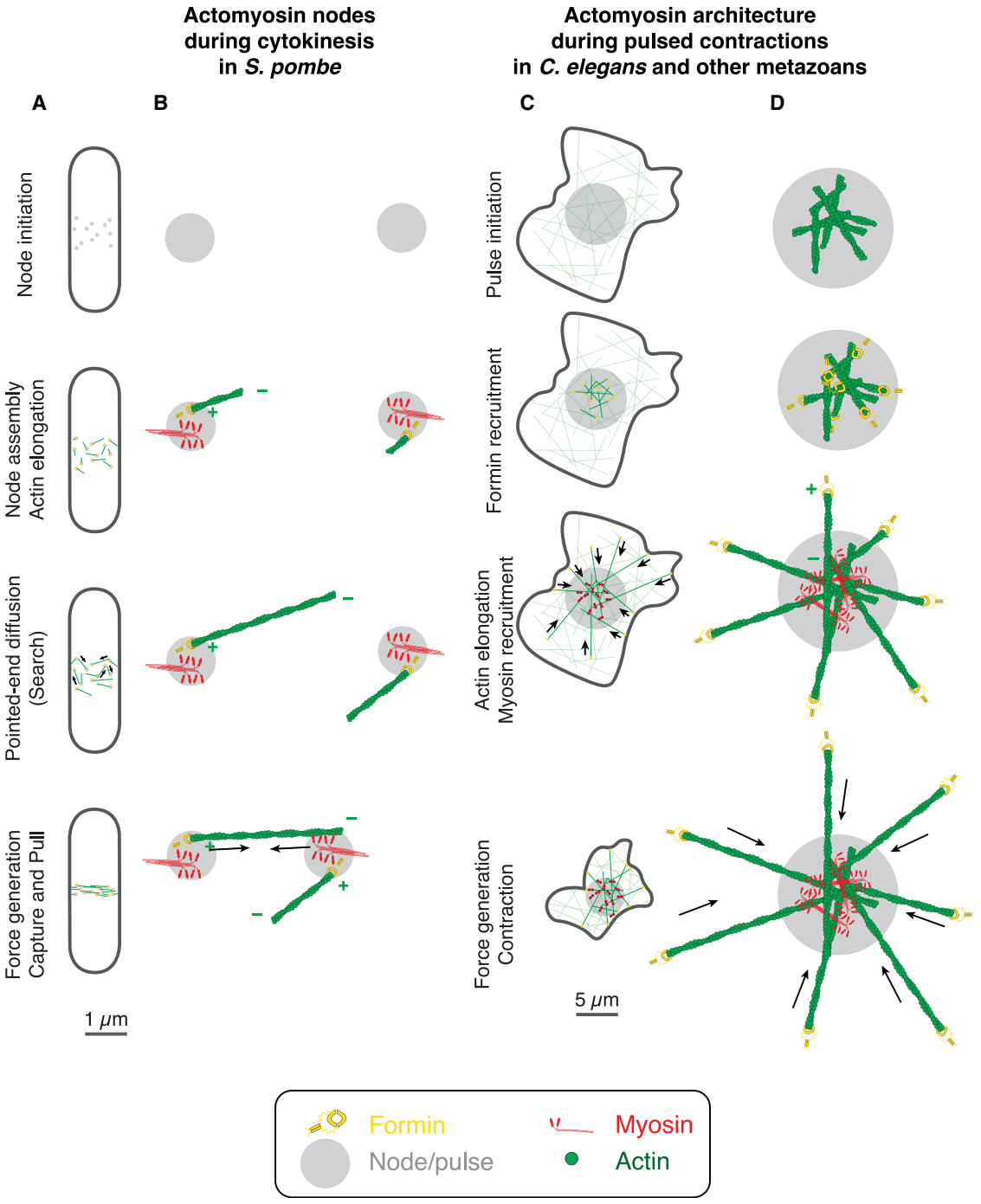

Figure 7. Compared analysis of contractility between pulsed contractility in metazoans (*Drosophila* and *C. elegans*) and yeast

(A and B) During cytokinesis in *Schizosaccharomyces pombe*, nodes form, cluster, and align, forming the contraction to drive cell division, with a process scale size of 1–2 μm. Comparatively, in metazoans, pulsed contractions drive apical constriction over 10–50 μm (A). The formin Cdc12p is recruited in the nodes and drives filament elongation (B). Pointed ends of filaments are proposed to diffuse locally and explore their environment until they are captured and pulled by Myo2p myosin filaments of another node.

(C and D) During pulsed contractions in *C. elegans,* Rho recruits formins, which elongate actin filaments, followed by myosin recruitment in the pulse center (C). Processive actin elongation by formins, recruited at the pulse site under control of Rho, drives formation of a polar actin network initiated at the pulse and extending more than 10 μm from the pulse, with actin barbed-end pointing outward (D). Myosin recruited by Rho in the center of the pulse then efficiently drives actin network contraction, pulling on actin cables assembled during the pulse to "reel in" the network toward the center of the pulse. A model inspired by the SCPR model has been proposed previously to account for contractility in cultured cells treated with small doses of LatA (Luo et al., 2013), supported by the observed recruitment of myosin at the pulse center and between pulses. In our system, we did not observe such myosin recruitment, suggesting that the two systems might be organized differently.

10-min cycles are divided roughly equally into ~5 min for mitosis and 5-min interphase with cortical pulses. As a consequence, cell polarity, compartmentalization, and cell shape changes are heavily constrained in time. An actin network primed for fast assembly, together with the polar architecture of actomyosin pulsed contractions, may set the stage for rapid and efficient contractions and cell shape changes. During gastrulation, this very same organization may thus drive fast apical constriction and subsequent timely internalization of endodermal cells.

Limitations of the study

Our study does not yet account for the interaction of other actin interaction partners at the barbed end, such as capping proteins or other formins, and our computational model does not account for signaling pathways governing pulsatile RhoA activation. Additional information about these players may thus help to interpret the results presented in this study.

Conclusions

Actomyosin network contractility is a key conserved feature of eukaryotic cells. Biochemically, the contractile structure assembled in *C. elegans* is similar to the nodes assembled in fission yeast during contractile ring assembly: formin actin filament elongators, myosin II motors, and actin cables (Vavylonis et al., 2008; Munro et al., 2004). However, several key differences separate the two contractile modules. Structurally, the sizes of the biological systems diverge strongly. At the level of the cell, a fission yeast cell is ~14 μm long and 3 μm wide during cell division, compared with 50 μm in length and 30 μm in width for the *C. elegans* embryo (Figures 7A and 7B). The two contractile macromolecular assemblies are also very different; fission yeast nodes are less than 600 nm wide and initially distant by less than 1 μm on average, whereas *C. elegans* actomyosin pulses are 3–5 μm wide and separated by 5–10 μm. The two systems are also biochemically distinct. The fission yeast formin Cdc12p elongates actin filaments with high processivity (k_{off}, ~7×10^{-5} s^{-1}) but slow speed (10.6 monomers·s^{-1} at 1.5 μM [actin], 4 μM [SpPRF], a fission yeast profilin), whereas the *C. elegans* formin CYK-1 elongates actin filaments with a lower processivity (k_{off}, ~4×10^{-3} s^{-1}) but much higher speed (63.2 monomers·s^{-1} at 1.5 μM [actin] and 4 μM [PFN-1], a *C. elegans* profilin). In the *Search-Capture-Pull-Release* (SCPR) model and related models, actin filament elongation takes place from a static barbed end (Pollard and Wu, 2010; Vavylonis et al., 2008). However, in *C. elegans*, a similar mechanism would result in filament buckling or stalling in actin filament elongation. To drive the same functional output, contraction, the molecular homologs assemble a structurally distinct, geometrically opposite architecture that is tuned to the scale of the biological system, revealing here an interesting instance of the tinkering of evolution.

STAR★METHODS

Detailed methods are provided in the online version of this paper and include the following:

- KEY RESOURCES TABLE
- RESOURCE AVAILABILITY
  - Lead contact
  - Materials availability
  - Data and code availability
- EXPERIMENTAL MODELS AND SUBJECT DETAILS
  - *C. elegans* culture and strains
- METHOD DETAILS
  - Endogenous cyk-1 GFP knock-in transgenic worm generation using CRISPR/Cas9
  - RNA interference
  - Imaging conditions
  - Tuning GFP levels to achieve single-molecule densities
  - Drug perfusion experiments
  - Assessing potential adversary effects of compression, laser exposure and GFP fusion
  - Single-molecule detection and tracking
  - Computing mean squared displacement (MSD) and alpha parameter
  - Estimating *in vivo* actin assembly parameters
  - Formin speed measurement analysis
  - Two-color imaging microscopy
  - Tracking of individual pulses of CYK-1::GFP
  - Single particles tracking and pulse analysis pipeline in Matlab
  - Numerical simulation of formin local recruitment
  - Overview of the computational model of actomyosin networks mechanics
- QUANTIFICATION AND STATISTICAL ANALYSIS

SUPPLEMENTAL INFORMATION

Supplemental information can be found online at https://doi.org/10.1016/j.celrep.2022.110868.

ACKNOWLEDGMENTS

We thank Stephan Grill, Ronen Zaidel-Bar, and Geraldine Seydoux for worm strains. We thank Marie Breau and Michel Labouesse for critical reading of the manuscript; Antoine Jégou, Michel Labouesse, Marie Breau, Flora Llense, and Teresa Ferraro for valuable discussions; members of the Robin laboratory for discussions and technical assistance; and the IBPS imaging facility, and in particular Susanne Bolte and France Lam, for excellent technical support. This work was supported by the ATIP/Avenir program (F.B.R.), the ERC-Tremplin program of CNRS (F.B.R.), the Marie Curie Program MSCA-IF 661451 (F.B.R.), and the National Institutes of Health (1R01GM126256).

AUTHOR CONTRIBUTIONS

Conceptualization, F.B.R.; methodology, S.P.G., V.C., T.K., and F.B.R.; software, S.B., F.B.R., J.L., and T.K.; formal analysis, V.C., S.P.G., J.L., T.K., and F.B.R.; resources, C.N.P., S.K.S., A.-C.R., and T.K.; writing – original draft, F.B.R.; writing – review & editing, S.P.G., V.C., T.K., and F.B.R.; visualization, V.C., S.P.G., T.K., and F.B.R.; supervision, T.K. and F.B.R.; project administration, F.B.R.; funding acquisition, T.K. and F.B.R.

DECLARATION OF INTERESTS

The authors declare no competing interests.

Received: January 22, 2021
Revised: March 13, 2022
Accepted: May 5, 2022
Published: May 31, 2022

SUPPORTING CITATIONS

The following references appear in the supplemental information: Axelrod and Wang, 1994; Berens, 2009; Berg and Purcell, 1977; Breitsprecher and Goode, 2013; Clift et al., 2005; Delbrück and Adam, 1968; Drenckhahn and Pollard, 1986; Ferrer et al., 2008; Fujiwara et al., 2014; Isambert et al., 1995; Kholodenko et al., 2000; Kishino and Yanagida, 1988; Meyer and Aebi, 1990; Miyoshi et al., 2006; Pollard and Borisy, 2003; Schafer et al., 1996; Shekhar et al., 2016; Tyska et al., 1999; Underhill and Doyle, 2004.

REFERENCES

Agarwal, P., and Zaidel-Bar, R. (2019). Principles of actomyosin regulation in vivo. Trends Cell Biol. *29*, 150–163. https://doi.org/10.1016/j.tcb.2018.09.006.

Amin, N.M., Hu, K., Pruyne, D., Terzic, D., Bretscher, A., and Liu, J. (2007). A Zn-finger/FH2-domain containing protein, FOZI-1, acts redundantly with Ce-MyoD to specify striated body wall muscle fates in the Caenorhabditis elegans postembryonic mesoderm. Development *134*, 19–29. https://doi.org/10.1242/dev.02709.

Amin, N.M., Lim, S.-E., Shi, H., Chan, T.L., and Liu, J. (2009). A conserved six-eya cassette acts downstream of Wnt signaling to direct non-myogenic versus myogenic fates in the C. Elegans postembryonic mesoderm. Dev. Biol. *331*, 350–360. https://doi.org/10.1016/j.ydbio.2009.05.538.

Axelrod, D., and Wang, M.D. (1994). Reduction-of-Dimensionality kinetics at reaction-limited cell surface receptors. Biophys. J. *66* (*3 Pt 1*), 588–600. https://doi.org/10.1016/s0006-3495(94)80834-3.

Bell, G.I. (1978). Models for the specific adhesion of cells to cells. Science *200*, 618–627. https://doi.org/10.1126/science.347575.

Bell, K.R., Werner, M.E., Doshi, A., Cortes, D.B., Sattler, A., Vuong-Brender, T., Labouesse, M., and Maddox, A.S. (2020). Novel cytokinetic ring components drive negative feedback in cortical contractility. Mol. Biol. Cell *31*, 1623–1636. https://doi.org/10.1091/mbc.E20-05-0304.

Bement, W.M., Leda, M., Moe, A., Kita, A.M., Larson, M.E., Golding, A., Pfeuti, C., Su, K.C., Miller, A., Goryachev, A., and von Dassow, G. (2015). Activator-inhibitor coupling between Rho signalling and actin assembly makes the cell cortex an excitable medium. Nat. Cell Biol. *17*, 1471–1483. https://doi.org/10.1038/ncb3251.

Berens, P. (2009). CircStat: a MATLAB toolbox for circular statistics. J. Stat. Softw. *31*, 1–21. https://doi.org/10.18637/jss.v031.i10.

Berg, H.C., and Purcell, E.M. (1977). Physics of chemoreception. Biophys. J. *20*, 193–219. https://doi.org/10.1016/S0006-3495(77)85544-6.

Bidone, T.C., Jung, W., Maruri, D., Borau, C., Kamm, R.D., and Kim, T. (2017). Morphological transformation and force generation of active cytoskeletal networks. PLoS Comput. Biol. *13*, e1005277. https://doi.org/10.1371/journal.pcbi.1005277.

Blanchoin, L., Boujemaa-Paterski, R., Sykes, Cécile, and Plastino, Julie (2014). Actin dynamics, architecture, and mechanics in cell motility. Physiol. Rev. *94*, 235–263. https://doi.org/10.1152/physrev.00018.2013.

Bombardier, J.P., Eskin, J.A., Jaiswal, R., Corrêa, I.R., Xu, M.-Q., Goode, B.L., and Gelles, J. (2015). Single-molecule visualization of a formin-capping protein 'decision complex' at the actin filament barbed end. Nat. Commun. *6*, 8707. https://doi.org/10.1038/ncomms9707.

Brauchle, M., Baumer, K., and Gönczy, P. (2003). Differential activation of the DNA replication checkpoint contributes to asynchrony of cell division in C. Elegans embryos. Curr. Biol. *13*, 819–827. https://doi.org/10.1016/s0960-9822(03)00295-1.

Breitsprecher, D., and Goode, B.L. (2013). Formins at a glance. J. Cell Sci. *126* (*Pt 1*), 1–7. https://doi.org/10.1242/jcs.107250.

Carvalho, A., Olson, S.K., Gutierrez, E., Zhang, K., Noble, L.B., Zanin, E., Desai, A., Groisman, A., and Oegema, K. (2011). Acute drug treatment in the early *C. Elegans* embryo. PLoS One *6*, e24656. https://doi.org/10.1371/journal.pone.0024656.

Chassé, H., Mulner-Lorillon, O., Boulben, S., Glippa, V., Morales, J., and Cormier, P. (2016). Cyclin B translation depends on mTOR activity after fertilization in sea urchin embryos. PLoS One *11*, e0150318. https://doi.org/10.1371/journal.pone.0150318.

Chen, Q., Nag, S., and Pollard, T.D. (2012). Formins filter modified actin subunits during processive elongation. J. Struct. Biol. *177*, 32–39. https://doi.org/10.1016/j.jsb.2011.10.005.

Clift, R., Grace, J.R., and Weber, M.E. (2005). Bubbles, Drops, and Particles (New York: Dover Publications).

Coravos, J.S., and Martin, A.C. (2016). Apical sarcomere-like actomyosin contracts nonmuscle Drosophila epithelial cells. Dev. Cell *39*, 346–358. https://doi.org/10.1016/j.devcel.2016.09.023.

Courtemanche, N. (2018). Mechanisms of formin-mediated actin assembly and dynamics. Biophys. Rev. *10*, 1553–1569. https://doi.org/10.1007/s12551-018-0468-6.

Courtemanche, N., Lee, J.Y., Pollard, T.D., and Greene, E.C. (2013). Tension modulates actin filament polymerization mediated by formin and profilin. Proc. Natl. Acad. Sci. U S A *110*, 9752–9757. https://doi.org/10.1073/pnas.1308257110.

Crocker, J.C., and Grier, D.G. (1996). Methods of digital video microscopy for colloidal studies. J. Colloid Interf. Sci. *179*, 298–310. https://doi.org/10.1006/jcis.1996.0217.

Delbrück, M., and Adam, G. (1968). Reduction of dimensionality in biological diffusion processes. In Structural Chemistry and Molecular Biology, Alexander Rich and Norman Davidson, eds. (San Francisco and London: W.H. Freeman and Co.), pp. 198–215.

Dickinson, D.J., Schwager, F., Pintard, L., Gotta, M., and Goldstein, B. (2017). A single-cell biochemistry approach reveals PAR complex dynamics during cell polarization. Dev. Cell *42*, 416–434.e11.

Dickinson, D.J., Ward, J.D., Reiner, D.J., and Goldstein, B. (2013). Engineering the Caenorhabditis elegans genome using Cas9-triggered homologous recombination. Nat Methods *10* (*10*), 1028–1034. https://doi.org/10.1038/nmeth.2641.

Drenckhahn, D., and Pollard, T.D. (1986). Elongation of actin filaments is a diffusion-limited reaction at the barbed end and is accelerated by inert macromolecules. J. Biol. Chem. *261*, 12754–12758. https://doi.org/10.1016/s0021-9258(18)67157-1.

Dumollard, R., Hebras, C., Besnardeau, L., and McDougall, A. (2013). Beta-catenin patterns the cell cycle during maternal-to-zygotic transition in urochordate embryos. Dev. Biol. *384*, 331–342. https://doi.org/10.1016/j.ydbio.2013.10.007.

Erdmann, T., and Schwarz, U.S. (2012). Stochastic force generation by small ensembles of myosin II motors. Phys. Rev. Lett. *108*, 188101. https://doi.org/10.1103/PhysRevLett.108.188101.

Erdmann, T., Albert, P.J., and Schwarz, U.S. (2013). Stochastic dynamics of small ensembles of non-processive molecular motors: the parallel cluster model. J. Chem. Phys. *139*, 175104. https://doi.org/10.1063/1.4827497.

Ferrer, J.M., Lee, H., Chen, J., Pelz, B., Nakamura, F., Kamm, R.D., and Lang, M.J. (2008). Measuring molecular rupture forces between single actin filaments and actin-binding proteins. Proc. Natl. Acad. Sci. U S A *105*, 9221–9226. https://doi.org/10.1073/pnas.0706124105.

Fujiwara, I., Remmert, K., Piszczek, G., and Hammer, J.A. (2014). Capping protein regulatory cycle driven by CARMIL and v-1 may promote actin network assembly at protruding edges. Proc. Natl. Acad. Sci. U S A *111*, E1970–E1979. https://doi.org/10.1073/pnas.1313738111.

Funk, J., Merino, F., Venkova, L., Heydenreich, L., Kierfeld, J., Vargas, P., Raunser, S., Piel, M., and Bieling, P. (2019). Profilin and formin constitute a pacemaker system for robust actin filament growth. eLife *8*, e50963. https://doi.org/10.7554/eLife.50963.

He, L., Wang, X., Tang, H.L., and Montell, D.J. (2010). Tissue elongation requires oscillating contractions of a basal actomyosin network. Nat. Cell Biol. *12*, 1133–1142. https://doi.org/10.1038/ncb2124.

Higashida, C., Miyoshi, T., Fujita, A., Oceguera-Yanez, F., Monypenny, J., Andou, Y., Narumiya, S., and Watanabe, N. (2004). Actin polymerization-driven molecular movement of mDia1 in living cells. Science *303*, 2007–2010. https://doi.org/10.1126/science.1093923.

Higashida, C., Suetsugu, S., Tsuji, T., Monypenny, J., Narumiya, S., and Watanabe, N. (2008). G-actin regulates rapid induction of actin nucleation by mDia1 to restore cellular actin polymers. J. Cell Sci. *121* (*Pt 20*), 3403–3412. https://doi.org/10.1242/jcs.030940.

Higashida, C., Kiuchi, T., Akiba, Y., Mizuno, H., Maruoka, M., Narumiya, S., Mizuno, K., and Watanabe, N. (2013). F- and G-actin homeostasis regulates mechanosensitive actin nucleation by formins. Nat. Cell Biol. *15*, 395–405. https://doi.org/10.1038/ncb2693.

Higgs, H.N. (2005). Formin proteins: a domain-based approach. Trends Biochem. Sci. *30*, 342–353. https://doi.org/10.1016/j.tibs.2005.04.014.

Howard, J. (2001). Mechanics of Motor Proteins and the Cytoskeleton (Sinauer Associates, Inc), pp. 1–7.

Isambert, H., Venier, P., Maggs, A.C., Fattoum, A., Kassab, R., Pantaloni, D., and Carlier, M.F. (1995). Flexibility of actin filaments derived from thermal fluctuations. J. Biol. Chem. *270*, 11437–11444. https://doi.org/10.1074/jbc.270.19.11437.

Jégou, A., Carlier, M.-F., and Romet-Lemonne, G. (2013). Formin mDia1 senses and generates mechanical forces on actin filaments. Nat. Commun. *4*, 1883. https://doi.org/10.1038/ncomms2888.

Johnston, R.J., Copeland, J.W., Fasnacht, M., Etchberger, J.F., Liu, J., Honig, B., and Hobert, O. (2006). An unusual Zn-finger/FH2 domain protein controls a left/right asymmetric neuronal fate decision in C. Elegans. Development *133*, 3317–3328. https://doi.org/10.1242/dev.02494.

Jung, W., Murrell, M.P., and Kim, T. (2015). F-actin cross-linking enhances the stability of force generation in disordered actomyosin networks. Comput. Part. Mech. *2* (*4*), 317–327. https://doi.org/10.1007/s40571-015-0052-9.

Kamath, R.S., and Ahringer, J. (2003). Genome-wide RNAi screening in Caenorhabditis elegans. Methods *30*, 313–321. https://doi.org/10.1016/s1046-2023(03)00050-1.

Mi-Mi, L., Votra, S., Kemphues, K., Bretscher, A., and Pruyne, D. (2012). Z-line formins promote contractile lattice growth and maintenance in striated muscles of C. Elegans. J. Cell Biol. *198*, 87–102. https://doi.org/10.1083/jcb.201202053.

Kholodenko, B.N., Hoek, J.B., and Westerhoff, H.V. (2000). Why cytoplasmic signalling proteins should Be recruited to cell membranes. Trends Cell Biol. *10*, 173–178. https://doi.org/10.1016/s0962-8924(00)01741-4.

Kim, T. (2015). Determinants of contractile forces generated in disorganized actomyosin bundles. Biomech. Model. Mechanobiol. *14*, 345–355. https://doi.org/10.1007/s10237-014-0608-2.

Kim, H.Y., and Davidson, L.A. (2011). Punctuated actin contractions during convergent extension and their permissive regulation by the non-canonical Wnt-signaling pathway. J. Cell Sci. *124*, 635–646. https://doi.org/10.1242/jcs.067579.

Kim, T., Hwang, W., Lee, H., and Kamm, R.D. (2009). Computational analysis of viscoelastic properties of crosslinked actin networks. PLoS Comput. Biol. *5*, e1000439. https://doi.org/10.1371/journal.pcbi.1000439.

Kim, H., Ishidate, T., Ghanta, K.S., Seth, M., Conte, D., J.r., Shirayama, M., and Mello, C.C. (2014). A co-CRISPR strategy for efficient genome editing in Caenorhabditis elegans. Genetics *197* (*4*), 1069–1080. https://doi.org/10.1534/genetics.114.166389.

Kishino, A., and Yanagida, T. (1988). Force measurements by micromanipulation of a single actin filament by glass needles. Nature *334*, 74–76. https://doi.org/10.1038/334074a0.

Koenderink, G.H., and Paluch, E.K. (2018). Architecture shapes contractility in actomyosin networks. Curr. Opin. Cell Biol. *50*, 79–85. https://doi.org/10.1016/j.ceb.2018.01.015.

Kreten, F.H., Hoffmann, Ch, Riveline, D., and Kruse, K. (2018). Active bundles of polar and bipolar filaments. Phys. Rev. E *98*, 012413. https://doi.org/10.1103/PhysRevE.98.012413.

Kubota, H., Miyazaki, M., Ogawa, T., Shimozawa, T., Kinosita, K., and Ishiwata, S. (2017). Biphasic effect of profilin impacts the formin mDia1 force-sensing mechanism in actin polymerization. Biophys. J. *113*, 461–471. https://doi.org/10.1016/j.bpj.2017.06.012.

Lecuit, T., and Lenne, P.-F. (2007). Cell surface mechanics and the control of cell shape, tissue patterns and morphogenesis. Nat. Rev. Mol. Cell Biol. *8*, 633–644. https://doi.org/10.1038/nrm2222.

Lenz, M., Gardel, M.L., and Dinner, A.R. (2012a). Requirements for contractility in disordered cytoskeletal bundles. New J. Phys. *14*, 033037. https://doi.org/10.1088/1367-2630/14/3/033037.

Lenz, M., Thoresen, T., Gardel, M.L., and Dinner, A.R. (2012b). Contractile units in disordered actomyosin bundles arise from F-actin buckling. Phys. Rev. Lett. *108*, 238107. https://doi.org/10.1103/PhysRevLett.108.238107.

Li, F., and Higgs, H.N. (2003). The mouse formin mDia1 is a potent actin nucleation factor regulated by autoinhibition. Curr. Biol. *13*, 1335–1340. https://doi.org/10.1016/s0960-9822(03)00540-2.

Li, F., and Higgs, H.N. (2005). Dissecting requirements for auto-inhibition of actin nucleation by the formin, mDia1. J. Biol. Chem. *280*, 6986–6992. https://doi.org/10.1074/jbc.M411605200.

Li, J., Biel, T., Lomada, P., Yu, Q., and Kim, T. (2017). Buckling-induced F-actin fragmentation modulates the contraction of active cytoskeletal networks. Soft Matter *13*, 3213–3220. https://doi.org/10.1039/c6sm02703b.

Linsmeier, I., Banerjee, S., Oakes, P.W., Jung, W., Kim, T., and Murrell, M.P. (2016). Disordered actomyosin networks are sufficient to produce cooperative and telescopic contractility. Nat. Commun. *7*, 12615–12619. https://doi.org/10.1038/ncomms12615.

Luo, W., Yu, C.H., Lieu, Z.Z., Allard, J., Mogilner, A., Sheetz, M.P., and Bershadsky, A.D. (2013). Analysis of the local organization and dynamics of cellular actin networks. J. Cell Biol. *202*, 1057–1073. https://doi.org/10.1083/jcb.201210123.

Maddox, A.S., Habermann, B., Desai, A., and Oegema, K. (2005). Distinct roles for two C. Elegans anillins in the gonad and early embryo. Development *132*, 2837–2848. https://doi.org/10.1242/dev.01828.

Mak, M., Zaman, M.H., Kamm, R.D., and Kim, T. (2016). Interplay of active processes modulates tension and drives phase transition in self-renewing, motor-driven cytoskeletal networks. Nat. Commun. *7*, 10323. https://doi.org/10.1038/ncomms10323.

Martin, A.C., Kaschube, M., and Wieschaus, E.F. (2009). Pulsed contractions of an actin-myosin network drive apical constriction. Nature *457*, 495–499. https://doi.org/10.1038/nature07522.

Mayer, M., Depken, M., Bois, J.S., Jülicher, F., and Grill, Stephan W. (2010). Anisotropies in cortical tension reveal the physical basis of polarizing cortical flows. Nature *467*, 617–621. https://doi.org/10.1038/nature09376.

Meyer, R.K., and Aebi, U. (1990). Bundling of actin filaments by alpha-actinin depends on its molecular length. J. Cell Biol. *110*, 2013–2024. https://doi.org/10.1083/jcb.110.6.2013.

Michaux, J.B., Francois B Robin, W.M.M., and Munro, E.M. (2018). Excitable RhoA dynamics drive pulsed contractions in the early C. Elegans embryo. J. Cell Biol. *217*, 4230–4252. https://doi.org/10.1083/jcb.201806161.

Miller, A.L., and Bement, W.M. (2009). Regulation of cytokinesis by Rho GTPase flux. Nat. Cell Biol. *11*, 71–77. https://doi.org/10.1038/ncb1814.

Miyoshi, T., Tsuji, T., Higashida, C., Hertzog, M., Fujita, A., Narumiya, S., Scita, G., and Watanabe, N. (2006). Actin turnover-dependent fast dissociation of capping protein in the dendritic nucleation actin network: evidence of frequent filament severing. J. Cell Biol. *175*, 947–955. https://doi.org/10.1083/jcb.200604176.

Munjal, A., and Lecuit, T. (2014). Actomyosin networks and tissue morphogenesis. Development *141*, 1789–1793. https://doi.org/10.1242/dev.091645.

Munro, E., Nance, J., and Priess, J.R. (2004). Cortical flows powered by asymmetrical contraction transport PAR proteins to establish and maintain anterior-posterior polarity in the early C. Elegans embryo. Dev. Cell *7*, 413–424. https://doi.org/10.1016/j.devcel.2004.08.001.

Murthy, K., and Wadsworth, P. (2005). Myosin-II-dependent localization and dynamics of F-actin during cytokinesis. Curr. Biol. *15*, 724–731. https://doi.org/10.1016/j.cub.2005.02.055.

Naganathan, S.R., Fürthauer, S., Nishikawa, M., Frank, J., and Grill, S.W. (2014). Active Torque Generation by the Actomyosin Cell Cortex Drives Left-Right Symmetry Breaking. eLife *3*, e04165. https://doi.org/10.7554/eLife.04165.

Naganathan, S.R., Fürthauer, S., Rodriguez, J., Fievet, B.T., Jülicher, F., Ahringer, J., Cannistraci, C.V., and Grill, S.W. (2018). Morphogenetic degeneracies in the actomyosin cortex. eLife *7*, 354. https://doi.org/10.7554/eLife.37677.

Nance, J., Munro, E.M., and Priess, J.R. (2003). C. Elegans PAR-3 and PAR-6 are required for apicobasal asymmetries associated with cell adhesion and gastrulation. Development *130*, 5339–5350. https://doi.org/10.1242/dev.00735.

Nance, J., and Priess, J.R. (2002). Cell polarity and gastrulation in C. Elegans. Development *129*, 387–397. https://doi.org/10.1242/dev.129.2.387.

Neidt, E.M., Scott, B.J., and Kovar, D.R. (2009). Formin differentially utilizes profilin isoforms to rapidly assemble actin filaments. J. Biol. Chem. *284*, 673–684. https://doi.org/10.1074/jbc.M804201200.

Neidt, E.M., Skau, C.T., and Kovar, D.R. (2008). The cytokinesis formins from the nematode worm and fission yeast differentially mediate actin filament assembly. J. Biol. Chem. *283*, 23872–23883. https://doi.org/10.1074/jbc.M803734200.

Nishikawa, M., Naganathan, S.R., Jülicher, F., and Grill, S.W. (2017). Controlling contractile instabilities in the actomyosin cortex. eLife *6*, e19595. https://doi.org/10.7554/eLife.19595.

Oegema, K., and Hyman, A.A. (2006). Cell division. WormBook, 1–40. https://doi.org/10.1895/wormbook.1.72.1.

Olson, S.K., Greenan, G., Desai, A., Müller-Reichert, T., and Oegema, K. (2012). Hierarchical assembly of the eggshell and permeability barrier in C. Elegans. J. Cell Biol. *198*, 731–748. https://doi.org/10.1083/jcb.201206008.

Pelletier, V., Gal, N., Fournier, P., and Kilfoil, M.L. (2009). Microrheology of microtubule solutions and actin-microtubule composite networks. Phys. Rev. Lett. *102*, 188303. https://doi.org/10.1103/PhysRevLett.102.188303.

Piekny, A., Werner, M., and Glotzer, M. (2005). Cytokinesis: welcome to the Rho zone. Trends Cell Biol. *15*, 651–658. https://doi.org/10.1016/j.tcb.2005.10.006.

Pollard, T.D., and Borisy, G.G. (2003). Cellular motility driven by assembly and disassembly of actin filaments. Cell *112*, 453–465. https://doi.org/10.1016/s0092-8674(03)00120-x.

Pollard, T.D., and Wu, J.-Q. (2010). Understanding cytokinesis: lessons from fission yeast. Nat. Rev. Mol. Cell Biol. *11*, 149–155. https://doi.org/10.1038/nrm2834.

Reymann, A.-C., Staniscia, F., Erzberger, A., Salbreux, G., and Grill, S.W. (2016). Cortical flow aligns actin filaments to form a furrow. eLife *5*, e17807. https://doi.org/10.7554/eLife.17807.

Robin, F.B., McFadden, W.M., Yao, B., and Munro, E.M. (2014). Single-molecule analysis of cell surface dynamics in Caenorhabditis elegans embryos. Nat. Methods *11*, 677–682. https://doi.org/10.1038/nmeth.2928.

Roh-Johnson, M., Shemer, G., Higgins, C.D., McClellan, J.H., Werts, A.D., Tulu, U.S., Gao, L., Betzig, E., Kiehart, D.P., and Goldstein, B. (2012). Triggering a cell shape change by exploiting preexisting actomyosin contractions. Science *335*, 1232–1235. https://doi.org/10.1126/science.1217869.

Rottner, K., Faix, J., Bogdan, S., Linder, S., and Kerkhoff, E. (2017). Actin assembly mechanisms at a glance. J. Cell Sci. *130*, 3427–3435. https://doi.org/10.1242/jcs.206433.

Schafer, D.A., Jennings, P.B., and Cooper, J.A. (1996). Dynamics of capping protein and actin assembly in vitro: uncapping barbed ends by polyphosphoinositides. J. Cell Biol. *135*, 169–179. https://doi.org/10.1083/jcb.135.1.169.

Shekhar, S., Kerleau, M., Kühn, S., Pernier, J., Romet-Lemonne, G., Jégou, A., and Carlier, M.-F. (2015). Formin and capping protein together embrace the actin filament in a ménage À trois. Nat. Commun. *6*, 8730. https://doi.org/10.1038/ncomms9730.

Shekhar, S., Pernier, J., and Carlier, M.-F. (2016). Regulators of actin filament barbed ends at a glance. J. Cell Sci. *129*, 1085–1091. https://doi.org/10.1242/jcs.179994.

Skruber, K., Read, T.-A., and Vitriol, E.A. (2018). Reconsidering an active role for G-actin in cytoskeletal regulation. J. Cell Sci. *131*, jcs203760. https://doi.org/10.1242/jcs.203760.

Suman, S.K., Daday, C., Ferraro, T., Vuong-Brender, T., Tak, S., Quintin, S., Robin, F., Gräter, F., and Labouesse, M. (2019). The plakin domain of C. elegans VAB-10/plectin acts as a hub in a mechanotransduction pathway to promote morphogenesis. Development. Dec 13;(24):dev183780. doi: 10.1242/dev.183780. *146* (*24*). https://doi.org/10.1242/dev.183780.

Swan, K.A., Severson, A.F., Carter, J.C., Martin, P.R., Schnabel, H., Schnabel, R., and Bowerman, B. (1998). Cyk-1: a C. Elegans FH gene required for a late step in embryonic cytokinesis. J. Cell Sci. *111* (*Pt 14*), 2017–2027. https://doi.org/10.1242/jcs.111.14.2017.

Timmons, L., and Fire, A. (1998). Specific interference by ingested dsRNA. Nature *395*, 854. https://doi.org/10.1038/27579.

Tse, Y.C., Werner, M., Longhini, K.M., Labbé, J.-C., Goldstein, B., and Glotzer, M. (2012). RhoA activation during polarization and cytokinesis of the early Caenorhabditis elegans embryo is differentially dependent on NOP-1 and CYK-4. Mol. Biol. Cell *23*, 4020–4031. https://doi.org/10.1091/mbc.E12-04-0268.

Tyska, M.J., Dupuis, D.E., Guilford, W.H., Patlak, J.B., Waller, G.S., Trybus, K.M., Warshaw, D.M., and Lowey, S. (1999). Two heads of myosin are better than one for generating force and motion. Proc. Natl. Acad. Sci. U S A *96*, 4402–4407. https://doi.org/10.1073/pnas.96.8.4402.

Underhill, P.T., and Doyle, P.S. (2004). On the coarse-graining of polymers into bead-spring chains. J. Non-Newtonian Fluid Mech. *122*, 3–31. https://doi.org/10.1016/j.jnnfm.2003.10.006.

Vavylonis, D., Wu, J.-Q., Hao, S., O'Shaughnessy, B., and Pollard, T.D. (2008). Assembly mechanism of the contractile ring for cytokinesis by fission yeast. Science *319*, 97–100. https://doi.org/10.1126/science.1151086.

Wollrab, V., Belmonte, J.M., Baldauf, L., Leptin, M., Nédélec, F., and Koenderink, G.H. (2018). Polarity sorting drives remodeling of actin-myosin networks. J. Cell Sci. *132*, jcs219717. https://doi.org/10.1242/jcs.219717.

Wu, J.-Q., and Pollard, T.D. (2005). Counting cytokinesis proteins globally and locally in fission yeast. Science *310*, 310–314. https://doi.org/10.1126/science.1113230.

Yamagata, K., and FitzHarris, G. (2013). 4D imaging reveals a shift in chromosome segregation dynamics during mouse pre-implantation development. Cell Cycle *12*, 157–165. https://doi.org/10.4161/cc.23052.

Yu, Q., Li, J., Murrell, M.P., and Kim, T. (2018). Balance between force generation and relaxation leads to pulsed contraction of actomyosin networks. Biophys. J. *115*, 2003–2013. https://doi.org/10.1016/j.bpj.2018.10.008.

Zhou, M., and Wang, Y.-L. (2008). Distinct pathways for the early recruitment of myosin II and actin to the cytokinetic furrow. Mol. Biol. Cell *19*, 318–326. https://doi.org/10.1091/mbc.e07-08-0783.

STAR★METHODS

KEY RESOURCES TABLE

REAGENT or RESOURCE	SOURCE	IDENTIFIER
Bacterial and virus strains		
L4417 plasmid	Kamath feeding library (Kamath and Ahringer, 2003)	NA
HT115(DE3) bacteria		NA
Chemicals, peptides, and recombinant proteins		
Latrunculin A	Sigma	L5163
Nocodazole	Sigma	M1404
Experimental models: Organisms/strains		
WT strain N2	CGC	Wild-type Bristol strain
EM302	Michaux et al., 2018	mgSi5[cb-UNC-119 (+) GFP::ANI-1(AH+PH)]II; nmy-2(cp52[nmy-2::mKate2 + unc-119(+)]) I; unc-119(ed3) II
FBR104	This study	cyk-1(jme06[cyk-1::mNeon])III
FBR106	This study	cyk-1(jme06[cyk-1::mNeon])III; geIs001[Pmex-5::Lifeact::mKate::nmy-2UTR, unc-119+]
FBR160	This study	cyk-1(jme14[cyk-1::eGFP])III
FBR175	This study	cyk-1(jme14[cyk-1::eGFP])III; nmy-2(cp52[nmy-2::mKate2 + unc-119(+)]) I; unc-119(ed3) III
JH1541	Courtesy of G. Seydoux	unc-119(ed4); pJH7.03 [unc-119; pie-1::GFP::actinpie-1 3′UTR]
LP229	Dickinson et al., 2017	nmy-2(cp52[nmy-2::mKate2 + LoxP unc-119(+) LoxP]) I; unc-119 (ed3) III
SWG001	Reymann et al., 2016	geIs001[Pmex-5::Lifeact::mKate::nmy-2UTR, unc-119+]
SWG282	This study	geIs008[Pcyk-1::CYK-1::GFP::cyk-1UTR, unc-119+]
Software and algorithms		
Computational model of actomyosin mechanics	Kim Taeyoon, this study	10.5281/zenodo.6486924

RESOURCE AVAILABILITY

Lead contact

Further information and requests for resources and reagents should be directed to the Lead Contact François B. Robin (francois.robin@sorbonne-universite.fr), who will address them to the appropriate author.

Materials availability

C. elegans transgenic strains generated in this study will be made available on request in exchange for reasonable compensation by requestor for processing and shipping.

Data and code availability

- Original code used in this study has been deposited and is publicly available on Zenodo: https://doi.org/10.5281/zenodo.6486924.
- Microscopy data reported in this paper will be shared by the lead contact upon request.
- Additional information required to reanalyze the data reported in this paper is available from the lead contact upon request.

EXPERIMENTAL MODELS AND SUBJECT DETAILS

C. elegans culture and strains

A list of strains used in this study is provided in Table S3.

Some strains were provided by the CGC, which is funded by NIH Office of Research Infrastructure Programs (P40 OD010440).

METHOD DETAILS

Endogenous cyk-1 GFP knock-in transgenic worm generation using CRISPR/Cas9

CRISPR knock-in of cyk-1 was carried out in Wild type *N2* genetic background using an established protocol as described in Dickinson et al.(2013). The SG sequence 5′- TCATCATCATCAGGCACAG**TGG** -3′ positioned in the last exon of cyk-1 was used as CRISPR targeting site. The SG sequence except PAM(**TGG**) was inserted in the pML2840 (Suman et al., 2019) using the overlap extension PCR method. The homologous repair plasmid was made using the GIBSON method. In brief, 1.6 kb upstream of the stop codon (left homology arm), 15-bp N-terminus linker with full-length GFP fragment and 700 bp downstream of the stop codon (right homology arm) with overlap arms were amplified and assembled in pJET1.2/blunt vector using Gibson Assembly Cloning Kit (New England Biolabs, Inc.). Full sequences are provided in Table S5. Several silent mutations were done in PAM and downstream sequence (until stop codon) in the homologous repair template to block undesired cleavage by Cas9 and avoid template switching during HDR respectively.

The cocktail of plasmids containing SG plasmid (50 ng/μl), repair template (50 ng/μl), and an co-injection marker pRF4 [*rol-6(su1006)*] (100 ng/μl) were mixed and injected into the gonads of young adult hermaphrodites (Kim et al., 2014). The rest of screening steps were followed as described earlier (Dickinson et al., 2013). Knock-in was confirmed using PCR, and DNA sequencing. The homozygous progeny were outcrossed to wild-type four times before subsequent experiments.

RNA interference

We performed RNAi using the feeding method as previously described (Timmons and Fire, 1998). The L4417 plasmid targeting *perm-1* (obtained from the Kamath feeding library (Kamath and Ahringer, 2003)) and the entire GFP sequence (generated by the Fire lab and available at http://www.addgene.org/1649/) were transformed into HT115(DE3) bacteria. Bacterial cultures for feeding were grown for 10–12 h and then induced on standard nematode nutritional growth media plates containing 50 μg/ml ampicillin and 1 mM IPTG for 16–24 h at 20–25°C, then stored at 4°C. For *perm-1* RNAi, L4 stage larvae were placed on feeding plates for 16–24 h before imaging.

Imaging conditions

We dissected gravid hermaphrodites and mounted one-cell embryos under #1.5 22-mm square coverslips in 2.5 μl of water or standard Egg Salts buffer (118 mM NaCl, 40 mM KCl, 3.4 mM CaCl2, 3.4 mM MgCl2, 5 mM HEPES, pH 7.4) containing ~500 uniformly sized polystyrene beads (15.6 ± 0.03 μm diameter, Bangs labs, #NT29N) to achieve uniform compression of the embryo surface across experiments (Robin et al., 2014).

We performed near-TIRF imaging at 19–21°C on an inverted Nikon Ti-E N-Storm microscope, equipped with motorized TIRF illuminator, Apo TIRF 100x Oil-immersion DIC N2 objective (Nikon) with 1.49–numerical aperture (NA), and PFS-S Perfect Focus unit (Nikon). Laser illumination at 488 nm and 561 nm from 300 mW solid-state sapphire laser (Coherent) was set at 30% of maximal power and delivered by fiber optics to the TIRF illuminator. Images were magnified by a 1.5× lens and collected on an Andor iXon Ultra DU-897 EMCCD camera, yielding a pixel size of 107 nm.

We controlled laser illumination angle and intensity and image acquisition using NIS Elements software (Nikon). For all experiments, we set the laser illumination angle to a standard value that was chosen empirically to approximately maximize signal intensity while maintaining even illumination across the field of view. For all SPT experiments, we collected images in streaming mode with continuous illumination at 15–60% laser intensity (100% ≈ 1.6 $\mu W \cdot \mu m^{-2}$) with 50 ms exposures to achieve frame rates of 20 frames/s.

Tuning GFP levels to achieve single-molecule densities

The quasi-steady-state densities observed during imaging depend on the initial (unobserved) densities, photobleaching rates and the intrinsic exchange kinetics of the target molecule (see main text and below). We thus determined the appropriate initial densities empirically for a given strain and experiment. We achieved these initial densities by using two methods as previously described (Robin et al., 2014). For SWG282 (CYK-1::GFP over-expression), we used RNAi directed against the GFP sequence to deplete the pool of GFP-tagged proteins. RNAi against maternal proteins typically yields an exponential decrease in the maternal protein with time of exposure (Oegema and Hyman, 2006). We controlled the degree of depletion by synchronizing larvae and sampling embryos at different times after the initiation of feeding to identify times at which discrete diffraction-limited speckles were observed at the cell surface. The optimal time was relatively consistent across experiments for a given strain and varied from 12–36 h depending on transgene expression levels and relative abundance at the cell surface vs. cytoplasm. To fine-tune density levels, we used brief (<10 s) pulses in epi-illumination mode at high laser power until adequate density was reached (Robin et al., 2014).

Drug perfusion experiments

For exposing embryos to 10 μM of Latrunculin A (Sigma L5163) or to 10 μg/mL of Nocodazole (Sigma M1404) in Egg Salts buffer during image acquisition, we used wider coverslips (22 mm x 30 mm) so that a perfusion chamber is formed between coverslip and slide, and the coverslip passes about 3 mm from the side of the slide. On the inverted microscope, this outer side of coverslip helps as support to able to deposit the perfusion volume as a drop (4 μL) while imaging. The drug solution likewise perfused by

capillarity between slide and coverslip exposes the embryos to the drug instantly. The perfusion timepoint is visible in the corresponding movies as a brief brightfield illumination and used as a reference during analysis.

Assessing potential adversary effects of compression, laser exposure and GFP fusion

We followed experimental procedures as previously tested (Robin et al., 2014). Using photobleaching to reduce GFP-tagged protein levels from full to single-molecule levels in one step resulted in arrested development. However, the laser exposure required to fine-tune densities by photobleaching, or that occurring during single-molecule imaging, did not cause embryos to arrest. In all of our single-molecule imaging experiments, we verified that embryos initiated and completed cytokinesis with normal timing or, in the case of nocodazole treated embryos multiple nuclei were present in the cell. To confirm that no adverse effects on population dynamics were associated with GFP fusion in the CYK-1::GFP CRISPR strain, we also used a CYK-1::mNeon CRISPR fusion to confirm our results (data not shown, strain available upon request).

Single-molecule detection and tracking

We used a publicly available Matlab implementation of the Crocker-Grier algorithm for single-particle detection and tracking (Pelletier et al., 2009; Crocker and Grier, 1996). In brief, the Crocker-Grier method localizes particles to subpixel resolution in individual frames by fitting local intensity peaks to a Gaussian point spread function. The two key detection parameters—peak and mean intensity of the candidate particles—are adjusted empirically for given imaging conditions using a graphical user interface. The particles are then linked frame to frame by minimizing the global displacement across all particles, given a user-chosen cutoff value for maximum particle displacement. A second parameter, the gap size, allows the possibility of ignoring 'gaps' in a trajectory due to transient failures to detect particles. These transient failures occur mainly because motion blur causes the particle intensity to fall transiently below the detection threshold.

Computing mean squared displacement (MSD) and alpha parameter

To explore particle dynamics, and we first computed the MSD. We first selected tracks of length larger than 15 times points, or 750ms, then computed the MSD at time intervals ranging from 50 ms to the duration of the track divided by 2.5. We then performed a linear fit on the logarithm of the MSD for tau < 300 ms (or 6 =15/2.5 frames, thus ensuring a "coverage" of the MSD of ~2.5-fold (meaning that, at maximal Tau, each measure of the MSD was sampled independently *at least* 2.5 times, thus minimizing measurement errors). Experimentally, after 750ms, superdiffusive particles had traveled on the order of ~900 nm, or ~9 pixels, compared with a localization resolution ~60 nm under our imaging conditions.

Estimating *in vivo* actin assembly parameters

To estimate actin concentration, we assumed that elongation rates scale linearly with actin concentration, and used previously measured peak elongation rates of ~60 monomers·s^{-1}, at 1.5 μM ATP-Actin in presence of 4 μM profilin (Neidt et al., 2009; Neidt et al., 2008).

To infer filament length, we made the following assumptions:

1. actin monomers display simple mono-exponential half-life at the cortex,
2. actin monomers display a half-life measured by tracking and smPReSS of 0.08-0.15 s (Robin et al., 2014; Michaux et al., 2018),
3. elongating formins display simple mono-exponential half-life at the filament barbed end,
4. elongating formins display a half-life measured by smPReSS of ~0.11 s (Figure 2D).

Under these assumptions, we consider solely actin filaments assembled by formins. From the perspective of an actin monomer at the time of disassembly, two options are possible:

(1) the monomer disassembles while the formin is still elongating,
(2) the formin unbinds and elongation stops before the monomer disassembles.

The "effective" elongation time of the formin on the filament is then the minimum value between (1) and (2). If actin lifetime and formin mediated actin-filament elongation time have independent exponential distributions of parameters $1/\tau_{actin}$ and $1/\tau_{formin}$, then the minimum between the two values also has exponential distribution of parameter $1/\tau_{filament} = 1/\tau_{actin} + 1/\tau_{formin}$. Under these conditions, the length of the elongated filament is:

$$L_{filament} = V_{elongation} \times \tau_{filament} = \frac{V_{elongation}}{\left(\frac{1}{\tau_{actin}} + \frac{1}{\tau_{formin}}\right)}$$

Formin speed measurement analysis

We performed single-molecule imaging as described previously. We mounted the embryos between glass slides with squares wells of 20 μm thick Epoxy and #1.5 coverslips (170 μm thick) in 2.5 μL of 0.22 μm filtered water with 15.4 μm polystyrene beads. We

imaged single molecules using 50% of 90mW of 488 nm laser, 50 ms of exposure, no delay between frames, using Photometrics 95B prime 22 mm sCMOS camera. Laser angle was set to 65°. Room temperature maintained between 19 and 20.5°C. After acquisition, we averaged two consecutive frames, in order to achieve 10 frames per second using ImageJ software (NIH Image, Bethesda, MD). We used Matlab implementation of the Crocker-Grier algorithm (Crocker and Grier, 1996) by the Kilfoil lab for single-particle tracking. We selected manually a ROI to exclude tracks from residual particles outside the cell for each stage: whole embryo for one-cell stage, anterior (AB) cell for two-cell stage, posterior AB daughter cell (ABp) for four-cell stage. Each stage was separated into three phases based on observed cortical dynamics: interphase (pulsed contractions at the cortex); mitosis (cortex "stable" with no identifiable pulsed contractions); and cytokinesis (visualized by cleavage furrow assembly).

Subsequent image analysis was performed in Matlab. We selected the trajectories based on their anomalous diffusion coefficient D and scaling exponents α. Tracks were classified as subdiffusive and superdiffusive, and selected specifically superdiffusive trajectories. In order to calculate the velocity only during elongation of actin filaments, we performed a second selection to exclude tracks displaying multiple behaviors during their lifetime (due to switches between subdiffusive and superdiffusive) and retained tracks displaying exclusively superdiffusive behavior. Finally, we screened individual trajectories manually to retain tracks that were closer to a line to avoid skewing our estimates of particle speed.

Two-color imaging microscopy

We performed single-molecule imaging as described previously. Acquisitions were performed with the Andor iXon 897 EMCCD camera. We imaged at 30% of 90 mW for 488 nm and 561 nm, with 50 ms exposure and no delay between frames (100 ms between two successive frames of the same channel). After acquisition, we averaged five consecutive frames, in order to achieve 2 frames per second using ImageJ. Pulsed contractions were selected manually and data from the intensity profile of a line drawn through the pulse is collected in a single frame. 3 pulses per embryo in 6 embryos (total of 18) were analyzed in Matlab (R2018a version). Intensities are smoothened and normalized with the local maximum value set to 1 and the immediately preceding minimum set to 0. To compare local accumulations of GFP fusions with Myosin (Figures 3A–3E), we defined the peak Myosin intensity as the point of maximal intensity in the red channel (Myosin, NMY-2::mKate2) in a cross-section through the pulse, and aligned spatially our collection of pulses based on the red channel. The information on the spatial alignment was subsequently propagated to the intensity data of the green channel (Formin, RhoA, and ROCK) to compare how the intensity in the two channels correlate spatially in our pulse collection. Intensity valued was smoothened through a rectangular window (size 3).

Tracking of individual pulses of CYK-1::GFP

We used a semi-automatic approach to identify and follow CYK-1 pulses during the two-cell stage interphase, in the anterior blastomere. We manually identified isolated pulses and drew a ROI over the surface of each pulse (about 6 μm in diameter), at about 5 frames before maximum contraction of the area can be detected. The ROI was then automatically propagated in time before and after t0, and also we designed a Matlab script (STAR Methods) allowing to adapt automatically the surface of the ROI in order to include the full trajectory of particles appearing within the ROI. To eliminate drift of the ROI associated with cortical flows, independently of CYK-1 mobility within the pulse area, we used a dedrifting routine on each particle based on the displacement of its neighbors. This was important for mobility analysis as particles registered with a global drift—and therefore displaying a persistent directional motion—would otherwise register as superdiffusive.

Single particles tracking and pulse analysis pipeline in Matlab

We designed an analysis pipeline based on Matlab scripts (STAR Methods, code available upon request) that includes CYK-1::GFP particles detection and tracking, reduction to the surface of the embryo and the AB cell, de-drifting of the trajectories and MSD analysis for segregation in different mobility populations (mainly superdiffusive CYK-1 *vs*. subdiffusive CYK-1). The further step is to intersect the matrix of all these trajectories with the specific ROI of each pulse. The final step is to normalize and align all the pulses (number of particles in time) with respect to their maximum and the minimum number of particles before, then to measure the angle orientation of every vector formed by the trajectories with respect to the center of the ROI.

Numerical simulation of formin local recruitment

We used MATLAB to compute a 2D simulation of local formin activation and actin filament elongation. Pulses were spatially and temporally distributed in an embryo's shaped mask in a random manner. Pulse were defined by a fixed 5x5 μm window (100x100 pixels) and a 20 s time window (400 frames). Pulses could not overlap in time and space. Using experimental data, density of formin recruitment, position around the center of the formin accumulating region and kinetics of recruitment could be computed in each pulse. We added 0.01 formins recruitment /μm^2/frame all over the embryo mask (independent of pulses generation) corresponding to the formin recruitment rate observed in areas away from a pulse. According to experimental data, 80% of the formin recruited were assigned to be subdiffusive while 20% of them were assigned superdiffusive. Since we aimed to study superdiffusive particles, we approximate sub-diffusive and diffusive particles as a unique population of immobile particles. Each position of superdiffusive tracks were computed using the following sequence. The length of the step R_n was picked in a normal distribution whose mean is 1.23 μm/s and standard deviation is 0.30 μm/s (values extracted from experimental data). The orientation θ_n of the step was calculated assuming a persistent length P_L of 15μm (close to the actin persistence length, (Howard, 2001)).

$$\theta_{n+1} = \theta_n + X \times \cos^{-1}\left(e^{-\frac{R}{2 \cdot P_L}}\right) \text{with } X \rightarrow \mathcal{N}(0,1)$$

Length of track were assigned using the distribution of track length for sub-diffusive and super-diffusive particles, respectively. Simulated data were analyzed using the same methods as experimental data.

Overview of the computational model of actomyosin networks mechanics

For simulations of actomyosin networks in this study, we used a well-established agent-based model of actomyosin networks based on the Langevin equation (J. Li et al., 2017; Jung et al., 2015; T. Kim et al., 2009; Mak et al., 2016). The detailed descriptions about the model and all parameters used in the model are explained in Supplementary Text and Table S1. In the model, actin filament (F-actin), motor, and ACP are coarse-grained using cylindrical segments (Figure S7A). The x, y and z positions of all the cylindrical segments are updated by the Langevin equation for Brownian dynamics. Deterministic forces in the Langevin equation include bending and extensional forces that maintain equilibrium angles formed by segments and the equilibrium lengths of segments, respectively, as well as a repulsive force acting between neighboring pairs of segments for considering volume-exclusion effects between F-actins. Due to the repulsive force, F-actins push away from each other if they overlap in space.

The formation of F-actin is initiated by a nucleation event, followed by polymerization at the barbed end and depolymerization at the pointed end. ACPs bind to F-actin without preference for cross-linking angles at a constant rate and also unbind from F-actin at a force-dependent rate determined by Bell's law (G. I. Bell, 1978). Each arm of motors binds to F-actin at a constant rate, and it then walks toward the barbed end of F-actin or unbinds from F-actin at force-dependent rates determined by the parallel cluster model (Erdmann et al., 2013; Erdmann and Schwarz, 2012). For all simulations in this study, we used a thin computational domain (20 μm×20 μm×0.1 μm) with periodic boundary conditions only in x and y directions (Figure S7B). In z direction, the boundaries of the domain exert repulsive forces on elements that moved beyond the boundaries. At the beginning of each simulation, a thin actin network is formed via self-assembly of F-actin and ACP.

For implementing RhoA activation, the domain is divided into 16 subdomains (4×4 in x and y directions). Every 30 s, one of the subdomains is randomly selected and then activated. In the activated subdomain, a fraction of the barbed ends of F-actins are randomly chosen and then undergo faster polymerization by a factor, ρ_f, for the duration of τ_f. With the reference values of ρ_f = 10 and τ_f = 10 s, F-actins are elongated by ~10 μm on average. For each simulation condition, five simulation runs are performed. After the time delay of d_M, motors in the activated subdomain are allowed to self-assemble into thick filament structures for the duration of τ_M. The reference values of d_M and τ_M are 5 s and 15 s, respectively. These active motors in the form of thick filaments can contract the part of the network in the activated subdomain. Once they become inactive after τ_M, the motors are disassembled into monomers that cannot bind to F-actin.

The code used in this study has been deposited at Zenodo and is publicly available with https://doi.org/10.5281/zenodo.6486924.

QUANTIFICATION AND STATISTICAL ANALYSIS

Quantification and statistical analysis are provided in the corresponding figure legends, Tables S1 and S2. Additional information is provided below for Figure 2.

Formin speed measurement statistical analysis (Figure 2): 23 to 40 tracks per embryo were selected. Normal distributions were verified. Two-sample Student tests (t-tests) were performed to measure the significance of the difference in speed between each stage and phase. *** means $p < 0.001$, ** means $p < 0.01$, ns: non-significant.

Cell Reports, Volume *39*

Supplemental information

Rapid assembly of a polar network architecture drives efficient actomyosin contractility

Vlad Costache, Serena Prigent Garcia, Camille N. Plancke, Jing Li, Simon Begnaud, Shashi Kumar Suman, Anne-Cécile Reymann, Taeyoon Kim, and François B. Robin

Figure S1

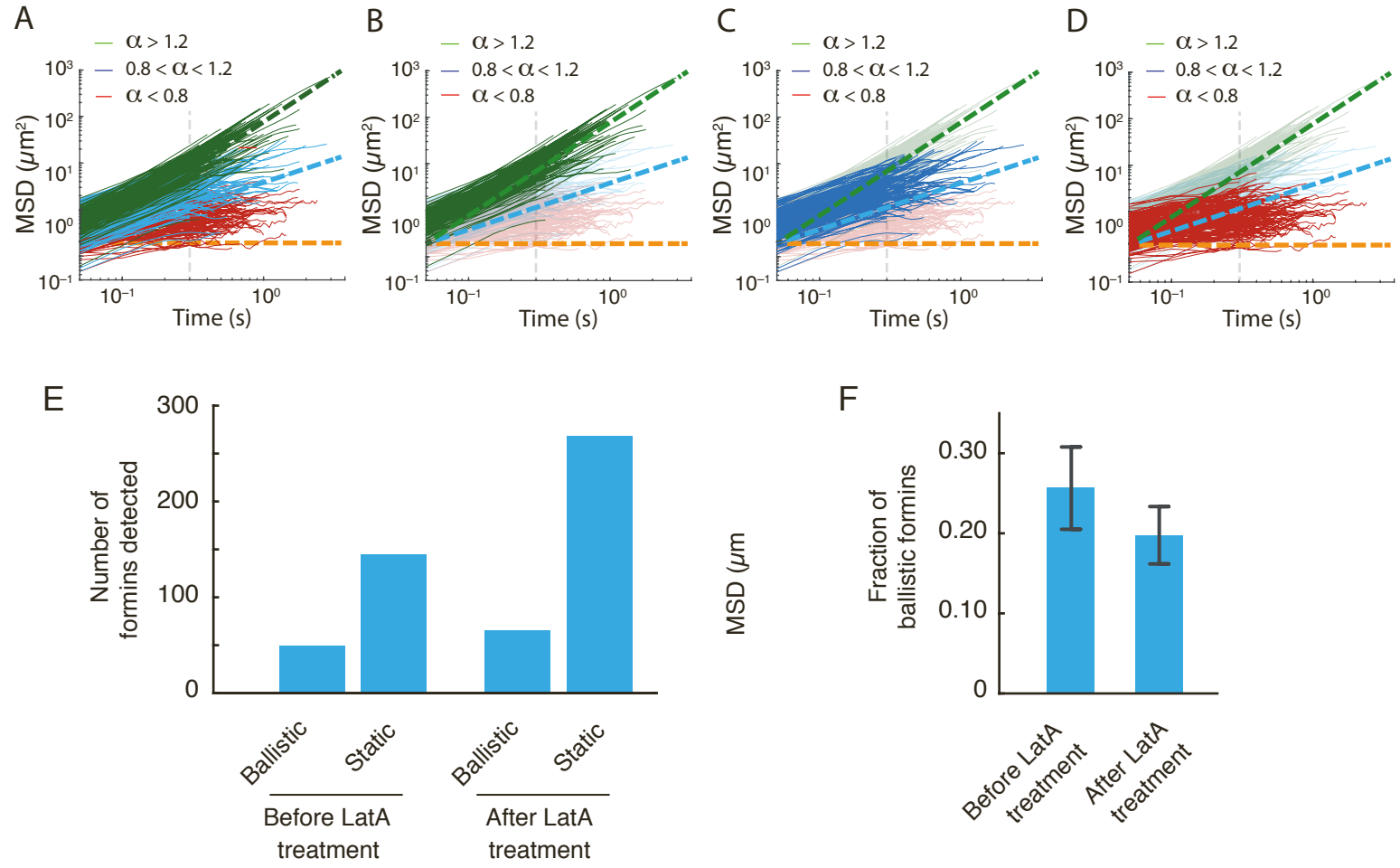
A
B
C
D
α > 1.2
0.8 < α < 1.2
α < 0.8
MSD (μm²)
Time (s)

E
Number of formins detected
300
200
100
0
Ballistic
Static
Ballistic
Static
Before LatA treatment
After LatA treatment

F
Fraction of ballistic formins
0.30
0.20
0.10
0
Before LatA treatment
After LatA treatment

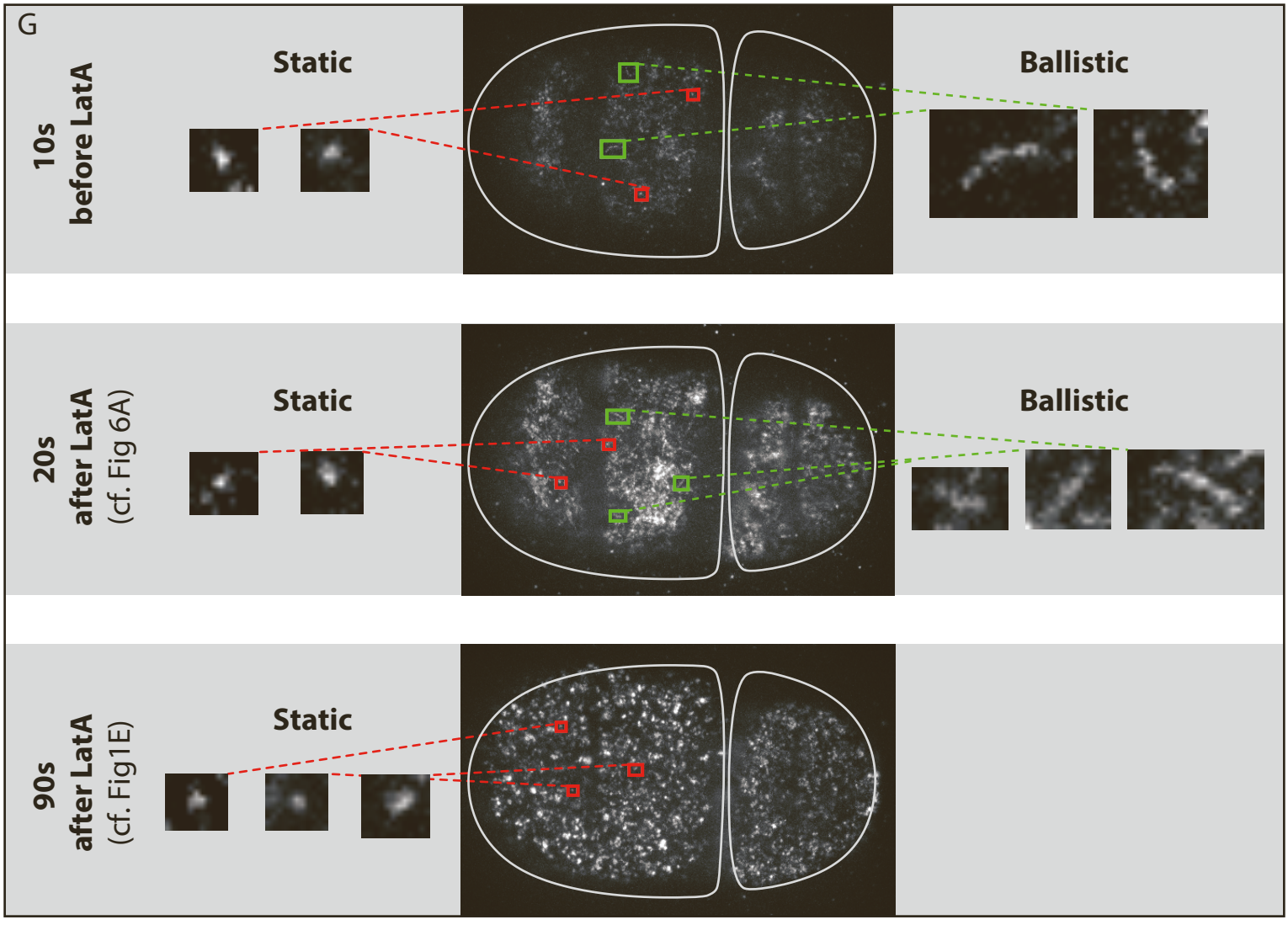
G
10s before LatA
Static
Ballistic
20s after LatA (cf. Fig 6A)
Static
Ballistic
90s after LatA (cf. Fig1E)
Static

Figure S1. **Early Effect of LatrunculinA on CYK-1 Formins at the Cell Cortex. Related to Figure 1. (A)** Number of superdiffusive and subdiffusive formins before and after treatment. **(B)** Fraction of superdiffusive formins before and after treatment. 3 different 2-c stage embryos permeabilized with Perm-1 RNAi, and treated with LatrunculinA 10μm, were analysed for the quantity and the mobility of the formins at 20s post drug perfusion, and compared to the 10 s before status of the respective embryo. Results are pooled among embryos. **(C)** Still images with Running Projections of 10 frames made out of averaged movies (3 frames AVG) so that elongating formins appear as lines (see inlets on the left hand) and immobile formins as dots (see inlets on the right hand). The horizontal regions indicate the timing with respect to the treatement with LatrunculinA. Notice that during early time (20s after treatement) elongating formins are still present and well visible. However, after 90s (the time of the analysis of different populations from Figure 1E) there are no more elongating formins visible at the cortex. **(D-G)** Mean-square displacement against lag time (MSD), detailing individual mobility populations of CYK-1 from Figure 1C (same data set). Slope curve reports on the anomalous diffusion exponent. Particles with anomalous diffusion exponent larger than 1.2 in green, between 0.8 and 1.2 in blue, and smaller than 0.8 in red. Pure superdiffusive corresponds to $\alpha = 2$ (green dashed), pure diffusive $\alpha = 1$ (blue dashed), and immobile (orange dashed). Detected mobilities correspond to different classes of behaviors. Superdiffusive display a characteristic ballistic motion (green, top panel), while subdiffusive particles appear immobile in the cortex (red, bottom). **(D)** All 3 populations superposed like in Figure 1C. **(E, F, G)** Display of trajectories from the individual populations.

Figure S2

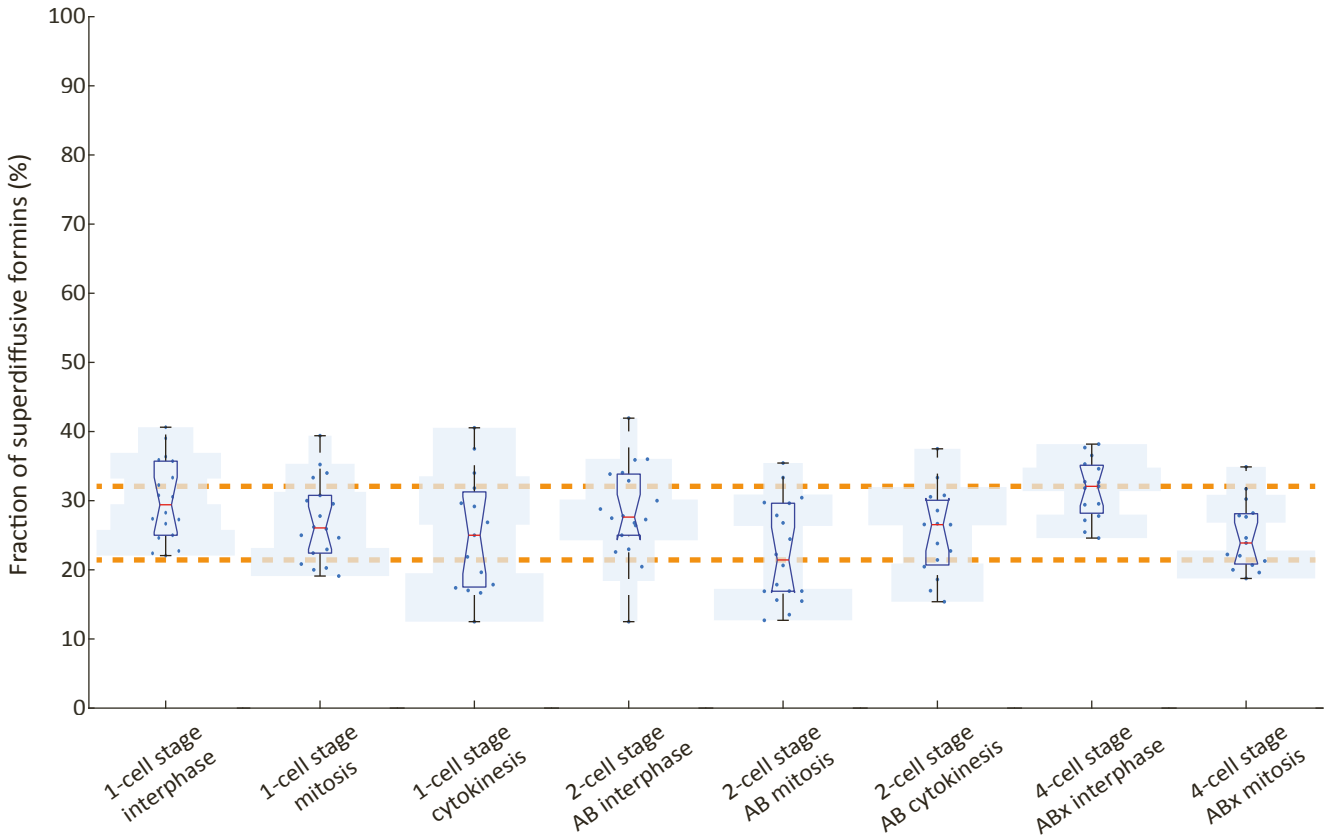
Fraction of superdiffusive formins (%)
100
90
80
70
60
50
40
30
20
10
0
1-cell stage interphase
1-cell stage mitosis
1-cell stage cytokinesis
2-cell stage AB interphase
2-cell stage AB mitosis
2-cell stage AB cytokinesis
4-cell stage ABx interphase
4-cell stage ABx mitosis

Figure S2. Ratio of superdiffusives formins in total population depending on cell cycle phase and the developmental stage. Related to Figure 2. 5 to 6 individual embryos carrying CYK-1::GFP overexpression per condition. 3 individual, same size ROI of at 3 distinct timepoints per embryo, using 1 s running projection to manually identify superdiffusive formins.

Figure S3

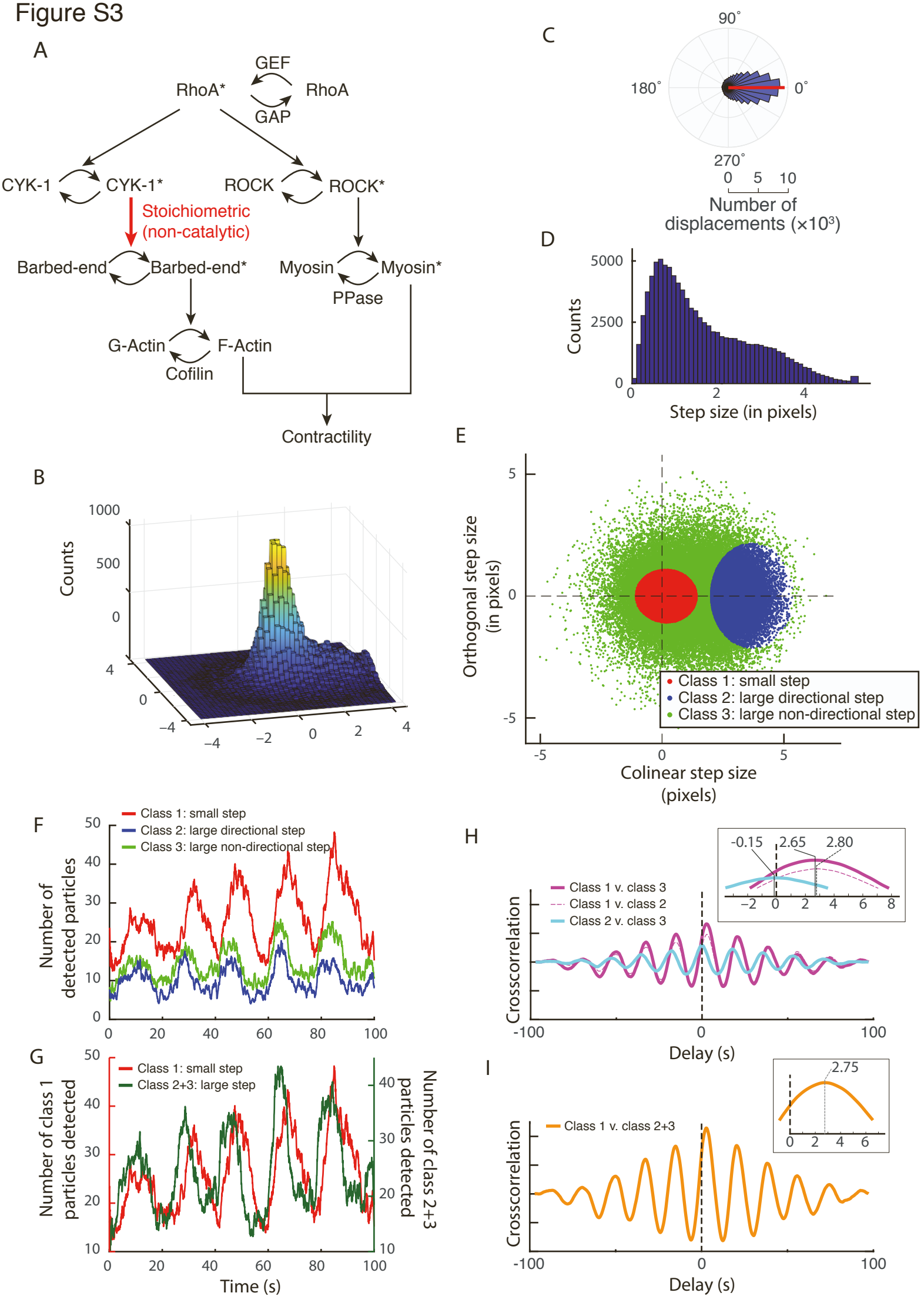
A
GEF
RhoA*
RhoA
GAP
CYK-1
CYK-1*
ROCK
ROCK*
Stoichiometric
(non-catalytic)
Barbed-end
Barbed-end*
Myosin
Myosin*
PPase
G-Actin
F-Actin
Cofilin
Contractility
B
Counts
C
90˚
180˚
0˚
270˚
0 5 10
Number of
displacements (×10³)
D
Counts
Step size (in pixels)
E
Orthogonal step size
(in pixels)
Colinear step size
(pixels)
Class 1: small step
Class 2: large directional step
Class 3: large non-directional step
F
Number of
detected particles
G
Number of class 1
particles detected
Number of class 2+3
particles detected
Class 1: small step
Class 2+3: large step
Time (s)
H
Crosscorrelation
Class 1 v. class 3
Class 1 v. class 2
Class 2 v. class 3
-0.15
2.65
2.80
Delay (s)
I
Crosscorrelation
Class 1 v. class 2+3
2.75
Delay (s)

Figure S3. Comparative localizations of ROCK/LET-502, RhoA biosensor and Formin/CYK-1. Related to Figure 3. (A) Mean of spatial normalized intensity of RhoA biosensor (solid green, AHPH::GFP) and Myosin II (solid red, NMY-2::mKate2 at endogenous locus) density profile across pulses. Shades: std from 50 pulses from 10 embryos. **(B)** Mean of spatial normalized intensity of ROCK (solid green, GFP::LET-502 at endogenous locus) and Myosin II (solid red, NMY-2::mKate2 at endogenous locus) density profile across pulses. Shades: std from 50 pulses from 10 embryos. **(C)** Merged results from (A, B). **(D)** Kymograph of Actin::GFP at single-molecule levels with NMY-2::mKate illustrating the contraction of the network during pulsed contractions. Region of interested is displayed dynamically in Movie S5. **(E, G, I)** Kymograph showing RhoA (GFP::AHPH (E)) or ROCK (GFP::LET-502 (G)) or Formin (CYK-1::GFP (I)) and Myosin (NMY-2::mKate2) pulsed contractions at the cortex of 2-cell stage *C. elegans* embryo during interphase. **(F, H, J)** Time-lapse of an individual pulsed contraction of NMY-2::mKate2 in the red channel (magenta) and RhoA (GFP::AHPH, panel F-F'"), ROCK (GFP::LET-502, panel H-H'") or Formin (CYK-1::GFP, panel J-J'") in the green channel and at the cortex of 2-cell stage *C. elegans* embryo during interphase. Below time-lapses: examples of representative individual pulses and the corresponding intensity profile, grey solid vertical line: center used for alignment in Fig. 3A-E and Fig. S4A-C. Black square: time frame picked to measure the intensity profile. White dashed line: instance of line used for the measurements presented in Fig. 3A-E and Fig. S4A-C.

Figure S4

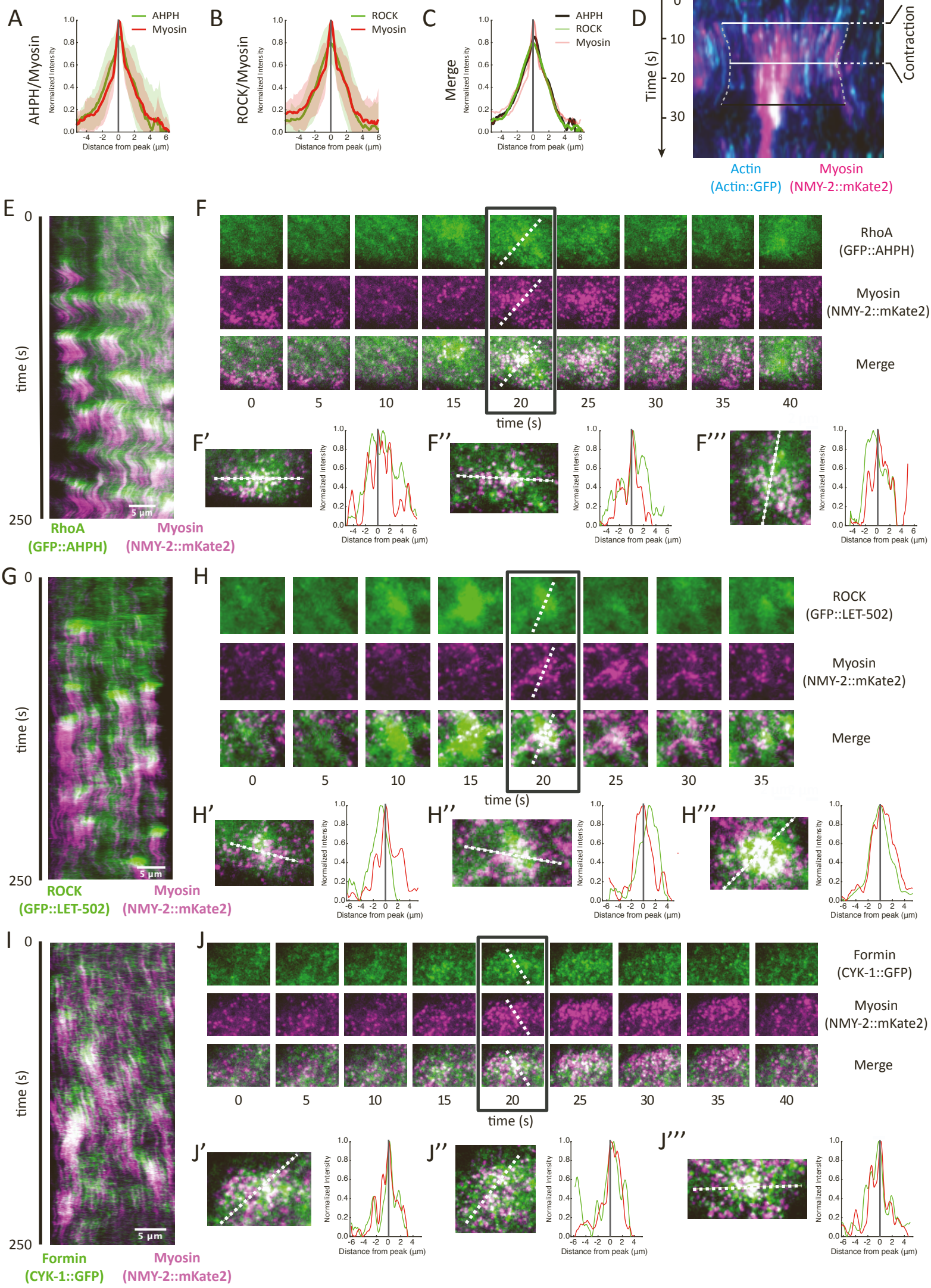
A
AHPH/Myosin
AHPH
Myosin
Normalized Intensity
Distance from peak (μm)
B
ROCK/Myosin
ROCK
Myosin
C
Merge
AHPH
ROCK
Myosin
D
Time (s)
Contraction
Actin
(Actin::GFP)
Myosin
(NMY-2::mKate2)
E
time (s)
5 μm
RhoA
(GFP::AHPH)
Myosin
(NMY-2::mKate2)
F
RhoA
(GFP::AHPH)
Myosin
(NMY-2::mKate2)
Merge
time (s)
F'
F''
F'''
G
ROCK
(GFP::LET-502)
Myosin
(NMY-2::mKate2)
H
ROCK
(GFP::LET-502)
Myosin
(NMY-2::mKate2)
Merge
time (s)
H'
H''
H'''
I
Formin
(CYK-1::GFP)
Myosin
(NMY-2::mKate2)
J
Formin
(CYK-1::GFP)
Myosin
(NMY-2::mKate2)
Merge
time (s)
J'
J''
J'''

Figure S4. Sorting and timing distinct populations of the formin CYK-1 reveals the kinetic signature of formin accumulation during pulsed contractions. Related to Figure 3. (A) Activation cascade of the formin CYK-1 by RhoA. **(B)** 3D histogram of step displacement with respect to the orientation of the previous step of the particle trajectory. Steps are taken of over 7 frames (350 ms). The histogram shows a large peak in zero, and a second additional peak around 3.5 pixels forward. **(C)** Distribution of angles of the steps in (B). **(D)** Distribution of step size, showing a merged but discernibly bimodal distribution of step sizes. **(E)** Automated classification of steps in (B) in 3 classes by 2-d gaussian fitting. Red: small/subdiffusive steps. Blue: large steps in the same direction as the previous step, corresponding to the second peak discussed in (B). Green: non-directional step, corresponding to formins changing course, or initiating elongation. **(F)** Temporal dynamics of the various step classes during a pulse, akin to Fig. 3A-C, but based on individual steps instead of whole trajectories. Green, red and blue as in (E). Note that Green and Blue curves, representing two classes of large steps (directional and non-directional) present similar temporal dynamics. **(G)** Temporal dynamics of subdiffusive steps vs "large steps"/superdiffusive steps. Dark green: merger of both classes of large steps (green and blue above). Red: small/subdiffusive steps. **(H, I)** Cross-correlation between the different populations of steps, and measured lags between these populations. Subdiffusive formins arrive ~2.7 s after superdiffusive (large steps) formins. Insets show an enlarged view of the peak region.

Figure S5

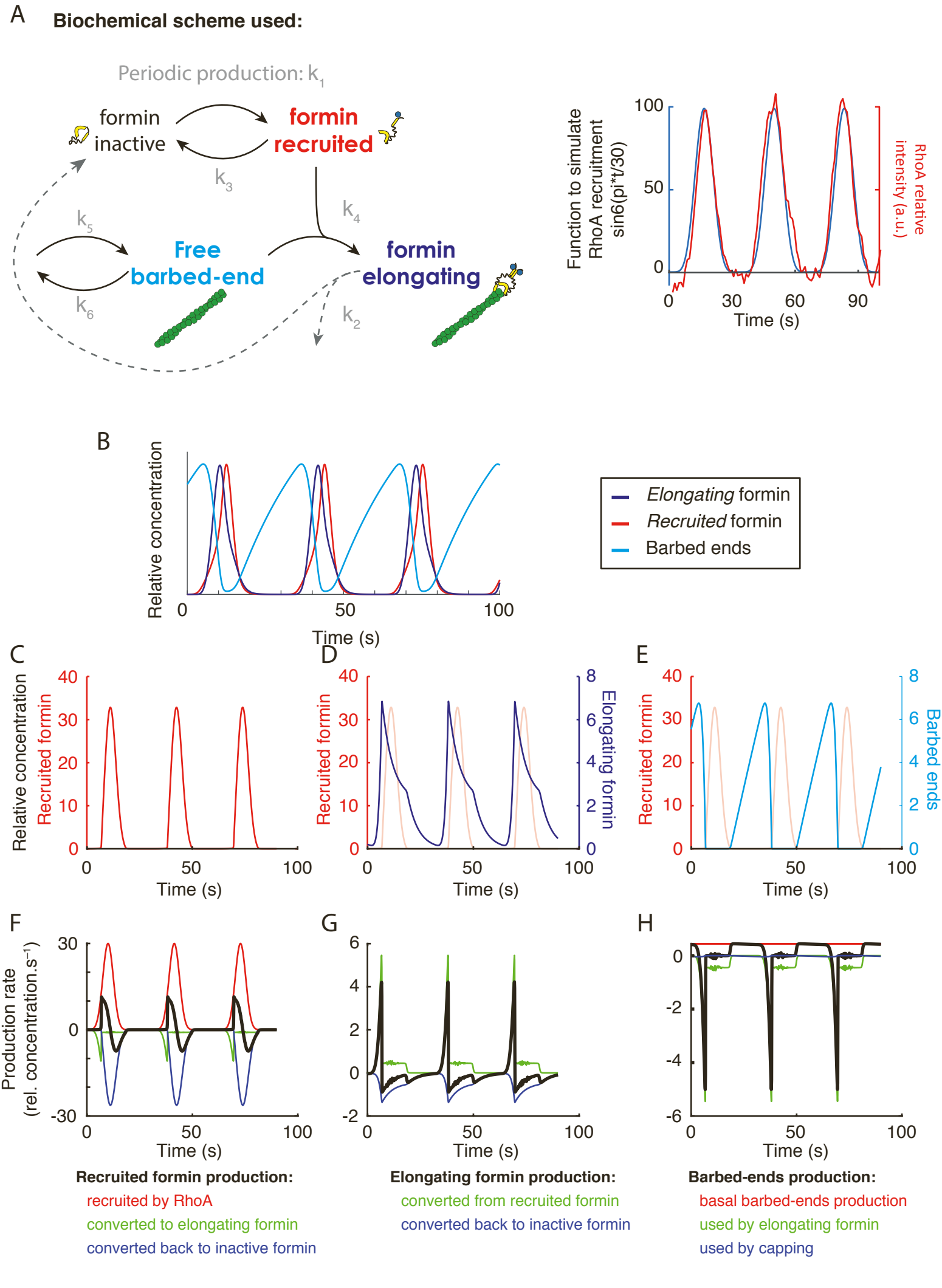
A
Biochemical scheme used:
Periodic production: k1
formin inactive
formin recruited
Free barbed-end
formin elongating
k1
k2
k3
k4
k5
k6
Function to simulate RhoA recruitment sin6(pi*t/30)
RhoA relative intensity (a.u.)
Time (s)
B
Relative concentration
Time (s)
Elongating formin
Recruited formin
Barbed ends
C
D
E
Relative concentration
Recruited formin
Elongating formin
Barbed ends
Time (s)
F
G
H
Production rate (rel. concentration.s⁻¹)
Time (s)
Recruited formin production:
recruited by RhoA
converted to elongating formin
converted back to inactive formin
Elongating formin production:
converted from recruited formin
converted back to inactive formin
Barbed-ends production:
basal barbed-ends production
used by elongating formin
used by capping

Figure S5. Mathematical simulation of a barbed end depletion model – a detailed view. Related to Figure 4. **(A)** Biochemical scheme for formin recruitment, activation and formation of a complex with barbed ends. Right panel compares function to simulate the temporal dynamics of RhoA recruitment with corresponding experimental observation. We measured the intensity of RhoA during a series of 3 consecutive pulsed contraction (red curve), and compared the dynamics with the waveform used to simulate pulsed contractions $\sin^6(\pi.t/30)$. Numerical simulations results proved robust to the specific waveform used with respect to the main conclusions. **(B)** An example of the evolution formin populations during a series of 3 pulses on the same graph. Cyan: Barbed ends, red: Recruited formins, purple: elongating formins. **(C-E)** Same as Fig. 4A-C, provided for reference for (F-H). **(C)** Temporal dynamics of recruited formins during a sequence of 3 pulses. Red: Recruited formins. **(D)** Same, with elongating formins (purple: elongating formins, light red: recruited formins). Recruited formins accumulate after elongating formins. **(E)** Temporal dynamics of barbed ends (Cyan: barbed ends, light red: recruited formins). **(F)** Sources and sinks affecting formin concentration are represented with a color code. Total derivative is presented in black, the positive contribution (production) and negative contribution (conversion) as described in the figure. **(G, H)** Same as (F) for the concentration of elongating formins (G) and barbed ends (H).

Figure S6

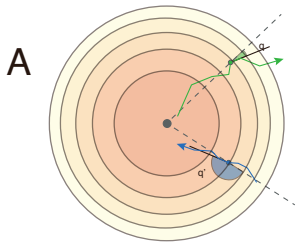

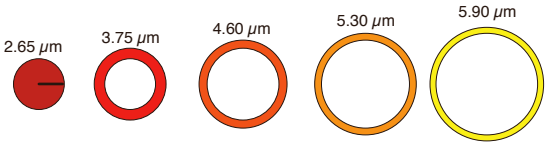

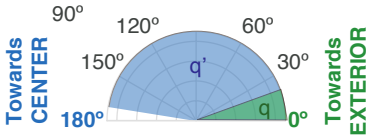

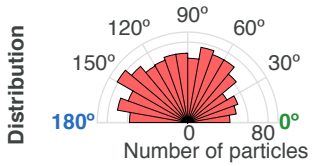

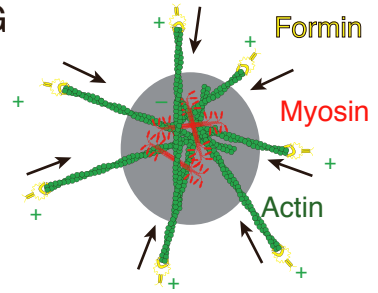

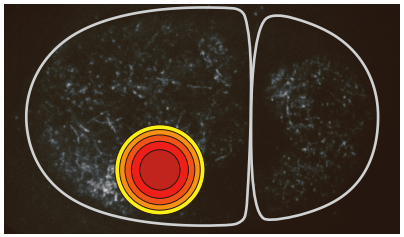

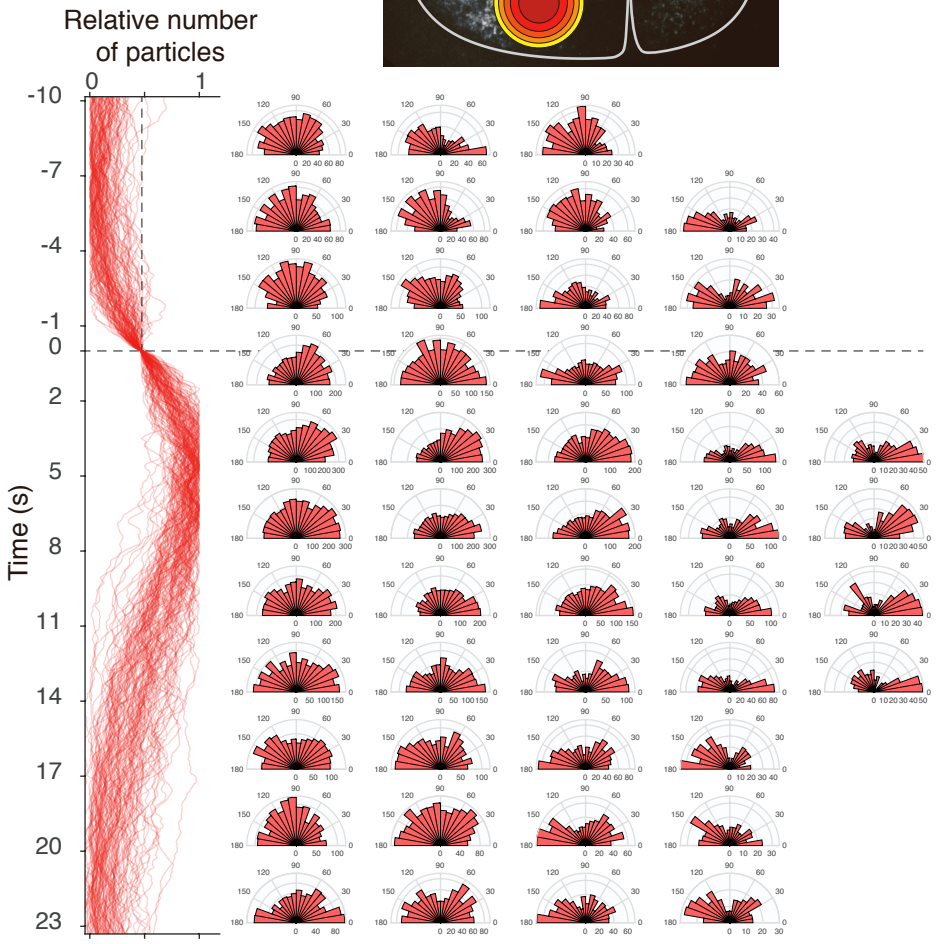

Real formin trajectories

n = 10 embryos, 115 pulses

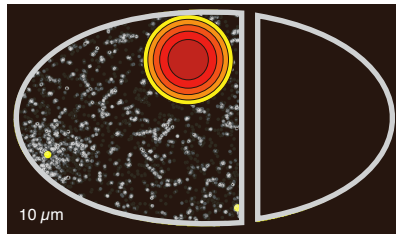

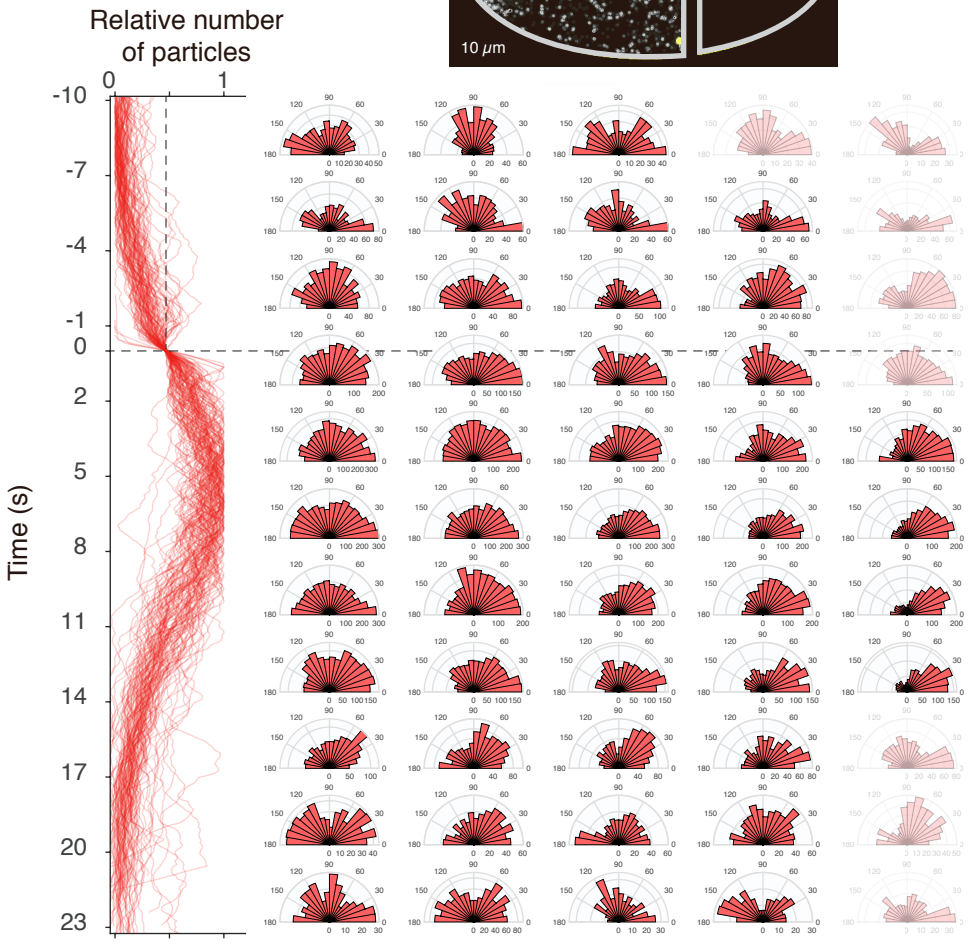

Simulated formin trajectories

n = 105 pulses

Figure S6. **Simulated CYK-1 formin trajectories display similar polar orientation (barbed ends pointing out) during pulsed contractions, as measured in real embryos. Related to Figure 5. (A)** Cartoon of a considered region of pulsed accumulation of formins, two examples of trajectories are drawn with the measured angle of the tangent from the center of the region to the vector of each particle in every position: green formin is directed outwards meanwhile blue formin is directed towards the center of the formin pulse. **(B)** The pulsed contraction region is separated in concentric circular regions that have the same surface. The radius of each circular region is indicated. **(C)** Measure of the angle for two formin trajectories is performed with respect to the center of the formin pulse and the local orientation of the formin trajectory. The green track ($\theta \sim 25°$) is oriented with the barbed end of the filament pointing away from the center of the formin pulse, while the blue track ($\theta \sim 170°$) is oriented towards the center of the formin pulse. **(D)** All the measured angles of trajectories within a circular region from the pulsed contraction are displayed as distributions on 180° polar plots. **(E)** Measured angles of formins trajectories in pulsed contractions from real embryos, with respect to a spatial coordinate (horizontal) and a time coordinate (vertical) of the pulsed accumulation. The vertical red curves display the accumulation of formin particles for each pulse. All pulses are aligned at 45% ratio between minimum and maximum, at time 0, and we signal this time with a horizontal dashed line. Dataset is the same as Fig. 5. The regions around the pulse, and when pulse intensity is high (dashed black box), display a distribution skewed towards 0, showing that the orientation of the formins point outwards of the pulse region. **(F)** Similar analysis as in (E), with simulated formin tracks based on formin kinetics extracted from measurements in real embryos (see Methods section for details). **(G)** Mechanistic model of actin filament orientation during pulsed contractions. Experiments performed on strain over-expressing CYK-1 fused with GFP, and GFP density was reduced using RNAi against GFP, through feeding – see methods.

Figure S7

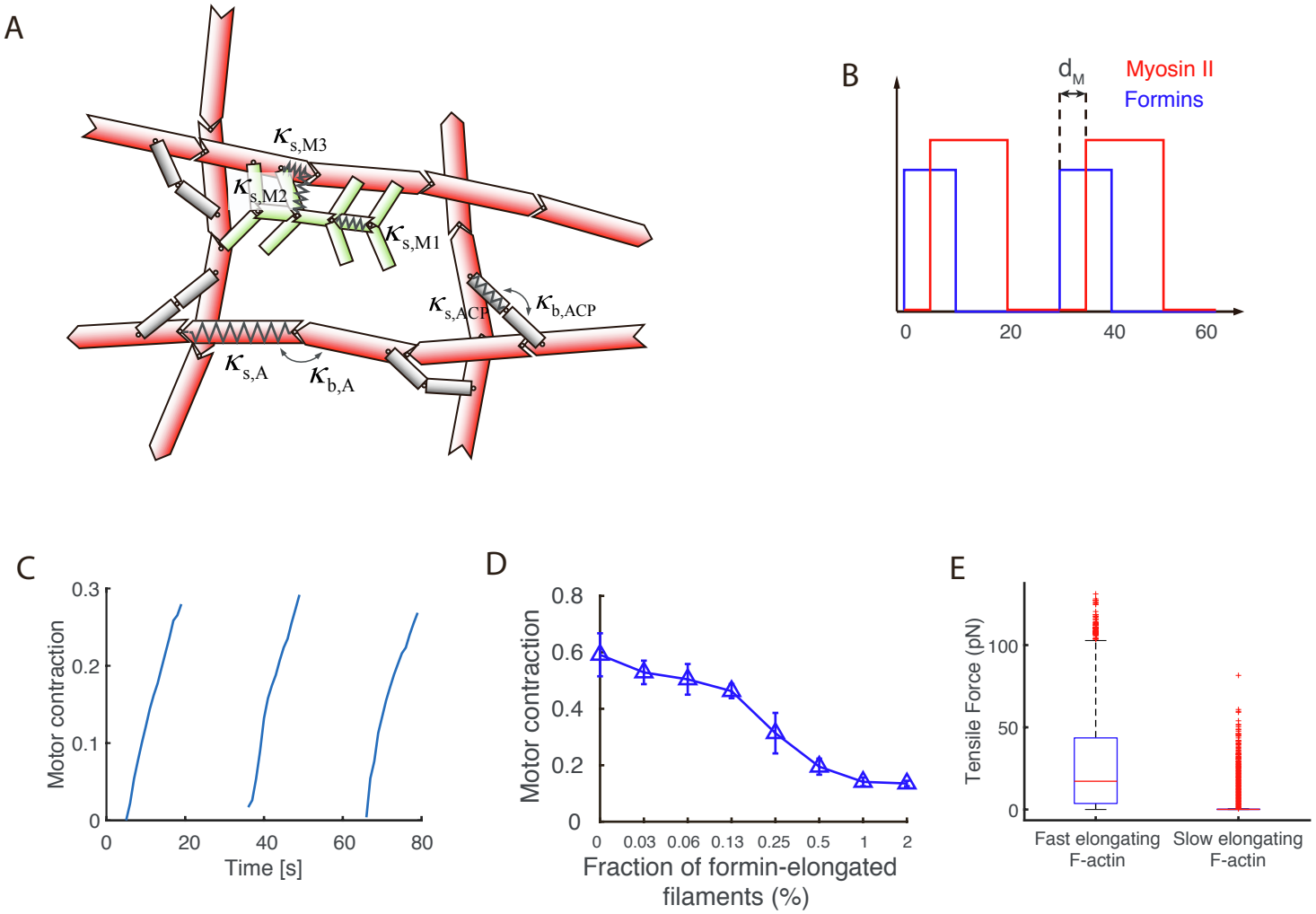
A
$\kappa_{s,M3}$
$\kappa_{s,M2}$
$\kappa_{s,M1}$
$\kappa_{s,ACP}$
$\kappa_{b,ACP}$
$\kappa_{s,A}$
$\kappa_{b,A}$
B
d_M
Myosin II
Formins
0
20
40
60
C
Motor contraction
0.3
0.2
0.1
0
0
20
40
60
80
Time [s]
D
Motor contraction
0.8
0.6
0.4
0.2
0
0
0.03
0.06
0.13
0.25
0.5
1
2
Fraction of formin-elongated filaments (%)
E
Tensile Force (pN)
100
50
0
Fast elongating F-actin
Slow elongating F-actin

Figure S7. Numerical simulation of the mechanics of actomyosin networks during pulsed contractions. Related to Figure 6. (A) Agent-based model for simulating actomyosin networks. Actin (red), actin cross-linking protein (ACP), and motor (green) are simplified by cylindrical segments. Spring and bending forces with stiffness ($\varkappa$'s) maintain equilibrium lengths and angles, respectively. **(B)** Activation scheme of myosin and formins during pulsed contractions. **(C)** An example showing the extent of myosin contraction measured in three different activated regions. **(D)** Boxplot showing the distribution of tensile forces acting on fast elongating actin filaments (left) and slow elongating filaments (right) in the control condition. **(E)** The average of the maximum values of the motor contraction shown in (C) as a function of the fraction of quickly elongating filaments.

Figure S8

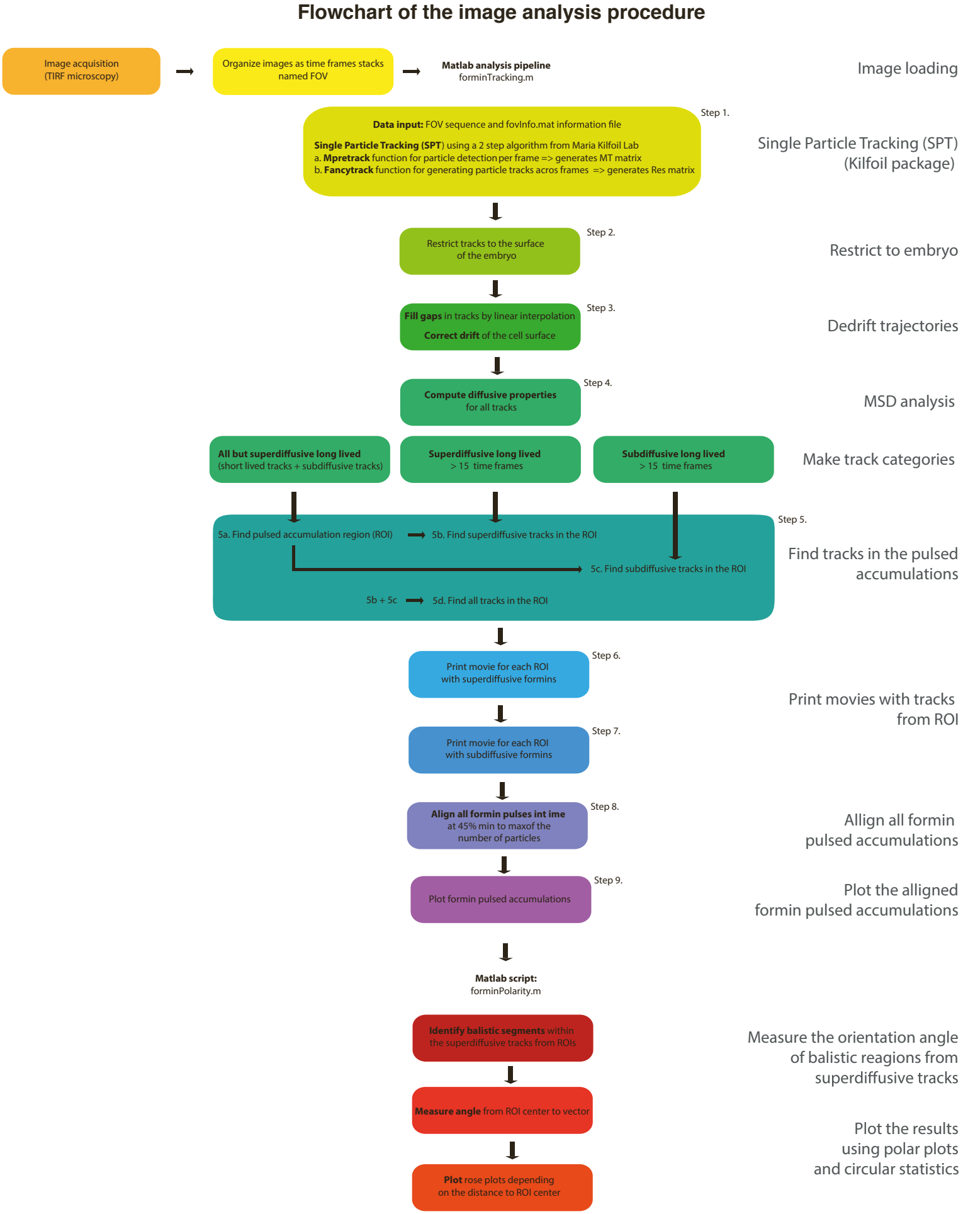
Flowchart of the image analysis procedure
Image acquisition (TIRF microscopy)
Organize images as time frames stacks named FOV
Matlab analysis pipeline forminTracking.m
Image loading
Step 1.
Data input: FOV sequence and fovInfo.mat information file
Single Particle Tracking (SPT) using a 2 step algorithm from Maria Kilfoil Lab
a. Mpretrack function for particle detection per frame => generates MT matrix
b. Fancytrack function for generating particle tracks acros frames => generates Res matrix
Single Particle Tracking (SPT) (Kilfoil package)
Step 2.
Restrict tracks to the surface of the embryo
Restrict to embryo
Step 3.
Fill gaps in tracks by linear interpolation
Correct drift of the cell surface
Dedrift trajectories
Step 4.
Compute diffusive properties for all tracks
MSD analysis
All but superdiffusive long lived (short lived tracks + subdiffusive tracks)
Superdiffusive long lived > 15 time frames
Subdiffusive long lived > 15 time frames
Make track categories
Step 5.
5a. Find pulsed accumulation region (ROI)
5b. Find superdiffusive tracks in the ROI
5c. Find subdiffusive tracks in the ROI
5b + 5c
5d. Find all tracks in the ROI
Find tracks in the pulsed accumulations
Step 6.
Print movie for each ROI with superdiffusive formins
Step 7.
Print movie for each ROI with subdiffusive formins
Print movies with tracks from ROI
Step 8.
Align all formin pulses int ime at 45% min to maxof the number of particles
Allign all formin pulsed accumulations
Step 9.
Plot formin pulsed accumulations
Plot the alligned formin pulsed accumulations
Matlab script: forminPolarity.m
Identify balistic segments within the superdiffusive tracks from ROIs
Measure angle from ROI center to vector
Measure the orientation angle of balistic reagions from superdiffusive tracks
Plot rose plots depending on the distance to ROI center
Plot the results using polar plots and circular statistics

Figure S8. Flowchart of image analysis pipeline for measuring formin trajectories mobility and their orientation during pulsed accumulations at the cortex. Related to STAR Methods. All 9 steps are organized as code sections that include single particle tracking (SPT) using a previously published algorithm (Pelletier et al, 2009). Data is further on managed as a matrix, throughout further processing steps: (1) elimination of particles outside the cell cortex, (2) correction of the drift and the MSD analysis (3) separation of the different mobility classes of formins: superdiffusive/ballistic (active formins), subdiffusive/confined (activated formins). Short-lived and subdiffusive particles serve as support to define the adaptive region of interest (ROI) corresponding to each pulsed accumulation region of formins. Pulses are then aligned in time with respect to the threshold ratio between minimum (before) and the maximum number of particles during the pulse, set at 45%. This analysis sets the stage for synchronizing across pulses the time sequences of arrival of the different formin populations at the cell cortex. A second script is used to measure the orientation angle between (1) the displacement vector of the active formins and (2) a vector starting at the center of the ROI/pulse and ending on the starting point of displacement. To select superdiffusive tracks and account for shifts between superdiffusive and subdiffusive behavior, we first selected superdiffusive tracks based on α, then for each timepoint in these tracks, we computed the ratio between start-to-end distance and travelled distance – equivalent to a straightness coefficient– over the 5 surrounding frames, and validated track regions for which the ratio was larger than an empirically determined threshold of 0.7 for more than 5 consecutive frames (250ms). Results are printed as rose plot using circular statistics toolbox (Berens, 2009). Images used in this analysis pipeline were obtained by near-TIRF microscopy at continuous 20 fps stream for 6000 frames, 16-bit, 512x512 pixels, saved as individual image sequences, and directly processed by the Matlab routine at the first step of the pipeline.

Table S1: Statistical information supporting Fig. 2A,B, *Costache, Prigent-Garcia, et al.*

	number of embryos	number of tracks	mean	median	high notch	low notch	std
1c interphase	6	240	1.2497	1.2641	1.2869	1.2412	0.1764
1c mitosis	6	240	1.272	1.2896	1.3102	1.2689	0.1626
1c cytokinesis	5	170	1.0496	1.0716	1.105	1.0382	0.2222
2c AB interphase	7	280	1.2413	1.2385	1.2617	1.2153	0.1933
2c AB mitosis	7	168	1.1848	1.1794	1.211	1.1479	0.1756
2c AB cytokinesis	5	180	1.0442	1.026	1.0567	0.99534	0.1838
4c ABx interphase	5	190	1.1546	1.155	1.1801	1.13	0.1675
4c ABx mitosis	5	185	1.2407	1.2506	1.2764	1.2248	0.1768
2c P1 interphase	7	161	1.1795	1.178	1.2086	1.1475	0.1849
2c P1 mitosis	7	161	1.2176	1.2204	1.2519	1.1889	0.1929

Table S1. Quantitative information describing the boxplots displayed in Fig. 2A-B, mean and std, values for median, high and low notch that are displayed on the boxplot.

Table S2: Statistical information supporting Fig. 2A,B, *Costache, Prigent-Garcia, et al.*

	paired	Two-sample ttest speed on tracks	Paired-sample ttest speed on mean	Two-sample ttest speed on mean
1-cell interphase/ 1-cell mitosis	y	0.1503	0.3676	0.5396
1c interphase/ 1c cytokinesis		9.92E-22		0.0016
1c mitosis/ 1c cytokinesis		1.78E-27		0.0013
2c AB interphase/ 2c AB mitosis	y	0.0021	0.0082	0.3185
2c AB interphase/ 2c AB cytokinesis		1.12E-24		0.0091
2c AB nitosis/ 2c AB cytokinesis		2.19E-12		0.0429
4c ABp interphase/ 4c ABp mitosis	y	1.91E-06	0.0328	0.0321
1c interphase/ 2c AB interphase		0.609		0.8609
2c AB interphase/ 4c ABp interphase		6.99E-07		0.0962
1c mitosis/ 2c AB mitosis		3.88E-07		0.1
2c AB mitosis/ 4c ABp mitosis		0.0031		0.3138
1c cytokinesis/ 2c AB cytokinesis		0.8027		0.9341
2c P1 interphase/ 2c P1 mitosis	y	0.071	0.4844	0.5465
2c AB interphase/ 2c P1 interphase	y	0.0011	0.1845	0.2725
2c AB mitosis/ 2c P1 mitosis	y	0.1066	0.1871	0.6054

Table S2. p-values for all statistical test performed on the data, y = yes. Paired sample t-test only performed when embryos have been captured and used for 2 stages, e.g. the samples are not independent.

Table S3: List of strains used in *Costache, Pirgent-Garcia, et al.*

Strain name	Genotype	Source
N2	Wild-type Bristol strain	CGC
EM302	*mgSi5[cb-UNC-119 (+) GFP::ANI-1(AH+PH)]II; nmy-2(cp52[nmy-2::mKate2 + unc-119(+)]) I; unc-119(ed3) III*	Michaux et al, 2018
FBR104	*cyk-1(jme06[cyk-1::mNeon])III*	This study
FBR106	*cyk-1(jme06[cyk-1::mNeon])III; gesIs001[Pmex-5::Lifeact::mKate::nmy-2UTR, unc-119+]*	This study
FBR160	*cyk-1(jme14[cyk-1::eGFP])III*	This study
FBR175	*cyk-1(jme14[cyk-1::eGFP])III; nmy-2(cp52[nmy-2::mKate2 + unc-119(+)]) I; unc-119(ed3) III*	This study
JH1541	*unc-119(ed4); pJH7.03 [unc-119; pie-1:GFP:actin::pie-1 3′ UTR]*	Courtesy of G. Seydoux
LP229	*nmy-2(cp52[nmy-2::mKate2 + LoxP unc-119(+) LoxP]) I; unc-119 (ed3) III*	Dickinson et al, 2017
SWG001	*gesIs001[Pmex-5::Lifeact::mKate::nmy-2UTR, unc-119+]*	Reyman et al, 2016
SWG282	*gesIs008[Pcyk-1::CYK-1::GFP::cyk-1UTR, unc-119+]*	This study

Table S4. List of parameters employed in the model. For some of the parameters, references are provided if the parameters were determined based on specific previous studies.

Symbol	Definition	Value
$r_{0,A}$	Length of an actin segment	1.4×10^{-7} [m]
$r_{c,A}$	Diameter of an actin segment	7.0×10^{-9} [m] (Kishino and Yanagida, 1988)
$\theta_{0,A}$	Bending angle formed by adjacent actin segments	0 [rad]
$\kappa_{s,A}$	Extensional stiffness of F-actin	1.69×10^{-2} [N/m]
$\kappa_{b,A}$	Bending stiffness of F-actin	2.64×10^{-19} [N·m] (Isambert et al, 1995)
$r_{0,ACP}$	Length of an ACP arm	2.35×10^{-8} [m] (Meyer and Aebi, 1990)
$r_{c,ACP}$	Diameter of an ACP arm	1.0×10^{-8} [m]
$\theta_{0,ACP}$	Bending angle formed by two ACP arms	0 [rad]
$\kappa_{s,ACP}$	Extensional stiffness of ACP	2.0×10^{-3} [N/m]
$\kappa_{b,ACP}$	Bending stiffness of ACP	1.04×10^{-19} [N·m]
$r_{0,M1}$	Length of a motor backbone segment	4.2×10^{-8} [m]
$r_{0,M2}$	Length of a motor arm	1.35×10^{-8} [m]
$r_{c,M}$	Diameter of a motor arm	1.0×10^{-8} [m]
$\theta_{0,M}$	Bending angle formed by motor backbone segments	0 [rad]
$\kappa_{s,M1}$	Extensional stiffness of a motor backbone	1.69×10^{-2} [N/m]
$\kappa_{s,M2}$	Extensional stiffness 1 of a motor arm	1.0×10^{-3} [N/m]
$\kappa_{s,M3}$	Extensional stiffness 2 of a motor arm	1.0×10^{-3} [N/m]
$\kappa_{b,M}$	Bending stiffness of a motor backbone	5.07×10^{-18} [N·m]
N_h	Number of heads represented by a motor arm	4
N_a	Number of arms per motor	8
$k_{n,A}$	Nucleation rate of actin	0.001 [$\mu M^{-1}s^{-1}$]
$k_{p,A}$	Polymerization rate of actin at the barbed end	5 [$\mu M^{-1}s^{-1}$]
$k_{d,A}$	Depolymerization rate of actin at the pointed end	50 [s^{-1}]
$k^0_{u,ACP}$	Zero-force unbinding rate constant of ACP	0.115 [s^{-1}] (Ferrer et al, 2008)
$x_{u,ACP}$	Sensitivity of ACP unbinding to applied force	1.04×10^{-10} [m] (Ferrer et al, 2008)
κ_r	Strength of repulsive force	1.69×10^{-3} [N/m]
Δt	Time step	1.15×10^{-5} [s]
μ	Viscosity of surrounding medium	8.6×10^{-1} [kg/m·s]
k_BT	Thermal energy	4.142×10^{-21} [J]
C_A	Actin concentration	200 [μM]
R_M	Ratio of myosin concentration to C_A	0.08
R_{ACP}	Ratio of ACP concentration to C_A	0.01
$<L_f>$	Average length of F-actins	~1 [μm]
ρ_f	Enhancement factor for faster actin polymerization	10
τ_f	Duration of faster actin polymerization	10 s
d_M	Time delay of myosin activation	5 s
τ_M	Duration of myosin activation	15 s

Table S5. Sequence information regarding endogenous cyk-1::GFP CRISPR knock-in. Related to STAR Methods.

Table S5. Sequence information regarding endogenous cyk-1::GFP CRISPR knock-in.

cyk-1(wild-type), with 500 bp flanks, Stop codon is highlighted in RED and bolded

GAAGACTTGGAGGAGGACTTGATCGGCAAAGATCACGACATCAGAATGCTTTGGGTCAGCTT
CAAGATCTCACTGGCTGCGCATCGGAACCGGTTCTTTCCGGACAGTTTGCTCGATCACGCAA
CGTTCCTCAAAATGATCTGCAACGACAAAATATGGAACTTCCATCATCAGTAAAACCAACAA
CGGCGCTTGATAGGGCTAAAGCATTTGGAGTTGGATTGCCGATTGGTCAGAATGAGCTCAAA
GTTCGAGTGAGAAGGAAAGGGCAACCAGCTGTTCCAgttacggtaacatattttatatgtgg
aaacttttcgaaatttaactttcagAATATCAATGGAACATCGCAAATCTCACCAACGCACA
AAGAAAACGATCCGACGGGTTCCTCGTCAACTTCATCTGGTCCTGCATCATCAAACACGGCT
ACATCATCATCATCAGGCACAGTGGTGCCATCAACAGACGATCTTCTCGCACGTCTTAATGA
TTTCTGAaagctcacatcggttgtcttatctatagatctagtcattctccgtctctatttttt
tctgtattattgccacatttttcatactttaattgtcattcacagggtccctcttctcgttcc
catttcaattgctcgttgtattttcatcagttcacttttcctttctatttttctttaggtaaa
tattttgagtttaaaaacgattttatttttattgacatggaacacaggcatactttacccga
gacattcaaaagtgaaatagaagaaatgcattagatgagctgaattcgtagtgtaagtgcac
gagacaatgcttcgtcggataccagtatttcttcgccatcgctaacaagatctttcatcgaa
gtatgcagattttctttgctttcttgttcaaattgtggcatgaaactgctaatacagtaaag
ttttcgagttgaggtcgctagtgtcggatgtttgagatggctgaaatttgaaatttgttttc
taaaacaaacg

SG sequence with **PAM**

Silent mutation incorporated region

cyk-1 Repair template(GFP knock-in at c-terminal before stop codon), with 500 bp flanks, Stop codon is highlighted in RED and bolded

GAAGACTTGGAGGAGGACTTGATCGGCAAAGATCACGACATCAGAATGCTTTGGGTCAGCTT
CAAGATCTCACTGGCTGCGCATCGGAACCGGTTCTTTCCGGACAGTTTGCTCGATCACGCAA
CGTTCCTCAAAATGATCTGCAACGACAAAATATGGAACTTCCATCATCAGTAAAACCAACAA
CGGCGCTTGATAGGGCTAAAGCATTTGGAGTTGGATTGCCGATTGGTCAGAATGAGCTCAAA
GTTCGAGTGAGAAGGAAAGGGCAACCAGCTGTTCCAgttacggtaacatattttatatgtgg
aaacttttcgaaatttaactttcagAATATCAATGGAACATCGCAAATCTCACCAACGCACA
AAGAAAACGATCCGACGGGTTCCTCGTCAACTTCATCTGGTCCTGCATCATCAAACACGGCT
ACATCATCATCATCAGGCACAGTCGTACCTTCTACTGATGATTTATTGGCTAGACTTAACGA
CTTTACCAGTGGTAGCGGCTCCAAGGGAGAGGAGCTCTTCACCGGAGTCGTCCCAATCCTCG
TCGAGCTCGACGGAGACGTCAACGGACACAAGTTCTCCGTCTCAGGAGAGGGAGAGGGAGAC
GCCACCTACGGAAAGCTCACCCTCAAGTTCATCTGCACCACCGGAAAGCTCCCAGTCCCATG
GCCAACCCTCGTCACCACCTTCACTTACGGAGTCCAATGCTTCTCCCGTTACCCAGACCACA
TGAAGCGTCACGACTTCTTCAAGTCCGCCATGCCAGAGGGATACGTCCAAGAGCGTACCATC
TTCTTCAAGgtaagtttaaacattaattaatactaactaaccctgattatttaaattttcag

GACGACGGAAACTACAAGACCCGTGCCGAGGTCAAGTTCGAGGGAGACACCCTCGTCAACCG
TATCGAGCTCAAGgtaagtttaaacagttcggtactaactaaccatacatatttaaatttttc
agGGAATCGACTTCAAGGAGGACGGAAACATCCTCGGACACAAGCTCGAATACAACTACAAC
TCCCACAACGTCTACATCATGGCCGACAAGCAAAAGAACGGAATCAAGGTCAACTTCAAGgt
aagtttaaacatgattttactaactaactaatctgatttaaattttcagATCCGTCACAACA
TCGAGGACGGATCTGTCCAACTCGCCGACCACTACCAACAAAACACCCCAATCGGAGACGGA
CCAGTCCTCCTCCCAGACAACCACTACCTCTCCACCCAATCCGCCCTCTCCAAGGACCCAAA
CGAGAAGCGTGACCACATGGTCCTCAAGGAGTTCGTCACCGCTGCCGGAATCACCCACGGAA
TGGACGAGCTCTACAAG**TGA**aagctcacatcggttgtcttatctatagatctagtcattctc
cgtctctatttttctgtattattgccacattttcatactttaattgtcattcacagggtc
cctcttctcgttccatttcaattgctcgttgtattttcatcagttcacttttcctttctatt
ttctttaggtaaatattttgagtttaaaaacgattttatttttattgacatggaacacaggc
atactttacccgagacattcaaaagtgaaatagaagaaatgcattagatgagctgaattcgt
agtgtaagtgcacgagacaatgcttcgtcggataccagtatttcttcgccatcgctaacaag
atctttcatcgaagtatgcagattttctttgctttcttgttcaaattgtggcatgaaactgc
taatacagtaaagttttcgagttgaggtcgctagtgtcggatgtttgagatggctgaaattt
gaaatttgttttctaaaacaaacg

SG sequence

Silent mutation incorporated region in the repair template

Linker sequence prior to GFP

The GFP sequence is shown in Green

Silent mutations are highlighted in Red with respect of wild-type sequence, and incorporated in the repair template:

```
Wild-type PAM downstream.ape from 1 to 44
Alignment to
Repair template PAM downstream.ape--  Matches:28; Mismatche

                  *          *          *          *
      1>TGGTGCCATCAACAGACGATCTTCTCGCACGTCTTAATGATTTC>44
      1>TCGTACCTTCTACTGATGATTTATTGGCTAGACTTAACGACTTT>44
```

METHODS S1: Description of the mathematical model of formin recruitment kinetics, related to Figure 4

1 A model to explore barbed ends dynamics *in vivo*

1.1 Assumptions

The proposed model is based on the following set of assumptions:

1. RhoA activation activity is represented as a smooth periodic function ($sin^6(\omega t)$,
2. inactive formins are activated by RhoA and recruited to the cortex, becoming "recruited",
3. we considered CYK-1 formins are poor nucleators but good elongators in our system, and therefore hypothesized that formins do not nucleate new filaments (*in vitro* actin assembly yields ∼1 new nucleated filament per 550 CYK-1 formin molecule at 2.5 μM actin and 2.5 μM profilin PFN-1, Neidt:2008df)
4. once recruited at the cortex, formins bind to barbed ends through a trimolecular reaction to drive actin assembly, becoming "elongating",
5. recruited formins unbind from the cortex to the cytoplasmic pool, (6) elongating formins unbind from the cortex to the cytoplasmic pool.

1.2 Definitions

$[CYK-1_{recruited}] : [CYK1^{*}]$
$[CYK-1_{elongating}] : [CYK1^{**}]$

$[Barbedends] : [BE]$
$Period : T$

1.3 Equations

$$\frac{d\left([CYK1^*]\right)}{dt} = k_1 \cdot \sin^6\left(\frac{\pi t}{T}\right) - k_3 \cdot [CYK1^*] - 2 \times k_4 \cdot [CYK1^*]^2 \cdot [BE] \quad (1)$$

$$\frac{d\left([CYK1^{**}]\right)}{dt} = k_4 \cdot [CYK1^*]^2 \cdot [BE] - k_2 \cdot [CYK1^{**}] \quad (2)$$

$$\frac{d\left([BE]\right)}{dt} = -k_4 \cdot [CYK1^*]^2 \cdot [BE] + k_5 - k_6 \cdot [BE] \quad (3)$$

1.4 Origin of the terms

$$\frac{d\left([CYK1^*]\right)}{dt} = k_1 \cdot \sin^6\left(\frac{\pi t}{T}\right) - k_3 \cdot [CYK1^*] - 2 \times k_4 \cdot [CYK1^*]^2 \cdot [BE] \quad (4)$$

The **first term** describes the pulse activation by Rho, which is transient and has a period of ∼30s. An empirical comparison of this waveform with actual RhoA dynamics is provided in Fig. S9.The **second term** describes inactivation of the recruited species. The **third term** describes the conversion from recruited to elongating species, as a trimolecular reaction, corresponding to the assumption that cytoplasmic, inactive formins are monomeric and assemble as dimers upon binding with barbed-ends. Recruited formins are not recycled back from the elongating formin pool, as we considered they had left the location of the pulse and were no longer available.

$$\frac{d\left([CYK1^{**}]\right)}{dt} = k_4 \cdot [CYK1^*]^2 \cdot [BE] - k_2 \cdot [CYK1^{**}] \quad (5)$$

The **first term** equates the conversion from inactive to active species (third term above), while the **second term** describes inactivation of the active species which is not converted back to recruited but is instead inactivated in the cytoplasmic species.

$$\frac{d\left([BE]\right)}{dt} = -k_4 \cdot [CYK1^*]^2 \cdot [BE] + k_5 - k_6 \cdot [BE] \quad (6)$$

The **first term** corresponds to the conversion of *free* barbed ends. These *free* barbed ends are likely to correspond to capped barbed ends: formins will displace the equilibrium and replace capping proteins, due to their higher affinity for barbed ends compared to capping proteins (*Neidt et al, 2008*). The **second**

term corresponds to a low, continuous source/production of barbed ends. This slow production of barbed ends could result from a combination of factors, such as leaky free G-actin nucleation, or cofilin- or myosin II-mediated filament severing. The **third term** corresponds to an inactivation of free barbed ends, representing the disappearance of barbed ends after some time. A typical value for that term will be on the order of magnitude of actin turnover rate ($\sim 0.1 - 1\ s^{-1}$). Barbed ends are not recycled back from the elongating formin pool, as we considered they had left the location of the pulse and were no longer available.

1.5 Numerical values of the kinetic parameters

Parameters used:

K(1)	Production rate	30 (#/s)
K(2)	Elongating formins inactivation rate	0.2000 (1/s)
K(3)	Recruited formins inactivation rate	0.8000 (1/s)
K(4)	Association rate of recruited formins with barbed ends	100 (1/s/#)
K(5)	Free barbed-ends production rate	0.4500 (#/s)
K(6)	Free barbed-ends destruction rate	0.0060 (1/s)

has dimension of concentration or number of molecules

2 Formins and barbed ends *in vivo*: implication of *in vitro* measurements

2.1 Rationale for quantitative approach based on *in vitro* kinetics measurements

In the previous section, Fig. 4 and Fig. S2, we proposed a model to test whether a free barbed end saturation mechanism that we were proposing could prove compatible with the observed sequence of events. To this end, we based our approach on observed cortical dynamics from single-molecule data, and bypassed both measurements for specific steps of the reaction, and detailed specifics of the diffusion mechanisms (2D surface reaction kinetics, with a first recruitment from a cytoplasmic pool, then a second recruitment directly from a pre-recruited cortical pool). In particular, local concentrations and known reactions constants considered exclusively within the cell cortex volume were not explicitly discussed.

Below, using side-by-side in vitro kinetics measurements from the literature, in vivo measurements, and estimations for concentrations, we show that formin recruitment may shift the system between a state in which barbed ends are limiting, at the peak of the pulse, and a state in which barbed ends locally outnumber formins.

2.2 Definitions

$[BarbedEnds] : [B]$
$[Formin] : [F]$
$[BarbedEnds–ForminsComplex] : [BF]$
Barbed ends association rate with formin : k_+^B, or simply k_+

2.3 Initial conditions and conservation

Initial conditions:
$[InitialBarbedEnds] : [B]_0$
$[InitialFormin] : [F]_0$

Conservation:
$[B] + [BF] = [B]_0$
$[F] + [BF] = [F]_0$

2.4 Basic chemical scheme

$\mathrm{B} + \mathrm{E} \underset{\mathrm{k_-}}{\overset{\mathrm{k_+}}{\rightleftarrows}} \mathrm{BE}$

Given off-rates measured in vitro –and to get an explicit formulation of the solution– we simplify the considered equation to a simple one-way reaction. While this is compatible with rate measured *in vitro*, the full model presented in the paper takes more empirical approach based on single-molecule measurements.

$\mathrm{B} + \mathrm{E} \xrightarrow{\mathrm{k_+}} \mathrm{BE}$

2.5 Equations

$$\frac{d\left([BF]\right)}{dt} = k_+ \cdot [B] \cdot [F] \tag{7}$$

$$\frac{d\left([BF]\right)}{dt} = k_+ \cdot \left([F]_0 - [BF]\right) \cdot \left([B]_0 - [BF]\right) \tag{8}$$

$$\frac{d\left([BF]\right)}{\left([B]_0 - [BF]\right)} \cdot \frac{1}{[F]_0 - [B]_0} + \frac{d\left([BF]\right)}{\left([F]_0 - [BF]\right)} \cdot \frac{1}{[B]_0 - [F]_0} = k_+ \cdot dt \tag{9}$$

$$\ln\left(\frac{\left([B]_0 - [BF]\right)}{\left([F]_0 - [BF]\right)} \cdot \frac{[F]_0}{[B]_0}\right) = k_+ \cdot \left([B]_0 - [F]_0\right) \cdot t \tag{10}$$

$$\boxed{[BF] = \frac{1 - e^{k_+ \cdot \left([B]_0 - [F]_0\right) \cdot t}}{\frac{1}{[B]_0} - \frac{e^{k_+ \cdot \left([B]_0 - [F]_0\right) \cdot t}}{[F]_0}}} \tag{11}$$

2.6 Formin/barbed-ends kinetics expected from *in vitro* data

We used previously measured values for k_+^B, (Shekhar, Nat Comm, 2015, Fig S4):

$$k_+^B = (29.1 \pm 0.6)\,\mu\mathrm{M}^{-1}\,\mathrm{s}^{-1} \tag{12}$$

We also defined the "excess factor" alpha as:

$$[F]_0 = \alpha \cdot [B]_0 \tag{13}$$

For barbed ends, this gives:

$$B = B_0 \cdot \frac{1 - \frac{1}{\alpha}}{e^{-k_+^B \cdot (B_0 - F_0) \cdot t} - \frac{1}{\alpha}} \tag{14}$$

Generally, as long as formins are in excess, the half life of barbed ends is bounded such that:

$$\frac{\ln(2)}{k_+^B \cdot F_0} \leq \tau_{1/2} \leq \frac{1}{k_+^B \cdot F_0} \tag{15}$$

We estimated formin concentrations from the total number of cortical molecules ($\sim 10^4$), divided by the *C. elegans* embryo volume ($\sim 40 \times 10^3\,\mu m^3$), yielding an overall formin concentration of $\sim 1\,nM$. Taking into account peak concentration during pulsed contractions, which can concentrate formins more than 10-fold factor, formin concentrations could reach $\sim 10\,nM$.

It is delicate to predict the effect of the binding of RhoA and restriction of CYK-1 to the cell surface on the on-rate of CYK-1. RhoA binding has two direct effects that we can consider consecutively. The first effect is to couple the reaction to the cell surface. The second effect is to drive transient local changes in CYK-1 concentration.

The effects of coupling reactions to the cell surface are complex –factors impacting the reaction kinetics include in particular diffusion kinetics and reduction of dimensionality– and have long been discussed (Adam and Delbrück, Structural Chemistry and Molecular Biology, 1968, Burg and Purcell, Biophys J, 1977, Axelrod and Wang, Biophys J, 1994, Kholodenko et al. Trends in Cell Biol., 2000), with the underlying disputed idea that cell surface coupling may accelerate biological reactions. How the binding to RhoA would affect the on-rate of CYK-1 to scarce barbed ends remains an open question, one way or another. Specifically, following Kholodenko (Kholodenko et al. Trends in Cell Biol., 2000), the rate enhancement h of the reaction from 3D to 2D can be approximated by:

$$h = (0.02 - 0.05) \cdot \left(\frac{D_m}{D_c}\right) \cdot \left(\frac{r_{cell}}{r_{prot}}\right) \tag{16}$$

with D_m the membrane diffusion, D_c the cytoplasmic diffusion, r_{cell} the cell radius and r_{prot} the protein radius. We thus estimate that $D_m/D_c \sim 10^{-2}$; in our biological system, we estimate $r_{cell} \sim 15\,\mu m$ and $r_{prot} \sim 5\,nm$, we find h $\approx$ 0.6–1.5. This result supports the idea that there is no intrinsic significant modulation of the reaction kinetics (specifically of the binding rate) directly associated to RhoA-driven CYK-1 confinement to the cell surface. The second effect is to drive local transient accumulations of CYK-1: RhoA pulses concentrate CYK-1 unevenly locally, raising CYK-1 concentration from 1 nM to 10 nM. This second effect – in the absemce of a negative impact of the confinement of the reaction in 2D – justifies our assumption of an increased concentration of CYK-1. In summary, the binding of RhoA should not affect drastically the kinetics of the reaction, as the effects of decreased diffusion and dimensionality reduction are approximately balanced. But the RhoA mediated concentration of CYK-1 in the pulses drives a local increase in concentration that we had to consider when analyzing CYK-1 kinetics, leading us to propose a local concentration of formins of $\sim 10\,nM$.

If we estimate that 10 % of the actin is polymerized (Robin *et al*, 2014), such that for simplicity F-actin monomers $\sim$4 µM, with an average filament length of $\sim$6 µm, the overall barbed-ends concentration should range around $\sim 2 - 3$nM.

Assuming initial local concentration of barbed ends of $\sim$3 nM, accumulations of formins at the cell surface bypassing $\sim$10 nM would enter a range compatible with the measured delays $\sim$2.7 s. This result suggests that the characteristic time for saturation of free, uncapped barbed ends resides at the boundary of the temporal dynamics observed in our experiments.

Both approaches bring interesting information: the strategy in Fig. 4 confirms that such a mechanism could in theory drive the observed kinetics, while the quantitative approach derived here suggests that this system could work at the limit of barbed end saturation, and formin recruitment would shift the system between a state in which barbed ends are limiting, at the peak of the pulse, and a state in which barbed ends locally outnumber formins.

2.7 Capping/barbed-ends kinetics expected from *in vitro* data

We also considered the affinity of CP for barbed ends, and a potential competition with formins. Cellular concentrations of CP are high ($\sim$ 1 µM, Pollard and Borisy, Cell, 2003, data not available in *C. elegans*), but CP concentration is buffered and its activity regulated (by CPI proteins, e.g. CARMIL, Fujiwara et al, PNAS, 2014), such that the concentration of free CP available for barbed end capping may be as low as 5-50 nM (Shekhar et al., J Cell Sci, 2016), values that would be within one order of magnitude of formin peak concentration in the pulse (10 nM). In these conditions, and with known ranges for the on-rate of capping proteins ($\sim 4.6 \pm 1.1$ µM^{-1} s^{-1} (Schafer et al., J Cell Biol, 1996), $\sim$ 3.9 µM^{-1} s^{-1} (Miyoshi et al., J Cell Biol, 2006), $\sim 12.8 \pm 1.1$ µM^{-1} s^{-1} (Shekhar et al., Nat Comm, 2015)), suggests that a competition between formins and capping could indeed take place.

METHODS S2: Detailed description of the computational model of actomyosin mechanics, related to Figure 6.

Brownian dynamics via the Langevin equation

In our agent-based model, F-actin is simplified into serially connected cylindrical segments with barbed and pointed ends. Motors have a backbone structure with eight arms ($N_a = 8$) attached, and each of the motor arm represents four myosin heads. Therefore, the total number of myosin heads represented by one motor is 32, which is not quite different from 56 myosin heads in one non-muscle myosin thick filament (Tyska et al, 1999). The backbone and arms of the motors are also described by cylindrical segments. ACPs are comprised of two cylindrical arm segments.

The displacements of all the cylindrical segments are determined by the Langevin equation with the negligence of inertia:

$$\mathbf{F}_i - \zeta_i \frac{\mathrm{d}\mathbf{r}_i}{\mathrm{d}t} + \mathbf{F}_i^{\mathrm{T}} = 0 \tag{S1}$$

where $\mathbf{r}_i$ is a position vector of the ith element, ζ_i is a drag coefficient, t is time, $\mathbf{F}_i$ is a deterministic force, and $\mathbf{F}_i^{\mathrm{T}}$ is a stochastic force satisfying the fluctuation-dissipation theorem (Underhill and Doyle, 2004):

$$\left\langle \mathbf{F}_i^{\mathrm{T}}(t)\mathbf{F}_j^{\mathrm{T}}(t) \right\rangle = \frac{2k_{\mathrm{B}}T\zeta_i\delta_{ij}}{\Delta t}\boldsymbol{\delta} \tag{S2}$$

where $\boldsymbol{\delta}$ is a second-order tensor, δ_{ij} is the Kronecker delta, and $\Delta t = 1.15\text{x}10^{-5}$ s is a time step. The drag coefficients are calculated via an approximated form for cylindrical objects (Clift, Grace and Weber, 2005):

$$\zeta_i = 3\pi\mu r_{c,i} \frac{3 + 2r_{0,i} / r_{c,i}}{5} \tag{S3}$$

where μ is the viscosity of surrounding medium, and $r_{0,i}$ and $r_{c,i}$ are the length and diameter of segments, respectively. The positions of all the cylindrical segments are updated at each time step via the Euler integration scheme:

$$\mathbf{r}_i(t + \Delta t) = \mathbf{r}_i(t) + \frac{\mathrm{d}\mathbf{r}_i}{\mathrm{d}t}\Delta t = \mathbf{r}_i(t) + \frac{1}{\zeta_i}\left(\mathbf{F}_i + \mathbf{F}_i^{\mathrm{T}}\right)\Delta t \tag{S4}$$

Deterministic forces

Deterministic forces include extensional forces maintaining equilibrium lengths, bending forces maintaining equilibrium angles, and repulsive forces accounting for volume-exclusion effects between actin segments. The extensional and bending forces originate from the following potentials:

$$U_s = \frac{1}{2}\kappa_s (r - r_0)^2 \tag{S5}$$

$$U_b = \frac{1}{2}\kappa_b \left(\theta - \theta_0\right)^2 \tag{S6}$$

where κ_s and κ_b are extensional and bending stiffnesses, r and r_0 are the instantaneous and equilibrium lengths of cylindrical segments, and θ and θ_0 are instantaneous and equilibrium angles formed by segments. The equilibrium length of actin segments ($r_{0,A}$ = 140 nm) and an equilibrium angle formed by two adjacent actin segments ($\theta_{0,A}$ = 0 rad) are maintained by extensional ($\kappa_{s,A}$) and bending ($\kappa_{b,A}$) stiffnesses of actins, respectively. The reference value of $\kappa_{b,A}$ corresponds to the persistence length of ~9 μm (Isambert et al, 1995). The equilibrium length of ACP arms ($r_{0,ACP}$

= 23.5 nm) and an equilibrium angle formed by the two arm segments of each ACP ($\theta_{0,ACP}$ = 0 rad) are regulated by extensional ($\kappa_{s,ACP}$) and bending ($\kappa_{b,ACP}$) stiffnesses of ACPs, respectively. The equilibrium length of motor backbone segments ($r_{s,M1}$= 42 nm) and an equilibrium angle formed by adjacent backbone segments ($\theta_{0,M}$ = 0 rad) are maintained by extensional ($\kappa_{s,M1}$) and bending ($\kappa_{b,M}$) stiffnesses, respectively. The value of $\kappa_{s,M1}$ is equal to that of $\kappa_{s,A}$, whereas the value of $\kappa_{b,M}$ is larger than that of $\kappa_{b,A}$. The extension of each motor arm is regulated by the two-spring model with stiffnesses of transverse ($\kappa_{s,M2}$) and longitudinal ($\kappa_{s,M3}$) springs. The transverse spring maintains an equilibrium distance ($r_{0,M2}$ = 13.5 nm) between the endpoint of a motor backbone and an actin segment where the arm of the motor binds, whereas the longitudinal spring maintains a right angle between the motor arm and the actin segment ($r_{0,M3}$ = 0 nm).

The repulsive force is represented by a harmonic potential (Kim et al, 2009):

$$U_r = \begin{cases} \frac{1}{2}\kappa_r \left(r_{12} - r_{c,A}\right)^2 & \text{if} \quad r_{12} < r_{c,A} \\ 0 & \text{if} \quad r_{12} \geq r_{c,A} \end{cases} \tag{S7}$$

where κ_r is the strength of repulsive force, and r_{12} is a minimum distance between two actin segments. Forces exerted on actin segments by bound motors and ACPs or by the repulsive force are distributed onto the barbed and pointed ends of the actin segments as described in our previous work (Young, Murrell, Kim, 2015).

Dynamics of ACPs

ACPs bind to binding sites located on actin segments every 7 nm without preference for cross-linking angles at a constant rate and also unbind from F-actin at a force-dependent rate determined by Bell's law (Bell, 1978):

$$k_{\mathrm{u,ACP}} = \begin{cases} k^0_{\mathrm{u,ACP}} \exp\left(\dfrac{x_{\mathrm{u,ACP}} \left| \vec{F}_{\mathrm{s,ACP}} \right|}{k_{\mathrm{B}}T} \right) & \text{if } r \geq r_{0,\mathrm{ACP}} \\ k^0_{\mathrm{u,ACP}} & \text{if } r < r_{0,\mathrm{ACP}} \end{cases} \quad \text{(S8)}$$

where $\left| \vec{F}_{\mathrm{s,ACP}} \right|$ is a spring force acting on an ACP arm, $k^0_{\mathrm{u,ACP}}$ is the zero-force unbinding rate constant, $x_{\mathrm{u,ACP}}$ is sensitivity to an applied force, and $k_{\mathrm{B}}T$ is thermal energy. The values of $k^0_{\mathrm{u,ACP}}$ (= 0.115 s^{-1}) and $x_{\mathrm{u,ACP}}$ (= 1.04×10^{-10} m) are determined based on filamin A (Ferrer et al, 2008).

Dynamics of motors

Motor arms bind to binding sites on actin segments at the rate of $40N_{\mathrm{h}}$ s^{-1}, where $N_{\mathrm{h}} = 8$ is the number of myosin heads represented by each motor arm. The walking ($k_{\mathrm{w,M}}$) and unbinding ($k_{\mathrm{u,M}}$) rates of the motor arms are determined by the parallel cluster model to mimic the mechanochemical cycle of non-muscle myosin II (Erdmann, Albert, Schwartz, 2013, Erdmann, Schwartz, 2012). The details of implementation and benchmarking of the parallel cluster model in our models are described in detail in our previous study (Kim, 2015). Note that $k_{\mathrm{w,M}}$ and $k_{\mathrm{u,M}}$ are smaller with larger applied loads because motors exhibit a catch-bond behavior. The unloaded walking velocity and stall force of motors are ~140 nm/s and ~5.7 pN, respectively.

Actin dynamics

The formation of F-actin is initiated from a nucleation event with the appearance of one cylindrical segment with polarity (i.e., with barbed and pointed ends) in a random orientation

perpendicular to the z direction. The polymerization and depolymerization of actins are simulated by the addition and removal of cylindrical segments, respectively, as in our previous studies (Mak et al, 2016). The average length of F-actin ($<L_f>$) used in simulations is ~1 μm. This value is comparable to that estimated in our in vivo experiments. In addition, with the reference values of the rate constants for actin dynamics, each F-actin turns over every ~10 s.

Contraction of actin

In order to quantitatively analyze the network morphology, we evaluate the contraction of F-actin, using the spatial distribution of F-actins in activated regions whose dimension is 5×5 μm in x and y directions. First, the activated region is divided into $N_G \times N_G$ grids. We found that the optimal level of N_G is 15. All grids are indicated by their own coordinate, (*i, j*). In each grid, we measure the intensity of actin segments at time *t*, $\rho_{A,t}^{i,j}$. Then, the standard deviation of $\rho_{A,t}^{i,j}$ in all N_G^2 grids is calculated and normalized by the initial mean value of actin density, $\overline{\rho}_{A,0}$. The normalized value represents the extent of actin contraction at each time point, *t*:

$$\text{Actin contraction at } t = \frac{1}{\overline{\rho}_{A,0}} \sqrt{\frac{\sum_{i,j=1}^{N_G} (\rho_{A,t}^{i,j} - \overline{\rho}_{A,t})^2}{N_G}} \qquad \text{(Eq. S9)}$$

We calculate the time evolution of actin contraction by subtracting the initial value of actin contraction from the instantaneous value at each time step. As F-actins aggregate more within the activated region (i.e., more contraction), the spatial distribution of F-actins will become more heterogeneous, increasing the standard deviation of $\rho_{A,t}^{i,j}$ and thus enhancing the extent of actin

contraction. From the time evolution curve (Fig. 6b, inset), we obtain the maximal extent of actin contraction and contraction level at a plateau phase.

Contraction of myosin motors

We calculate the extent of motor contraction using the center position of motor thick filaments, $(x^i_{\mathrm{M},t},\ y^i_{\mathrm{M},t})$, where i is the index of motors, and t is time. At each time step, we calculate a distance between the center position of each thick filament and the center position of a currently activated region, $(x_{\mathrm{reg},t},\ y_{\mathrm{reg},t})$. We assume that the average of all the distances represents the approximate size of motor clusters. The average is further divided by an initial value:

$$\text{Motor contraction} = \frac{\sum_{i=1}^{N_\mathrm{M}} \sqrt{(x^i_{\mathrm{M},t} - x_{\mathrm{reg},t})^2 + (y^i_{\mathrm{M},t} - y_{\mathrm{reg},t})^2} \,/\, N_\mathrm{M}}{\sum_{i=1}^{N_\mathrm{M}} \sqrt{(x^i_{\mathrm{M},0} - x_{\mathrm{reg},0})^2 + (y^i_{\mathrm{M},0} - y_{\mathrm{reg},0})^2} \,/\, N_\mathrm{M}} \qquad \text{(Eq. S10)}$$

In the time evolution of motor contraction, we average the maximum values of the motor contraction in all pulse periods to use it as an indicator for the extent of motor contraction.

Table S4. List of parameters employed in the model. For some of the parameters, references are provided if the parameters were determined based on specific previous studies.

Symbol	Definition	Value
$r_{0,A}$	Length of an actin segment	1.4×10^{-7} [m]
$r_{c,A}$	Diameter of an actin segment	7.0×10^{-9} [m] (Kishino and Yanagida, 1988)
$\theta_{0,A}$	Bending angle formed by adjacent actin segments	0 [rad]
$\kappa_{s,A}$	Extensional stiffness of F-actin	1.69×10^{-2} [N/m]
$\kappa_{b,A}$	Bending stiffness of F-actin	2.64×10^{-19} [N·m] (Isambert et al, 1995)
$r_{0,ACP}$	Length of an ACP arm	2.35×10^{-8} [m] (Meyer and Aebi, 1990)
$r_{c,ACP}$	Diameter of an ACP arm	1.0×10^{-8} [m]
$\theta_{0,ACP}$	Bending angle formed by two ACP arms	0 [rad]
$\kappa_{s,ACP}$	Extensional stiffness of ACP	2.0×10^{-3} [N/m]
$\kappa_{b,ACP}$	Bending stiffness of ACP	1.04×10^{-19} [N·m]
$r_{0,M1}$	Length of a motor backbone segment	4.2×10^{-8} [m]
$r_{0,M2}$	Length of a motor arm	1.35×10^{-8} [m]
$r_{c,M}$	Diameter of a motor arm	1.0×10^{-8} [m]
$\theta_{0,M}$	Bending angle formed by motor backbone segments	0 [rad]
$\kappa_{s,M1}$	Extensional stiffness of a motor backbone	1.69×10^{-2} [N/m]
$\kappa_{s,M2}$	Extensional stiffness 1 of a motor arm	1.0×10^{-3} [N/m]
$\kappa_{s,M3}$	Extensional stiffness 2 of a motor arm	1.0×10^{-3} [N/m]
$\kappa_{b,M}$	Bending stiffness of a motor backbone	5.07×10^{-18} [N·m]
N_h	Number of heads represented by a motor arm	4
N_a	Number of arms per motor	8
$k_{n,A}$	Nucleation rate of actin	0.001 [$\mu M^{-1}s^{-1}$]
$k_{p,A}$	Polymerization rate of actin at the barbed end	5 [$\mu M^{-1}s^{-1}$]
$k_{d,A}$	Depolymerization rate of actin at the pointed end	50 [s^{-1}]
$k^0_{u,ACP}$	Zero-force unbinding rate constant of ACP	0.115 [s^{-1}] (Ferrer et al, 2008)
$x_{u,ACP}$	Sensitivity of ACP unbinding to applied force	1.04×10^{-10} [m] (Ferrer et al, 2008)
κ_r	Strength of repulsive force	1.69×10^{-3} [N/m]
Δt	Time step	1.15×10^{-5} [s]
μ	Viscosity of surrounding medium	8.6×10^{-1} [kg/m·s]
k_BT	Thermal energy	4.142×10^{-21} [J]
C_A	Actin concentration	200 [μM]
R_M	Ratio of myosin concentration to C_A	0.08
R_{ACP}	Ratio of ACP concentration to C_A	0.01
$<L_f>$	Average length of F-actins	~1 [μm]
ρ_f	Enhancement factor for faster actin polymerization	10
τ_f	Duration of faster actin polymerization	10 s
d_M	Time delay of myosin activation	5 s
τ_M	Duration of myosin activation	15 s